

## General Disclaimer

### One or more of the Following Statements may affect this Document

- This document has been reproduced from the best copy furnished by the organizational source. It is being released in the interest of making available as much information as possible.
- This document may contain data, which exceeds the sheet parameters. It was furnished in this condition by the organizational source and is the best copy available.
- This document may contain tone-on-tone or color graphs, charts and/or pictures, which have been reproduced in black and white.
- This document is paginated as submitted by the original source.
- Portions of this document are not fully legible due to the historical nature of some of the material. However, it is the best reproduction available from the original submission.



## Technical Memorandum 83852

# A HIGH RESOLUTION SPECTROSCOPIC STUDY OF THE $\nu_2$ BAND OF HYDROGEN SULFIDE AND THE 1-0 BAND OF HYDROGEN IODIDE

(NASA-TM-83852) A HIGH RESOLUTION  
SPECTROSCOPIC STUDY OF THE  $\nu$  SUB 2 BAND OF  
HYDROGEN SULFIDE AND THE 1-0 BAND OF  
HYDROGEN IODIDE Ph.D. Thesis - Maryland  
Univ. (NASA) 159 p HC A08/MF A01 CSCL 07D G3/25

N82-19336

Unclas  
16362

Lawrence Larrabee Strow



DECEMBER 1981

National Aeronautics and  
Space Administration

**Goddard Space Flight Center**  
Greenbelt, Maryland 20771

**A HIGH RESOLUTION SPECTROSCOPIC STUDY OF  
THE  $\nu_2$  BAND OF HYDROGEN SULFIDE  
AND THE 1-0 BAND OF HYDROGEN IODIDE**

by

**Lawrence Larrabee Strow**

**Dissertation submitted to the Faculty of the Graduate School  
of the University of Maryland in partial fulfillment  
of the requirements for the degree of  
Doctor of Philosophy**

**1981**

## ABSTRACT

Title of Dissertation:     **A High Resolution Spectroscopic Study of the  $\nu_2$  Band of Hydrogen Sulfide and the 1-0 Band of Hydrogen Iodide**

Lawrence Larrabee Strow, Doctor of Philosophy, 1981

Dissertation directed by:   **Dr. Thomas D. Wilkerson**  
                                  **Research Professor**  
                                  **Institute for Physical Science and Technology**

A tunable diode laser spectrometer has been constructed and used to study: (1) the effects of centrifugal distortion on the transition frequencies and strengths of the  $\nu_2$  band of  $\text{H}_2\text{S}$ , and (2) nuclear quadrupole hyperfine structure in the 1-0 band of HI. Some additional transition frequencies in the  $\nu_2$  band of  $\text{H}_2\text{S}$  were measured with a high resolution grating spectrometer.

A total of 126 line frequencies and 94 line strengths in the  $\nu_2$  band were measured. The average accuracy of the line frequency measurements was  $\pm 0.00016 \text{ cm}^{-1}$ . An error analysis of relative frequency measurements using a diode laser is given. The line strengths were measured to an average accuracy of about 3%. The effect of the finite spectral width of the diode laser on the measurement of line strengths is discussed in detail.

The observed  $\text{H}_2\text{S}$  line frequencies were fit to Watson's AS and NS reduced Hamiltonians in both the  $\text{I}^r$  and  $\text{III}^r$  coordinate representations in order to determine the best set of rotation-distortion constants for the upper state of the  $\nu_2$  band. Successful fits were obtained for all the reduced Hamiltonians except the AS Hamiltonian in the  $\text{III}^r$  representation. The characteristics of this Hamiltonian are examined in detail to understand its poor behavior relative to the other reduced Hamiltonians. Comparisons of the observed line strengths in this band to calculated rigid rotor line strengths are also presented.

Nuclear quadrupole hyperfine structure in the 1-0 vibration-rotation band of HI, was observed with the diode laser spectrometer. The R(0), P(1), P(2), and P(3) lines of



this band were recorded, all of which clearly exhibit nuclear quadrupole splittings. The upper vibrational state nuclear quadrupole coupling constant, determined from the observed splittings, was found to be  $-1850\text{MHz} \pm 12\text{MHz}$ , or  $1.2\% \pm 0.7\%$  larger than the ground state coupling constant. It is believed that this is the first observation of nuclear quadrupole structure in the vibration-rotation spectrum of a diatomic molecule.

The results of the  $\text{H}_2\text{S}$  measurements described here should serve as a severe test of present and future theories of centrifugal distortion in asymmetric rotor spectra. This work also demonstrates the utility of diode lasers for highly accurate studies of infrared molecular spectra.

## ACKNOWLEDGEMENTS

I wish to express my appreciation to Dr. Thomas D. Wilkerson, who directed this work and provided the support and encouragement needed for its successful completion. I am indebted to Dr. W. J. Lafferty for his suggestion of both research topics in this work. I would also like to thank Dr. Lafferty for making the molecular spectroscopy laboratory at the National Bureau of Standards available to me for part of this work and for his hospitality during my stay there. I am grateful to Dr. C. L. Korb for my introduction to experimental molecular spectroscopy and for his support throughout my graduate school career. I would like to thank Drs. J. Susskind and D. E. Jennings for many helpful discussions and for their improvements to parts of this manuscript.

The direction supplied by my advisement committee played an important role in this work and is gratefully acknowledged. I was fortunate to have a committee with such a diversity of expertise in the field of molecular spectroscopy. The occasional meetings I had with the committee to discuss the progress and problems in this research were invaluable.

Thanks are due to Bruce Gentry for his part in the construction of the gas cell and for many discussions concerning the experimental portions of this work. I wish to thank Dr. J. Hillman for providing the rotational analysis computer program and for discussions concerning its operation. I am grateful to Lisa Steffens and Bob Orr for the many hours they spent operating the raw data analysis programs.

I also wish to express my appreciation to Harvey Ostrow and Dr. H. Plotkin for supporting my graduate school education over its many years.

I cannot find words to express my thanks to my wife, Van Lynn Wensil, for her love, patience, and understanding. Her many interests and endeavors in life have given me needed perspective during this time of such concentrated study.

## TABLE OF CONTENTS

	<u>Page</u>
ACKNOWLEDGEMENTS .....	ii
LIST OF TABLES .....	v
LIST OF FIGURES .....	vii
<b>CHAPTER</b>	
I.    INTRODUCTION .....	1
II.   THEORY OF ASYMMETRIC ROTOR VIBRATION- ROTATION SPECTRA .....	5
A.  Development of the Rotational Hamiltonian .....	5
B.  Watson's Reduced Rotational Hamiltonian .....	10
C.  Calculation of the Rotational Energy Levels .....	18
D.  Vibration-Rotation Line Strengths of an Asymmetric Top Molecule .....	22
III.  DIODE LASER SPECTROMETER AND DATA ACQUISITION .....	28
A.  Introduction .....	28
B.  Experimental Apparatus .....	29
C.  Operation of the Diode Laser Spectrometer and Sample Spectra .....	35
D.  Grating Spectrometer Measurements .....	56
IV.  EXPERIMENTAL RESULTS-DETERMINATION OF THE H <sub>2</sub> S LINE FREQUENCIES AND STRENGTHS .....	58
A.  Introduction .....	58
B.  Frequency Measurements and Error Analysis .....	59
C.  Strength Measurements and Error Analysis .....	63
V.   ROTATIONAL ANALYSIS OF THE $\nu_2$ BAND OF H <sub>2</sub> S .....	85

	<u>Page</u>
A. Rotational Structure of the $\nu_2$ Band and Line Assignments . . . . .	85
B. Least-Squares Fitting of the Rotational Hamiltonian . . . . .	90
C. Results of Least-Squares Fits for the Rotational Constants of the $\nu_2$ Band . . . . .	94
D. Characteristics of the AS-III <sup>r</sup> Hamiltonian . . . . .	109
VI. LINE STRENGTHS IN THE $\nu_2$ BAND OF H <sub>2</sub> S - COMPARISON TO RIGID ROTOR LINE STRENGTHS . . . . .	127
VII. NUCLEAR QUADRUPOLE HYPERFINE STRUCTURE IN THE INFRARED SPECTRUM OF HYDROGEN IODIDE . . . . .	134
A. Introduction . . . . .	134
B. Nuclear Quadrupole Interaction Theory . . . . .	134
C. Experimental Considerations . . . . .	137
D. Results . . . . .	137
APPENDIX A. PLANARITY RELATIONS AND DETERMINABLE CONSTANTS . . . . .	142
APPENDIX B. CORRELATION TABLES FOR MOLECULAR CONSTANTS OF GROUND AND $\nu_2 = 1$ EXCITED STATES OF H <sub>2</sub> S . . . . .	145
BIBLIOGRAPHY . . . . .	154

## LIST OF TABLES

<u>Table</u>	<u>Page</u>
II-1	Coordinate Representations . . . . . 19
II-2	Character Table for V(a, b, c) . . . . . 20
IV-1	Spline Fit Coefficients for Index of Refraction of Germanium . . . . . 61
IV-2	Etalon Errors . . . . . 62
IV-3	Diode Laser Calibration Accuracy Tests . . . . . 63
IV-4	Measured Transition Frequencies in $\nu_2$ Band of H <sub>2</sub> S . . . . . 64
IV-5	Measured Line Strengths in $\nu_2$ Band of H <sub>2</sub> S . . . . . 81
V-1	Standard Deviation of Ground and Upper State Fits . . . . . 95
V-2	Molecular Constants for Ground State, AS Form, I <sup>r</sup> Representation . . . . . 97
V-3	Molecular Constants for Ground State, AS Form, III <sup>r</sup> Representation . . . . . 98
V-4	Molecular Constants for Ground State, NS Form, I <sup>r</sup> Representation . . . . . 99
V-5	Molecular Constants for Ground State, NS Form, III <sup>r</sup> Representation . . . . . 100
V-6	Molecular Constants for Upper State of $\nu_2$ Band, AS Form, I <sup>r</sup> Representation . . . . . 101
V-7	Molecular Constants for Upper State of $\nu_2$ Band, AS Form, III <sup>r</sup> Representation . . . . . 102
V-8	Molecular Constants for Upper State of $\nu_2$ Band, NS Form, I <sup>r</sup> Representation . . . . . 103
V-9	Molecular Constants for Upper State of $\nu_2$ Band, NS Form, III <sup>r</sup> Representation . . . . . 104
V-10	Molecular Constants for Ground State, Typke's Hamiltonian, III <sup>r</sup> Representation - From Gillis and Edwards <sup>(17)</sup> . . . . . 108
V-11	Molecular Constants for Ground State, AS Form, III <sup>q</sup> Representation - From Helminger et al. <sup>(16)</sup> . . . . . 111
V-12	Molecular Constants for Ground State, AS Form, III <sup>r</sup> Representation - From Gillis and Edwards <sup>(17)</sup> . . . . . 112

<u>Table</u>	<u>Page</u>
V-13	Determinable Constants for Best Ground State Fits . . . . . 114
V-14	Determinable Constants for Best Upper State Fits (cm <sup>-1</sup> ) . . . . . 115
V-15	Determinable Constants for Best Upper State Fits (MHz) . . . . . 116
V-16	GF/ENF Factors – Best Ground State Fits . . . . . 117
V-17	GF/ENF Factors – Best $\nu_2$ Band Fits . . . . . 118
V-18	$s_{111}$ Parameter Calculations . . . . . 122
VII-1	Observed Splittings in P(1) of HI . . . . . 140
VII-2	Observed Difference in Quadrupole Coupling Constant from Ground to 1st Excited Vibrational State . . . . . 141
B-1	Correlation Table, AS Form, I <sup>F</sup> Representation, $\nu_2 = 1$ Upper State Fit, Ground State Fixed at Best Fit Values. . . . . 146
B-2	Correlation Table, AS Form, III <sup>F</sup> Representation, $\nu_2 = 1$ Upper State Fit, Ground State Fixed at Best Fit Values. . . . . 147
B-3	Correlation Table, NS Form, I <sup>F</sup> Representation, $\nu_2 = 1$ Upper State Fit, Ground State Fixed at Best Fit Values. . . . . 148
B-4	Correlation Table, NS Form, III <sup>F</sup> Representation, $\nu_2 = 1$ Upper State Fit, Ground State Fixed at Best Fit Values. . . . . 149
B-5	Correlation Table, AS Form, I <sup>F</sup> Representation, Ground State Fit Using Microwave H <sub>2</sub> S Frequencies and Ground State Combination Differences . . . . . 150
B-6	Correlation Table, AS Form, III <sup>F</sup> Representation, Ground State Fit Using Microwave H <sub>2</sub> S Frequencies and Ground State Combination Differences . . . . . 151
B-7	Correlation Table, NS Form, I <sup>F</sup> Representation, Ground State Fit Using Microwave H <sub>2</sub> S Frequencies and Ground State Combination Differences . . . . . 152
B-8	Correlation Table, NS Form, III <sup>F</sup> Representation, Ground State Fit Using Microwave H <sub>2</sub> S Frequencies and Ground State Combination Differences . . . . . 153

## LIST OF FIGURES

<u>Figure</u>		<u>Page</u>
II-1	H <sub>2</sub> S Geometry, Center of Mass at Origin . . . . .	19
II-2	The $\nu_2$ Vibration of H <sub>2</sub> S . . . . .	24
III-1	Diode Laser Spectrometer . . . . .	31
III-2	Germanium Etalon and Temperature Stabilized Copper Holder . . . . .	34
III-3	Diode Laser Spectrometer Electronics . . . . .	36
III-4	Diode Laser Spectrum of H <sub>2</sub> S and N <sub>2</sub> O Near 1149.4 cm <sup>-1</sup> . . . . .	40
III-5	Diode Laser Spectrum of H <sub>2</sub> S and N <sub>2</sub> O Near 1149.7 cm <sup>-1</sup> . . . . .	41
III-6	Diode Laser Spectrum of H <sub>2</sub> S and N <sub>2</sub> O Near 1120 cm <sup>-1</sup> . . . . .	42
III-7	Diode Laser Spectrum of H <sub>2</sub> S and N <sub>2</sub> O Near 1123 cm <sup>-1</sup> . . . . .	43
III-8	Diode Laser Spectrum of H <sub>2</sub> S and N <sub>2</sub> O Near 1140 cm <sup>-1</sup> . . . . .	44
III-9	Diode Laser Spectrum of H <sub>2</sub> S and N <sub>2</sub> O Near 1129 cm <sup>-1</sup> . . . . .	45
III-10	Diode Laser Spectrum of H <sub>2</sub> S and N <sub>2</sub> O Near 1128 cm <sup>-1</sup> . . . . .	46
III-11	Diode Laser Spectrum of H <sub>2</sub> S and CO <sub>2</sub> Near 1095.7 cm <sup>-1</sup> . . . . .	47
III-12	Diode Laser Spectrum of H <sub>2</sub> S and CO <sub>2</sub> Near 1098 cm <sup>-1</sup> . . . . .	48
III-13	Diode Laser Spectrum of H <sub>2</sub> S and CO <sub>2</sub> Near 1090 cm <sup>-1</sup> . . . . .	49
III-14	Diode Laser Spectrum of H <sub>2</sub> S and N <sub>2</sub> O Near 1120.5 cm <sup>-1</sup> . . . . .	50
III-15	Diode Laser Spectrum of H <sub>2</sub> S Near 1099 cm <sup>-1</sup> . . . . .	51
III-16	Diode Laser Spectra of $6_{15} - 7_{26}$ and $6_{25} - 7_{16}$ H <sub>2</sub> S Transitions at Different Optical Depths . . . . .	52
III-17	Diode Laser Spectrum of H <sub>2</sub> S Near 1229.34 cm <sup>-1</sup> . . . . .	53
III-18	Diode Laser Spectrum of H <sub>2</sub> S Near 1257 cm <sup>-1</sup> . . . . .	54
IV-1	Correction to Measured Line Strengths, $S_M$ , as a Function of $y = \gamma_L/\gamma_D \sqrt{\ln 2}$ . . . . .	71
IV-2	Correction to Measured Line Strength, $S_D$ , for a Lorentzian Laser Lineshape . . . . .	74

<u>Figure</u>	<u>Page</u>
IV-3	Correction to Measured Line Strength, $S_D$ , for a Gaussian Laser Lineshape . . . . . 75
V-1	Stick Spectrum of $\nu_2$ Band of $H_2S$ with Experimentally Observed Lines Indicated, Theoretical Rigid Rotor Strengths Used in this Plot . . . . . 87
V-2	Stick Spectrum of $\nu_2$ Band of $H_2S$ , Theoretical Rigid Rotor Strengths Used in this Plot . . . . . 89
VI-1	Stick Spectrum of Observed Line Strengths and Rigid Rotor Line Strengths . . . . . 130
VI-2	Ratio of Observed Line Strengths to Calculated Rigid Rotor Line Strengths (F Factor) . . . . . 131
VII-1	Observed and Calculated Profiles of P(1), P(2), and P(3) of HI . . . . . 138



# CHAPTER I

## INTRODUCTION

Information about the geometry, potential function, and electric dipole moment function of a molecule can be obtained from a quantitative study of its vibration-rotation spectrum. As the experimental methods of infrared molecular spectroscopy improve, better molecular models can be constructed from the interpretation of the observed spectra. Accurate experimental studies of molecular vibration-rotation spectra are also important for a number of diverse applications such as laser isotope separation and the study of planetary atmospheres (including the Earth's atmosphere).

The development of tunable diode lasers has made it possible to obtain molecular spectra in the  $500\text{ cm}^{-1}$  to  $2500\text{ cm}^{-1}$  spectral region with essentially Doppler limited resolution. Very precise spectroscopic measurements can be made with diode lasers in a relatively straightforward manner without complex instrumentation. The high resolution of diode lasers makes them very attractive for the measurement of absorption line strengths, an aspect of molecular vibration-rotation spectra that is much less studied than transition frequencies. Tunable diode lasers can also be used to measure transition frequencies if absorption frequency standards are available in the spectral region under study.

In this work, a tunable diode laser spectrometer was constructed and used to study the effects of centrifugal distortion on the transition frequencies and strengths of the  $\nu_2$  band of  $\text{H}_2\text{S}$ . Some additional line frequencies in the  $\nu_2$  band were measured with a high resolution grating spectrometer. A study of nuclear quadrupole hyperfine structure in the low J lines of the 1-0 band of HI was also made with the diode laser spectrometer and will be presented here.

The main portion of this work is concerned with the  $\nu_2$  vibration-rotation band of  $\text{H}_2\text{S}$ , centered at  $1180\text{ cm}^{-1}$ . While the spectra of light asymmetric rotors such as  $\text{H}_2\text{S}$  and  $\text{H}_2\text{O}$  have been understood qualitatively for many years, the quantitative characterization

of both their energy levels and transition strengths has remained a difficult problem. This is due in part to the relatively large effects of centrifugal distortion on the spectra of light asymmetric rotors. Since the  $\nu_2$  vibration of  $\text{H}_2\text{S}$  is largely unperturbed by other vibrations of the molecule, this band is ideal for a study of the effects of centrifugal distortion without other complicating interactions. Also, the  $\nu_1$  and  $\nu_2$  vibrational bands of  $\text{H}_2\text{S}$  exhibit what are perhaps the largest intensity perturbations due to centrifugal distortion ever observed in the spectrum of an asymmetric rotor.

In a low resolution ( $\approx 5 \text{ cm}^{-1}$ ) study of the  $\nu_2$  band, Emerson and Eggers<sup>(1)</sup> found that the P branch region of this band is about five times less intense than the R branch region. They were able to qualitatively account for the observed intensity anomalies by including centrifugal distortion in a calculation of the line strengths of this band. Since their work, no further studies of the strengths in this band have been made. In fact, no individual line strengths in the infrared spectrum of  $\text{H}_2\text{S}$  have ever been measured.

The only previous rotational analysis of the line frequencies in the  $\nu_2$  band of  $\text{H}_2\text{S}$  was performed by Allen and Plyler.<sup>(2)</sup> They assigned 55 transitions from  $1080 \text{ cm}^{-1}$  to  $1257 \text{ cm}^{-1}$  from a spectrum recorded with a resolution of  $0.3 \text{ cm}^{-1}$ . They were able to obtain values for the quadratic rotational constants A, B, and C in the upper vibrational state of the  $\nu_2$  band, but no centrifugal distortion constants were determined.

In the present work, a total of 126 line frequencies and 94 line strengths in the  $\nu_2$  band were measured. The line frequencies were successfully fit to several of Watson's reduced rotational Hamiltonians,<sup>(3)</sup> and a number of centrifugal distortion constants in the first excited state of the  $\nu_2$  vibration as well as the quadratic rotational constants were determined. Also, the measured line strengths were compared to calculated rigid rotor strengths in order to determine the magnitude of the centrifugal distortion perturbations. The line strengths measured here should serve as a stringent test of the existing theories of centrifugal distortion perturbations in light asymmetric rotor line strengths.

In Chapter II, the derivation of Watson's reduced rotational Hamiltonian is summarized as well as the basic theory of line strengths in asymmetric rotor vibration-rotation spectra.

Chapters III and IV deal with the experimental portion of this work. In Chapter III, the diode laser spectrometer is discussed and several examples of spectra of  $\text{H}_2\text{S}$  taken with this instrument are presented. The determination of the  $\text{H}_2\text{S}$  line frequencies and strengths from the diode laser spectra is outlined in Chapter IV and a detailed error analysis given.

The least-squares analysis of the observed  $\nu_2$  band frequencies using Watson's AS and NS reduced Hamiltonians is presented in Chapter V. Successful fits to the frequencies were obtained using the AS Hamiltonian in the  $I^r$  coordinate representation, and the NS Hamiltonian in both the  $I^r$  and  $III^r$  representations. The AS Hamiltonian in the  $III^r$  representation, though, was unexpectedly found to fit the frequencies very poorly. A large part of Chapter V deals with the characteristics of this particular Hamiltonian and why it fits the frequencies so poorly.

In Chapter VI the results of the  $\text{H}_2\text{S}$  line strength measurements are compared to calculated rigid rotor line strengths. The dependence of the observed line strength perturbations on  $J$ ,  $K_a$ , and  $K_c$  is also examined.

In Chapter VII, the study of nuclear quadrupole hyperfine structure in the 1-0 vibration-rotation band of hydrogen iodide near  $2200\text{ cm}^{-1}$  is presented. Using the diode laser spectrometer the R(0), P(1), P(2), and P(3) lines of this band were recorded, all of which exhibit nuclear quadrupole hyperfine structure. Nuclear quadrupole splittings, which arise from the interaction of the electric field gradient of the molecular electron cloud with the nuclear electric quadrupole moment, are commonly observed in microwave pure rotational spectra. In infrared molecular spectra, these hyperfine splittings are usually masked by either the Doppler width of the absorption lines or by the low resolution of the spectrometer being used to record the spectrum.

In the case of hydrogen iodide, its extremely large nuclear quadrupole moment and molecular weight combine to give relatively large hyperfine splittings with small Doppler widths. This allowed the resolution of some structure in the low  $J$  transitions of hydrogen iodide using the diode laser spectrometer. From these spectra, the nuclear quadrupole

coupling constant of hydrogen iodide in both the ground and upper vibrational states was determined. It is believed that this is the first observation of nuclear quadrupole hyperfine structure in the vibrational spectrum of a diatomic molecule.

## CHAPTER II

### THEORY OF ASYMMETRIC ROTOR VIBRATION-ROTATION SPECTRA

#### II. A. Development of the Rotational Hamiltonian

The complete molecular Hamiltonian for a polyatomic molecule can be written as

$$H = \sum_{n,e} \frac{P_n^2}{2M_n} + \frac{P_e^2}{2M_e} + V_{nn} + V_{ee} + V_{ne}, \quad (\text{II-1})$$

where  $P_n$  and  $P_e$  are the momentum operators for the nuclei and electrons. The potential energy terms  $V_{nn}$ ,  $V_{ee}$ , and  $V_{ne}$  come from the nucleus-nucleus, electron-electron, and nucleus-electron interactions respectively. A great simplification to  $H$  can be made using the Born-Oppenheimer approximation, which is adopted in this work. This approximation assumes that since electrons are much lighter than nuclei, they move much more quickly. Therefore the electron's motion at any time is the same as if the nuclei were fixed at their present instantaneous positions. This allows one to separate Schrödinger's equation into an electronic part, and a vibration-rotation part, to be solved separately. In the electronic wave equation the nuclear positions are taken to be adjustable parameters. In the vibration-rotation wave equation the electronic energy as a function of nuclear position becomes the potential energy term in the Hamiltonian. To solve the vibration-rotation problem we can treat the molecule as a set of point masses representing the nuclei lying in some potential field. With this model the classical Hamiltonian can be developed from which the quantum-mechanical Hamiltonian is obtained by proper replacement of coordinates and their conjugate momenta with the corresponding quantum-mechanical operators.

For a molecule of  $N$  nuclei, there are  $3N$  degrees of freedom. Three of these degrees of freedom describe the translational motion of the molecular center of mass thus leaving  $3N-3$  degrees of freedom to describe the rotation and vibration of the molecule. The rotation can be described by introducing a coordinate system which rotates with the molecule, called the molecule-fixed axes, whose origin is at the molecule's center of mass. Three

coordinates, such as the Euler angles, are required to give the orientation of this axis system with respect to space fixed axes. The remaining  $3N-6$  degrees of freedom are associated with the normal mode vibrations of the molecule, there being three of these for a three atom molecule such as hydrogen sulfide. The molecular vibrations are described relative to the rotating and translating molecule-fixed axes with the normal vibrational coordinates  $Q_i$ .

The classical expression for the molecular kinetic energy is obtained by transforming the kinetic energy in the space fixed frame,  $T = \frac{1}{2} \sum_n M_n \dot{\rho}_n \cdot \dot{\rho}_n$ , to the molecule-fixed axis frame. This was originally done in a rigorous fashion by Wilson and Howard<sup>(4)</sup> who obtained

$$T = \sum_{\alpha, \beta} \frac{1}{2} (J_\alpha - \Pi_\alpha) \mu_{\alpha\beta} (J_\beta - \Pi_\beta) + \frac{1}{2} \sum_i P_i^2 \quad (11-2)$$

where  $\alpha, \beta = x, y, z$  in the molecule-fixed frame and  $i$  runs over the  $3N-6$  normal coordinates. In this expression  $J_\alpha = \partial T / \partial \omega_\alpha$  is the  $\alpha^{\text{th}}$  component of angular momentum,  $\omega_\alpha$  being the  $\alpha^{\text{th}}$  component of the angular velocity of the molecule-fixed axes.  $\Pi_\alpha$  is a quantity close to the vibrational angular momentum about the  $\alpha$  axis but has some contributions from the rotational motion and is not conjugate to any particular angular coordinate. The term  $\mu_{\alpha\beta}$  is a function of the normal coordinates and is almost, but not quite, equal to the instantaneous inverse moment of inertia tensor.  $P_i = \partial T / \partial \dot{Q}_i$  is the momentum due to vibration and is conjugate to the normal coordinate  $Q_i$ . The translational energy of the molecule has been left out of the kinetic energy expression. Complete definitions of the terms used here can be found in several places<sup>(5,6)</sup>. It is assumed that the potential  $V$  can be written solely as a function of the normal coordinates  $Q_i$ . In the limit of small vibrations only terms in  $Q_i^2$  will appear in the potential.

The quantum-mechanical Hamiltonian has been derived from the classical expression by Wilson and Howard<sup>(4)</sup>, Darling and Dennison<sup>(7)</sup>, and more recently by Watson<sup>(8)</sup>. Its derivation from the classical Hamiltonian is non-trivial because the  $\Pi_\alpha$  momentum term is not conjugate to any coordinate. The rather complicated original expressions for the rotational Hamiltonian in references<sup>(4)</sup> and <sup>(7)</sup> have been considerably simplified by Watson to give

$$H = \frac{1}{2} \sum_{\alpha, \beta} (J_{\alpha} - \Pi_{\alpha}) \mu_{\alpha\beta} (J_{\beta} - \Pi_{\beta}) + \frac{1}{2} \sum_i (P_i^2 + V(Q_i)) + U \quad (\text{II-3})$$

where  $J_{\alpha}$ ,  $\Pi_{\alpha}$ ,  $P_i$  are the quantum mechanical momentum operators corresponding to the previously given classical quantities. The extra term  $U = \sum_{\alpha} -1/8 \mu_{\alpha\alpha}$  is a function only of coordinates and not momenta and therefore can be considered as part of the potential energy.

As written, this Hamiltonian is too complicated for any practical calculations of molecular vibration-rotation energy levels. It is customary to simplify it by expanding the potential  $V$  and the effective inverse moment of inertia tensor  $\mu_{\alpha\beta}$  about equilibrium values as a Taylor series in the normal coordinates  $Q_i$ . For reasonably rigid molecules this series converges fairly rapidly. For light asymmetric top molecules such as  $\text{H}_2\text{S}$  and  $\text{H}_2\text{O}$ , though, this series converges relatively slowly because some components of  $\mu_{\alpha\beta}$  diverge for large values of the bending mode normal coordinate. A perturbation calculation can then be made by performing a series of contact or unitary transformations on the expanded Hamiltonian to make it diagonal in vibration quantum number to the required degree of accuracy<sup>(4,9)</sup>. This results in an effective rotational Hamiltonian for each vibrational state, so that we can write  $H = H_{\text{R}}^{\text{V}} + H_{\text{V}}$ , where the rotational parameters in  $H_{\text{R}}^{\text{V}}$  will depend on the vibrational state of the molecule. From now on we will write  $H_{\text{R}}^{\text{V}}$  as just  $H_{\text{R}}$ , remembering that this  $H_{\text{R}}$  is for a particular vibrational state. The zero order term for  $H_{\text{V}}$  is

$$H_{\text{V}}^0 = \frac{1}{2} \sum_i^{3N-6} (P_i^2 + \lambda_i Q_i^2), \quad (\text{II-4})$$

which represents a set of uncoupled harmonic oscillators with energy eigenvalues

$$E_{\text{V}} = \sum_{i=1}^{3N-6} h \nu_i (n_i + \frac{1}{2}), \quad (\text{II-5})$$

where the  $\nu_i$  are the  $3N-6$  normal vibrational mode frequencies given by  $\nu_i = \frac{1}{2\pi} \sqrt{\lambda_i}$ , the  $n_i = 0, 1, 2, 3, \dots$  are the vibrational quantum numbers, and  $h$  is Planck's constant. If there are no resonances between vibrations one then need only be concerned with diagonalizing the rotational Hamiltonian in order to calculate the rotational energies. In this work we are mainly

concerned with rotational structure within a given vibrational band and will not be further concerned with the details of the purely vibrational terms in the Hamiltonian. Approximations to  $H_R$  will now be discussed for the specific case of an asymmetric rotor which has three unequal principal moments of inertia.

The lowest order approximation for  $H_R$  in a given vibrational state is

$$H_R \approx H_{\text{rigid}} = \frac{1}{2} \sum_{\alpha, \beta} \bar{\mu}_{\alpha\beta} J_\alpha J_\beta \quad (\text{II-6})$$

where the  $\bar{\mu}_{\alpha\beta}$  are constant effective values for the inverse moment of inertia tensor. These  $\bar{\mu}_{\alpha\beta}$  come from integrals of the  $\mu_{\alpha\beta}$  over the vibrational wavefunctions. If the molecular axes are rotated so they are identical to the principal axes of inertia then  $\bar{\mu}_{\alpha\beta}$  is reduced to diagonal form giving  $H_{\text{rigid}} = X'J_x^2 + Y'J_y^2 + Z'J_z^2$  where  $X', Y', Z' = 1/2I_x, 1/2I_y, 1/2I_z$  and  $I_x, I_y, I_z$  are the principal moments of inertia expressed in proper units. If the angular momentum operators  $J_x, J_y, J_z$  are written in units of  $\hbar \equiv h/2\pi$  then  $X', Y', Z'$  will be defined to be in units of wavenumbers ( $\text{cm}^{-1}$ ) so that all energies in this work can be expressed in this convenient unit. Infrared transition frequencies and molecular constants will also be given in the  $\text{cm}^{-1}$  unit, remembering that to obtain the true frequency one must multiply the quantity given in wavenumber units by the speed of light. Microwave transitions and molecular constants will be given in MHz, as is normally done.

The next order approximation to  $H_R$ , derived by Wilson and Howard<sup>(4)</sup>, is

$$H_R = \frac{1}{2} \sum_{\alpha, \beta} \bar{\mu}_{\alpha\beta} J_\alpha J_\beta + \frac{1}{4} \sum_{\alpha, \beta, \gamma, \delta} \tau_{\alpha\beta\gamma\delta} J_\alpha J_\beta J_\gamma J_\delta \quad (\text{II-7})$$

where the  $\tau_{\alpha\beta\gamma\delta}$  are given to a very good approximation by<sup>(10)</sup>

$$\tau_{\alpha\beta\gamma\delta} = -\frac{1}{2} \sum_{i, j} \mu_{\alpha\beta}^{(i)} (F^{-1})_{ij} \mu_{\gamma\delta}^{(j)}$$

The indices  $i$  and  $j$  run over some set of  $3N-6$  internal displacement coordinates  $R_i$  which are used to evaluate  $\mu_{\alpha\beta}^{(i)} \equiv (\partial\mu_{\alpha\beta}/\partial R_i)_e$ , where the  $e$  stands for evaluating  $\partial\mu_{\alpha\beta}/\partial R_i$  at equilibrium.  $F^{-1}$  is the inverse force field matrix written in terms of the coordinates  $R_i$ . The



equation for  $\tau_{\alpha\beta\gamma\delta}$  assumes a harmonic force field and that higher order terms in the expansion of  $\mu_{\alpha\beta}$  are negligible. The dependence of the  $\tau_{\alpha\beta\gamma\delta}$  on the inverse of the force constant matrix is physically reasonable since the smaller the force constants of the molecule the more it will distort at higher rotational states, and therefore the bigger the  $\tau_{\alpha\beta\gamma\delta}$ . For a general asymmetric rotor there are 21 non-zero  $\tau_{\alpha\beta\gamma\delta}$  which together take on only nine distinct values. The rest of the  $\tau_{\alpha\beta\gamma\delta}$  are zero due to symmetry. The nine distinct  $\tau_{\alpha\beta\gamma\delta}$  are  $\tau_{\alpha\alpha\alpha\alpha}$ ,  $\tau_{\alpha\alpha\beta\beta} = \tau_{\beta\beta\alpha\alpha}$ ,  $\tau_{\alpha\beta\alpha\beta} = \tau_{\alpha\beta\beta\alpha} = \tau_{\beta\alpha\beta\alpha} = \tau_{\beta\alpha\alpha\beta}$  for  $\alpha, \beta = x, y, z$ .

It was later shown by Kivelson and Wilson<sup>(11)</sup> that by use of the angular momentum commutation relations the  $H_R$  given by Wilson and Howard can be written in the more simple form

$$H_R = XJ_x^2 + YJ_y^2 + ZJ_z^2 + \frac{1}{4} \sum_{\alpha, \beta} \tau'_{\alpha\alpha\beta\beta} J_\alpha^2 J_\beta^2 \quad (\text{II-8})$$

where  $\tau'_{xxxx} = \tau_{xxxx}$ ,  $\tau'_{yyyy} = \tau_{yyyy}$ ,  $\tau'_{zzzz} = \tau_{zzzz}$

$$\tau'_{xxyy} = \tau_{xxyy} + 2\tau_{xyxy}$$

$$\tau'_{yyzz} = \tau_{yyzz} + 2\tau_{yzyz}$$

$$\tau'_{xxzz} = \tau_{xxzz} + 2\tau_{xzxz}$$

$$X = X' + \frac{1}{4}(3\tau_{xyxy} - 2\tau_{xzxz} - 2\tau_{yzyz})$$

$$Y = Y' + \frac{1}{4}(3\tau_{yzyz} - 2\tau_{xyxy} - 2\tau_{xzxz})$$

$$Z = Z' + \frac{1}{4}(3\tau_{xzxz} - 2\tau_{xyxy} - 2\tau_{yzyz}).$$

By use of the commutation relations it has been shown that there are really only six independent distortion constants for a general asymmetric rotor and also that the quadratic coefficients depend upon the original quartic coefficients.

For a planar asymmetric top molecule such as  $H_2S$ , Dowling<sup>(12)</sup> has shown that the six independent  $\tau'$  coefficients reduce to four independent coefficients. His relations between the quartic coefficients are only strictly valid for a harmonic approximation to the force

field and for the equilibrium coefficients, not vibrationally averaged ones that are observed in practice. If the observed energy levels of a molecule are extremely accurate then the use of these relations in the Hamiltonian can lead to a poor fit of the data because of these two approximations. The relations obtained by Dowling are given in Appendix A.

It is important to know how many independent sets of constants there are in  $H_R$  because only the independent constants (which may be combinations of fundamental molecular constants) can be derived from a molecular spectrum. When accurate rotational energy levels of a non-planar asymmetric molecule were fit with Kivelson and Wilson's  $H_R$ , the quartic distortion constants were found to be indeterminate, although the observed energy levels could be accurately reproduced with the constants obtained in the fit. Watson<sup>(13)</sup> showed that the matrix elements of the six Kivelson and Wilson's distortion operators were linearly dependent on each other, therefore leading to their indeterminate value in the least-squares fitting process. In doing so, Watson developed a general method for developing rotational Hamiltonians to high orders in angular momentum operators that insures independence of the matrix elements of the effective operators. This enables a unique set of distortion constants to be determined. The Hamiltonians developed by Watson were used in this work since they can be easily expanded to the high orders of angular momentum required to fit light asymmetric rotors. A summary of Watson's development of the rotational Hamiltonian will now follow. This summary will go into some detail on those points important for the interpretation of the fits performed in this work on  $H_2S$  rotational data.

## II. B. Watson's Reduced Rotational Hamiltonian

Watson developed a procedure to deal with the problem of indeterminate distortion coefficients by systematically making use of the fact that the eigenvalues of  $H_R$  do not change when it is transformed with some arbitrary unitary operator. By choosing the unitary operator to be a power series in angular momentum operators, the transformed Hamiltonian becomes a power series like the original one but with different coefficients for the angular momentum operators. One can then choose the arbitrary parameters specifying the unitary

operator to eliminate as many terms as possible from the transformed  $H_R$ , resulting in what is called a reduced Hamiltonian. Alternative methods of reducing  $H_R$  result in different individual coefficients but not in independent combinations of coefficients for operators, which are always the same. The remaining terms are then the maximum number that can be determined from the rotational energy levels. It should be remembered that since an arbitrary unitary transformation of the Hamiltonian does not change the eigenvalues; only those combinations of coefficients not dependent upon the arbitrary parameters in the unitary transformation are determinable.

The steps required to obtain the reduced Hamiltonians used in this work will now be outlined. The following discussion will concentrate only on the effects of the unitary transformations on the quadratic and quartic coefficients for simplicity. The transformation of higher order coefficients and subsequent reduction of the Hamiltonian is analogous to that of the lower order ones. For detailed discussions of this theory one can refer to papers by Watson<sup>(3,13,14)</sup>.

If there are no vibrational degeneracies or resonances present for a particular vibrational state of a molecule, then the effective rotational Hamiltonian,  $H_R$ , for that state is a power series in components of the total angular momentum operators  $J_x$ ,  $J_y$ , and  $J_z$ . Watson has shown that if one takes the angular momentum commutation relations into account,  $H_R$  can always be written in the so-called standard form

$$H_R = \sum_{p,q,r} h_{pqr} (J_x^p J_y^q J_z^r + J_z^r J_y^q J_x^p) \quad (II-9)$$

where  $p, q, r = 0, 1, 2, \dots$  and the  $h_{pqr}$  are constant coefficients. This expression is constrained by the fact that  $H_R$  must be Hermitian and time reversal invariant. This requires the sum  $p + q + r$  to be equal to an even integer and the  $h_{pqr}$  to be real. For molecules with orthorhombic point groups, a number of the  $h_{pqr}$  can be shown to equal zero. For a general (non-orthorhombic) molecule, Watson showed that the  $H_R$  of equation II-9 can be transformed to look like the  $H_R$  of an orthorhombic molecule, which when written up to sixth power in angular momentum, is given by

$$\begin{aligned}
H_R = & XJ_x^2 + YJ_y^2 + ZJ_z^2 + \sum_{\alpha,\beta} T_{\alpha\beta} J_\alpha^2 J_\beta^2 \\
& + \sum_{\alpha} \phi_{\alpha\alpha\alpha\alpha} J_\alpha^6 + \sum_{\alpha \neq \beta} \phi_{\alpha\alpha\beta} (J_\alpha^4 J_\beta^2 + J_\beta^2 J_\alpha^4) \\
& + \phi_{xyz} (J_x^2 J_y^2 J_z^2 + J_z^2 J_y^2 J_x^2). \tag{II-10}
\end{aligned}$$

The coefficients  $T_{\alpha\beta}$  in this equation are related to Kivelson and Wilson's parameters by  $T_{\alpha\beta} = \frac{1}{4} \tau'_{\alpha\alpha\beta\beta}$ . Note that at this point there are six quartic and ten sextic coefficients. This series can be written to higher powers in  $J$  if necessary. The transformed  $H_R$  is given by

$$\tilde{H}_R = U^{-1} H_R U \tag{II-11}$$

where Watson chose

$$U = e^{iS_3} e^{iS_5} e^{iS_7} \dots \tag{II-12}$$

with

$$\begin{aligned}
S_3 = & s_{111} (J_x J_y J_z + J_z J_y J_x) \text{ and} \\
S_5 = & s_{311} (J_x^3 J_y J_z + J_z J_y J_x^3) \\
& + s_{131} (J_x J_y^3 J_z + J_z J_y^3 J_x) \\
& + s_{113} (J_x J_y J_z^3 + J_z^3 J_y J_x) \tag{II-13}
\end{aligned}$$

and so on so that  $U$  is unitary and time reversal invariant as required. If we write  $H_R = H_2 + H_4 + H_6 + \dots$  where  $H_n$  contains terms to the  $n^{\text{th}}$  power of angular momentum and write

$$\tilde{H}_R = U^{-1} H_R U = \tilde{H}_2' + \tilde{H}_4' + \tilde{H}_6' + \dots \tag{II-14}$$

then the transformed  $\tilde{H}_R$  terms are given to first order by<sup>(3)</sup>

$$\tilde{H}_2' = H_2$$

$$\tilde{H}_4' = H_4 + i[H_2, S_3]$$

$$\tilde{H}_6' = H_6 + i[H_4, S_3] - \frac{1}{2}[[H_2, S_3], S_3] + i[H_2, S_5] \quad (\text{II-15})$$

where  $[A, B] = AB - BA$ . The relations given here for the  $\tilde{H}_n'$  only contain terms from the transformation that are the same order of magnitude as the untransformed  $H_n$  terms, any smaller terms have been dropped. The transformation has been carried out using the approximation  $e^{iS_n} \approx 1 + iS_n$  which is unitary to order  $S_n^2$ . This is a relatively accurate procedure if the parameters  $s_{111}, s_{311}, s_{131}, s_{113}$ , etc. are chosen to be small enough. When  $\tilde{H}_R$  is re-written in the standard form previously introduced by using the commutation relations on each of the  $\tilde{H}_n'$  expressions, terms of lower degree than  $\tilde{H}_n'$  may be produced. The resulting terms of similar magnitude can be collected together again to give  $\tilde{H}_R = \tilde{H}_2 + \tilde{H}_4 + \tilde{H}_6 + \dots$ . In order for  $\tilde{H}_R$  to converge as well as  $H_R$  the unitary transformation parameters should be chosen so that  $s_{111} \sim T/B$  and  $s_{131}, s_{311}, s_{113} \sim \phi/B$  where  $B, T$ , and  $\phi$  are on the order of the untransformed quadratic, quartic, and sextic coefficients in  $H_R$ . The transformed quadratic and quartic coefficients are, from equation II-15,

$$\tilde{X} = X + 4(Z - Y) s_{111}$$

$$\tilde{Y} = Y + 4(X - Z) s_{111}$$

$$\tilde{Z} = Z + 4(Y - X) s_{111}$$

$$\tilde{T}_{xx} = T_{xx}, \tilde{T}_{yy} = T_{yy}, \tilde{T}_{zz} = T_{zz}$$

$$\tilde{T}_{yz} = T_{yz} + 2(Z - Y) s_{111}$$

$$\tilde{T}_{xz} = T_{xz} + 2(X - Z) s_{111}$$

$$\tilde{T}_{xy} = T_{xy} + 2(Y - X) s_{111} \quad (\text{II-16})$$

It should be noted that the relative changes in the quadratic coefficients are much smaller than those in the quartic coefficients. A typical transformed sextic coefficient is

$$\begin{aligned} \tilde{\phi}_{yyz} = & \phi_{yyz} + 2(Z - Y) s_{131} - 4(T_{yy} - T_{yz}) s_{111} \\ & + 4(Z - Y) s_{111}^2. \end{aligned} \quad (\text{II-17})$$

All the transformed sextic coefficients are given by Watson<sup>(14)</sup> and the higher order contributions for the quadratic and quartic coefficients are given by Typke<sup>(15)</sup>.

A set of quartic coefficient combinations that do not depend, to a very good approximation, upon the unitary transformation parameters are

$$\begin{aligned} T_{xx}, T_{yy}, T_{zz}, \quad T_1 = T_{yz} + T_{xz} + T_{xy}, \text{ and} \\ T_2 = XT_{yz} + YT_{xz} + ZT_{xy}. \end{aligned} \quad (\text{II-18})$$

These quantities can therefore be chosen as a set of determinable quartic coefficients. This choice for the determinable coefficients is only one out of an infinite number of possibilities, but any other choice for a set of determinable combinations can be expressed in terms of those given above. For the sextic part of  $\tilde{H}_R$  there are seven determinable combinations of coefficients. In general there are  $n+1$  independent terms in  $H_R$  of degree  $n$ .

We now wish to write  $\tilde{H}_R$  in a form convenient for calculation by using the operators  $J_x^2, J_y^2, J_z^2, J_{\pm} = J_x \pm iJ_y$  instead of  $J_x, J_y,$  and  $J_z$ . This is normally done for the calculation of asymmetric rotor energy levels due to the algebraic complexity of the matrix elements of  $H_R$  if the operators  $J_x, J_y,$  and  $J_z$  are used. In terms of these operators,  $H_R$  has the form

$$\begin{aligned} H_R = & B_{200} J^2 + B_{020} J_z^2 + B_{002} (J_+^2 + J_-^2) + T_{400} J^4 + T_{220} J^2 J_z^2 \\ & + T_{040} J_z^4 + T_{202} J^2 (J_+^2 + J_-^2) + \frac{1}{2} T_{022} [J_z^2 (J_+^2 + J_-^2) \\ & + (J_+^2 + J_-^2) J_z^2] + T_{004} (J_+^4 + J_-^4) + \text{higher order terms.} \end{aligned} \quad (\text{II-19})$$

The relationship between these coefficients and the previously used ones in  $H_R$  are given by Watson<sup>(3)</sup>. The subscripts of the coefficients refer to the powers of  $J, J_z$  and  $J_{\pm}$  in the operator for each coefficient. For example, the quadratic coefficients in this form are related to the original ones by

$$\begin{aligned}
B_{200} &= \frac{1}{2} (X + Y) \\
B_{002} &= \frac{1}{4} (X - Y) \\
B_{020} &= Z - \frac{1}{2} (X + Y).
\end{aligned}
\tag{II-20}$$

The transformed quadratic and quartic coefficients in  $\tilde{H}_R$  for this form are

$$\begin{aligned}
\tilde{B}_{200} &= B_{200} + 4 B_{002} s_{111} \\
\tilde{B}_{020} &= B_{020} - 14 B_{002} s_{111} \\
\tilde{B}_{002} &= B_{002} + 2 B_{020} s_{111} \\
\tilde{T}_{400} &= T_{400} - 2 B_{002} s_{111} \\
\tilde{T}_{202} &= T_{202} \\
\tilde{T}_{220} &= T_{220} + 12 B_{002} s_{111} \\
\tilde{T}_{022} &= T_{022} - 2 B_{020} s_{111} \\
\tilde{T}_{040} &= T_{040} - 10 B_{002} s_{111} \\
\tilde{T}_{004} &= T_{004} + B_{002} s_{111}.
\end{aligned}
\tag{II-21}$$

$s_{111}$  can now be chosen to reduce the quartic terms in  $\tilde{H}_R$  from six to five. The most commonly used reduction, called the AS form, is obtained by setting

$$s_{111} = -\frac{T_{004}}{B_{002}} = \frac{4R_6}{(Y-X)}
\tag{II-22}$$

where

$$R_6 = 1/16 [T_{xx} + T_{yy} - 2T_{xy}].
\tag{II-23}$$

This choice for  $s_{111}$  makes  $\tilde{T}_{004} = 0$  so that the operator  $(J_+^4 + J_-^4)$  is dropped from  $\tilde{H}_R$  and is not included in fitting the observed energy levels to  $\tilde{H}_R$ . Similarly, three operators in the sextic part of  $\tilde{H}_R$  can be dropped with proper choices of  $s_{131}$ ,  $s_{311}$ , and  $s_{113}$ . The resulting Hamiltonian, written in the most commonly used notation is

$$H_R^{AS} = H_2^{AS} + H_4^{AS} + H_6^{AS} + \dots
\tag{II-24}$$

where

$$H_2^{AS} = \frac{1}{2}(X^{AS} + Y^{AS}) J^2 + [Z^{AS} - \frac{1}{2}(X^{AS} + Y^{AS})] J_z^2 + \frac{1}{4}(X^{AS} - Y^{AS})(J_+^2 + J_-^2)$$

$$H_4^{AS} = -\Delta_J J^4 - \Delta_{JK} J^2 J_z^2 - \Delta_K J_z^4 - \delta_J J^2 (J_+^2 + J_-^2) - \frac{1}{2} \epsilon_K [J_z^2 (J_+^2 + J_-^2) + (J_+^2 + J_-^2) J_z^2]$$

$$H_6^{AS} = H_J J^6 + H_{JK} J^4 J_z^2 + H_{KJ} J^2 J_z^4 + H_K J_z^6 + h_J J^4 (J_+^2 + J_-^2) + \frac{1}{2} h_{JK} J^2 [J_z^2 (J_+^2 + J_-^2) + (J_+^2 + J_-^2) J_z^2] + \frac{1}{2} h_K [J_z^4 (J_+^2 + J_-^2) + (J_+^2 + J_-^2) J_z^4]$$

$$H_8^{AS} = L_J J^8 + L_{JK} J^6 J_z^2 + L_{JK} J^4 J_z^4 + L_{KKJ} J^2 J_z^6 + L_K J_z^8 + \ell_J J^6 (J_+^2 + J_-^2) + \frac{1}{2} \ell_{JK} J^4 [J_z^2 (J_+^2 + J_-^2) + (J_+^2 + J_-^2) J_z^2] + \frac{1}{2} \ell_{KJ} J^2 [J_z^4 (J_+^2 + J_-^2) + (J_+^2 + J_-^2) J_z^4] + \frac{1}{2} \ell_K [J_z^6 (J_+^2 + J_-^2) + (J_+^2 + J_-^2) J_z^6].$$

This is the most commonly used reduced Hamiltonian because of its relative ease of calculation, which will be discussed in Section II-C.

Another possible reduction of  $H_R$ , that is sometimes used is called the NS form,<sup>(3)</sup> results from setting

$$s_{111} = \frac{T_{022}}{2 B_{020}} = \frac{R_5}{Z - \frac{1}{2}(X - Y)}, \quad (II-25)$$

where

$$R_5 = -1/8 (T_{xx} - T_{yy} - 2T_{xz} + 2T_{yz}). \quad (II-26)$$



This choice for  $s_{111}$  sets  $\tilde{T}_{022} = 0$  so that the term with the operator  $\frac{1}{2} [J_z^2 (J_+^2 + J_-^2) + (J_+^2 + J_-^2) J_z^2]$  is dropped from  $\tilde{H}_R$ . The equations for  $s_{131}$ ,  $s_{311}$ , and  $s_{113}$  for both the AS and NS reductions are given by Watson<sup>(3)</sup>. The NS reduced Hamiltonian can be written

$$H_R^{NS} = H_2^{NS} + H_4^{NS} + H_6^{NS} + \dots \quad (\text{II-27})$$

where

$$H_2^{NS} = \frac{1}{2} (X^{NS} + Y^{NS}) J_z^2 + [Z^{NS} - \frac{1}{2} (X^{NS} + Y^{NS})] J_z^2 \\ + \frac{1}{4} (X^{NS} - Y^{NS}) (J_+^2 + J_-^2)$$

$$H_4^{NS} = -D_J J_z^4 - D_{JK} J_z^2 J_z^2 - D_K J_z^4 \\ + \delta_1 J_z^2 (J_+^2 + J_-^2) + \delta_2 (J_+^4 + J_-^4)$$

$$H_6^{NS} = H'_J J_z^6 + H'_{JK} J_z^4 J_z^2 + H'_{KJ} J_z^2 J_z^4 + H'_K J_z^6 \\ + h_1 J_z^4 (J_+^2 + J_-^2) + h_2 J_z^2 (J_+^4 + J_-^4) \\ + h_3 (J_+^6 + J_-^6)$$

$$H_8^{NS} = L'_J J_z^8 + L'_{JK} J_z^6 J_z^2 + L'_{JK} J_z^4 J_z^4 + L'_{KKJ} J_z^2 J_z^6 \\ + L'_K J_z^8 + \ell_1 J_z^2 (J_+^2 + J_-^2) + \ell_2 J_z^4 (J_+^4 + J_-^4) \\ + \ell_3 J_z^2 (J_+^6 + J_-^6) + \ell_4 (J_+^8 + J_-^8).$$

These two forms for  $\tilde{H}_R$  were used in this work. The  $H_2S$  pure rotational spectrum in the microwave spectral region was fit by Helminger et al.<sup>(16)</sup> using the AS from written in terms of powers of the operator  $J_x^2 - J_y^2$  instead of  $J_z^2$ , which results in some slightly

different operators in  $H_6^{AS}$  and  $H_8^{AS}$ . The microwave data as well as rotational line frequencies in the  $2\nu_2$ ,  $\nu_1$ , and  $\nu_3$  bands of  $H_2S$  have been fit by Gillis and Edwards<sup>(17)</sup> to a reduced Hamiltonian developed by Typke<sup>(15)</sup>, which is very similar to the NS form. Typke also employed powers of the operator  $J_x^2 - J_y^2$  instead of  $J_z^2$  to write  $H_R$ , which again leads to slightly different higher order operators in  $H_R$ .

## II. C. Calculation of the Rotational Energy Levels

In this section the calculation of energy levels from  $H_R$  will be discussed as well as the molecular symmetries which affect this calculation. Unlike a symmetric rotor, the energy levels of an asymmetric rotor, given by  $H_R |\psi\rangle = E_i |\psi\rangle$ , cannot be written in closed form, even in the rigid rotor approximation. To obtain the  $E_i$ , the Hamiltonian matrix is computed in some basis set and is then numerically diagonalized with a computer.

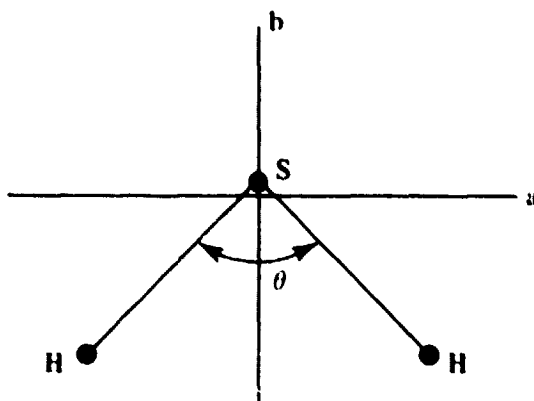
A convenient basis set consists of the symmetric top wavefunctions  $|J, K\rangle$ . The  $M$  dependence of these functions, where  $M$  represents the quantum number corresponding to the  $2J + 1$  orientations of the total angular momentum in the space fixed coordinate system, is not shown because field free rotational energies do not depend upon it. Since the Hamiltonians we have discussed are diagonal in  $J$ , the only matrix elements required for the calculation of the  $E_i$  are  $\langle J, K' | H_R | J, K \rangle$ . The Hamiltonian matrix is block diagonal in  $J$  and can therefore be diagonalized separately for each  $J$  value. The only non-zero matrix elements for a rigid rotor are

$$\begin{aligned} \langle J, K | H_{\text{rigid}} | J, K \rangle &= \frac{1}{2}(X + Y) J(J + 1) + [Z - \frac{1}{2}(X + Y)] K^2 \\ \langle J, K \pm 2 | H_{\text{rigid}} | J, K \rangle &= \frac{1}{4}(X - Y) \{ [J(J + 1) - K(K \pm 1)] * \\ &\quad [J(J + 1) - (K \pm 1)(K \pm 2)] \}^{1/2}, \end{aligned} \quad (\text{II-28})$$

so that  $H_{\text{rigid}}$  is in tri-diagonal form.

The numerical diagonalization of  $H_R$  is facilitated by taking into account the symmetries of asymmetric rotor wavefunctions, which belong to the four-group  $V(a, b, c)$  defined by the three rotation operators  $C_2^a, C_2^b, C_2^c$  and the identity operator  $E$ . The labels  $a, b,$

c denote the molecular axes and are defined by the requirement that the principal moments of inertia satisfy the relation  $I_a < I_b < I_c$ . As shown in Figure II-1, the planar  $H_2S$  molecule lies in the ab plane, with the b axis having 2 fold symmetry.  $C_2^a$ , for example, represents a  $180^\circ$  rotation of the molecule about its a axis. The a, b, c axes of the molecule can be identified with the x, y, z molecular axes used up to now in the six ways shown in



$$\theta \approx 92^\circ$$

c axis  $\perp$  to page

$$r_{H-S} \approx 1.33 \text{ \AA}$$

Figure II-1:  $H_2S$  Geometry, Center of Mass at Origin

Table II-1. The character table for  $V(a, b, c)$  is given in Table II-2, with a +1 representing a symmetric wavefunction for the given operation and a -1 an antisymmetric wavefunction.

TABLE II-1  
Coordinate Representations

	$I^r$	$II^r$	$III^r$	$I^c$	$II^c$	$III^c$
x	b	c	a	c	a	b
y	c	a	b	b	c	a
z	a	b	c	a	b	c

TABLE II-2  
Character Table for V(a, b, c)

Symmetry Species			Operation			
$K_{-1}$	$K_{+1}$	Type	E	$C_2^a$	$C_2^b$	$C_2^c$
ee		A	1	1	1	1
eo		$B_a$	1	1	-1	-1
oo		$B_b$	1	-1	1	-1
oe		$B_c$	1	-1	-1	1

It was observed by Wang<sup>(18)</sup> that the  $|J, K\rangle$  symmetric rotor basis functions do not transform as a representation of the four-group V(a, b, c), while the linear combinations of these functions

$$\begin{aligned}
 |J, O^+\rangle &= |J, O\rangle \\
 |J, K^+\rangle &= 1/\sqrt{2} \{ |J, K\rangle + |J, -K\rangle \} \quad K > 0 \\
 |J, K^-\rangle &= 1/\sqrt{2} \{ |J, K\rangle - |J, -K\rangle \} \quad K > 0
 \end{aligned}
 \tag{II-29}$$

do have this property. For the  $|J, K\rangle$  basis functions  $J^2 |J, K\rangle = J(J+1) |J, K\rangle$  and  $J_z |J, K\rangle = K |J, K\rangle$ , where the z subscript refers to the molecule fixed z axis. If  $H_R$  is set up in this basis, it can be factorized for each J (except J = 0 or 1), into four independent tri-diagonal submatrices. This can be done because the matrix elements connecting  $|J, K^+\rangle$  and  $|J, K^-\rangle$  vanish as well as those connecting even and odd K. For a given J we have

$$H_R^J = E^+ + O^+ + E^- + O^-
 \tag{II-30}$$

where E and O refer to the evenness or oddness of the K values in the matrix elements and the + and - refer to the matrices with only  $|J, K^+\rangle$  or  $|J, K^-\rangle$  matrix elements. This factorization of  $H_R$  is called the Wang transformation. Although the Wang transformation

is not necessary for the computation of the  $E_i$ , it does reduce the size of the matrices that must be diagonalized from  $2J + 1$  by  $2J + 1$  to approximately  $J/2$  by  $J/2$ , which can be a significant reduction in computer memory, especially for high  $J$  values. The diagonalization of the four Wang submatrices gives  $2J + 1$  energy levels for each  $J$  value, which in general are non-degenerate.

The behavior of the energy levels can be described using the parameter  $\kappa$ , where  $\kappa = (2B - A - C)/(A - C)$  and  $A, B, C = 1/2I_a, 1/2I_b, 1/2I_c$  in the proper units. If the moments of inertia of an asymmetric top are varied from the limiting prolate symmetric top ( $B = C$ ) to the limiting oblate symmetric top ( $B = A$ ),  $\kappa$  will vary from  $-1$  to  $+1$ , the most asymmetric top having  $\kappa = 0$ . For  $H_2S$   $\kappa \approx +0.5$  and thus it is a fairly asymmetric rotor. The asymmetric rotor energy levels are generally designated by  $J_{K_a, K_c}$ , where  $K_a$  is the  $K$  value of the limiting symmetric prolate top level ( $\kappa = -1$ ) with which the asymmetric top energy level connects and  $K_c$  is the  $K$  value of the limiting symmetric oblate top level ( $\kappa = +1$ ) with which this same asymmetric top energy level connects. For a given  $J$  the asymmetric top energy levels do not cross, except in extreme cases which were not encountered in this work,<sup>(21)</sup> making this labeling procedure possible. The identification of  $K_a, K_c$  values with the eigenvalues of the Wang submatrices for a given  $J$  can be found in a number of references<sup>(19, 20)</sup> and is easily incorporated into computer programs that calculate asymmetric rotor energy levels. This  $J_{K_a, K_c}$  notation also conveniently gives the symmetry of the rotational wavefunctions from the parity of  $K_a$  and  $K_c$ , as shown in Table II-2.

For the previously discussed AS form of the Hamiltonian the only non-zero matrix elements are

$$\langle J K | H_R^{AS} | J K \rangle \quad \text{and} \quad \langle J K \pm 2 | H_R^{AS} | J K \rangle$$

so that the calculation of the energy levels is identical to that for a rigid rotor, the only modification being the addition of higher degree terms to each matrix element. For the NS

Hamiltonian there are non-zero matrix elements for  $\Delta K = 0, \pm 2, \pm 4,$  and  $\pm 6$ . Still, the Hamiltonian matrix can be Wang factorized and line identifications assigned as for the rigid rotor. The required matrix elements for both the AS and NS Hamiltonians have been tabulated by Kirshner<sup>(21)</sup>.

#### II. D. Vibration-Rotation Line Strengths of an Asymmetric Top Molecule

To interpret the vibration-rotation spectrum of an asymmetric top molecule a knowledge of the transition strengths (and selection rules) as well as the molecular energy levels is required. If the approximation is made that there is no interaction between vibration and rotation, the calculation of the relative line strengths within a vibration-rotation band is straightforward. The relative line strengths obtained using this approximation, which is called the rigid rotor approximation, often agree with experimentally observed line strengths to 30% or better. The  $\nu_2$  band of  $H_2S$ , when observed under low resolution ( $\approx 5\text{cm}^{-1}$ )(22), exhibits an intensity profile very different from a rigid rotor profile. The  $H_2S$  intensity profile, which is characterized by the P branch region being about 1/5 as intense as the R branch region of the band, was studied by Emerson and Eggers,<sup>(1)</sup> who showed that the intensity anomaly is caused by centrifugal distortion of the nonrigid  $H_2S$  molecule. In this section we will discuss the fundamental relations for the vibration-rotation line strengths and also the rigid rotor approximation for these strengths. The approach taken by Emerson and Eggers to include some of the effects of centrifugal distortion in the line strengths will also be summarized.

The line strength is defined to be the integral of the absorption coefficient,  $k(\nu)$ , over the line,

$$S = \int_{\text{over the line}} k(\nu) d\nu. \quad (\text{II-31})$$

In terms of fundamental molecular quantities, the line strength is given by<sup>(19)</sup>

$$S = \frac{8\pi^3 \nu N g_i e^{-E_i/kT}}{3hc Q} (1 - e^{-h\nu/kT}) |\langle \mu \rangle|^2 \quad (\text{II-32})$$

where  $N$  is the number of molecules/cm<sup>3</sup>-atm,  $\nu$  is the frequency of the transition,  $E_i$  is the lower state energy of the transition,  $g_j$  is the statistical weight or degeneracy of the lower state energy level  $E_j$ ,  $Q$  is the vibration-rotation partition function, and  $|\langle \mu \rangle|^2$  is the square of the transition dipole moment matrix element. The partition function is given by

$$Q = \sum_j g_j e^{-E_j/kT} \quad (\text{II-33})$$

where  $E_j$  are the molecular vibration-rotation energy levels.

The square of the dipole moment matrix element is given by

$$|\langle \mu \rangle|^2 = \sum_{F=X,Y,Z} |\langle i | \mu_F | f \rangle|^2 \quad (\text{II-34})$$

where  $\mu_F$  is the component of the dipole moment along the X, Y, or Z space-fixed axes, and  $|i\rangle$  and  $|f\rangle$  are the initial and final states of the transition. In the absence of any external fields the X, Y, and Z components of  $\langle \mu \rangle$  all have the same value so that only one component (the Z component for example) needs to be evaluated, giving

$$|\langle \mu \rangle|^2 = 3 |\langle i | \mu_Z | f \rangle|^2. \quad (\text{II-35})$$

The component of the dipole moment along the space-fixed Z axis can be related to the dipole moment relative to the molecule-fixed axes with the direction cosines,  $\varphi_{Fg}$  by

$$\mu_Z = \sum_{g=a,b,c} \varphi_{Zg} \mu_g, \quad (\text{II-36})$$

where  $g$  is summed over the three molecule-fixed axes, a, b, and c.

The  $\nu_2$  vibration of H<sub>2</sub>S studied in this work is illustrated in Fig. II-2. For this vibration  $\mu_a$  and  $\mu_c$  do not change, so that only  $\mu_b$  needs to be included in equation II-36 for  $\mu_Z$ . The permanent dipole moment of H<sub>2</sub>S is also along the b axis, and gives rise to the pure rotational spectrum of H<sub>2</sub>S. Since H<sub>2</sub>S is a planar molecule  $\mu_c \equiv 0$ . The only time  $\mu_a$  is not zero is during the asymmetric vibration  $\nu_3$ . We can now write the dipole matrix element for the  $\nu_2$  vibration as

$$|\langle \mu \rangle|^2 = 3 |\langle i | \varphi_{Zb} \mu_b | f \rangle|^2. \quad (\text{II-37})$$

At this point, the approximation that there is no interaction between vibration and rotation can be made. This means that  $\mu_b$  does not depend on rotation coordinates and

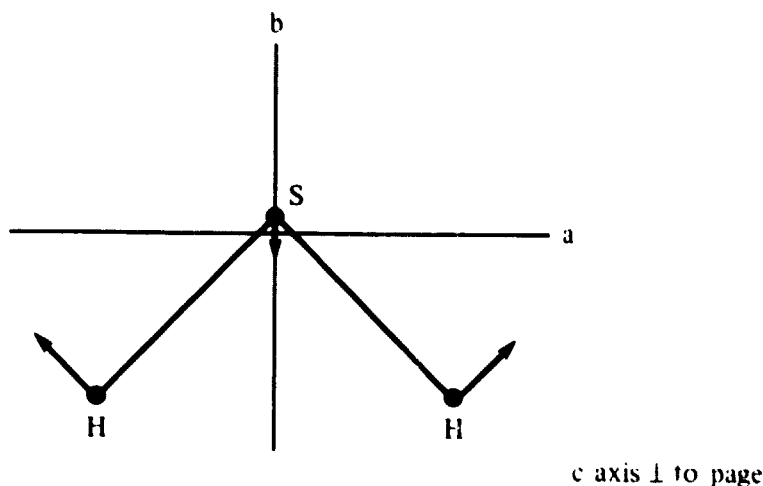


Figure II-2: The  $\nu_2$  Vibration of  $\text{H}_2\text{S}$

that  $|i\rangle$  and  $|f\rangle$  can be separated into vibrational and rotational parts  $|V\rangle$  and  $|R\rangle$ , so that now  $|\langle\mu\rangle|^2$  can be written as

$$|\langle\mu\rangle|^2 = 3 |\langle R_i | \varphi_{Zb} | R_f \rangle|^2 |\langle V_i | \mu_b | V_f \rangle|^2 \quad (\text{II-38})$$

where

$$|i\rangle = |R_i\rangle |V_i\rangle \text{ and } |f\rangle = |R_f\rangle |V_f\rangle.$$

This is called the rigid rotor approximation in this work, although the dependence of  $|R_i\rangle$  and  $|R_f\rangle$  on the average centrifugal distortion within each vibrational state is included when evaluating  $\langle R_i | \varphi_{Zb} | R_f \rangle$  in Ch. VI for comparison to the observed  $\nu_2$  band line strengths. The dependence of  $\langle R_i | \varphi_{Zb} | R_f \rangle$  on the vibrationally averaged centrifugal distortion in each state is obtained by using one of Watson's high order reduced Hamiltonians to generate  $|R_i\rangle$  and  $|R_f\rangle$ . In the usual rigid rotor approximation,  $|R_i\rangle$  and  $|R_f\rangle$  are generated from the rigid rotor Hamiltonian given in equation II-6, using the same rotational constants for both the lower and upper states. The direction cosine matrix elements in the  $|JKM\rangle$  representation are given in many places<sup>(19,23)</sup> and are used to evaluate  $\langle R_i | \varphi_{Zb} | R_f \rangle$  since the asymmetric top rotational eigenfunctions are calculated in terms of  $|JKM\rangle$  basis functions.

In the rigid rotor approximation the total band intensity of the vibration-rotation band is determined by the  $\langle V_i | \mu_b | V_f \rangle$  matrix element. If the dipole moment is expanded about the equilibrium value as a Taylor series in the normal coordinates  $Q_i$ , we can approximate  $\mu_b$  by



$$\mu_b = \mu_b^0 + \sum_{i=1}^3 \left( \frac{\partial \mu_b}{\partial Q_i} \right)_{Q_i=0} Q_i + \dots, \quad (\text{II-39})$$

where  $\mu_b^0$  is the permanent dipole moment of  $\text{H}_2\text{S}$ . For the  $\nu_2$  band the vibration quantum number  $n_2$  given in equation II-5 changes 0 to 1. Only  $Q_2$  is non-zero for this vibration, giving

$$\langle V_i | \mu_b | V_f \rangle = \frac{\partial \mu_b}{\partial Q_2} \langle V_i | Q_2 | V_f \rangle, \quad (\text{II-40})$$

since  $\langle V_i | \mu_b^0 | V_f \rangle = 0$  for a rigid rotor.

The selection rules for changes in  $K_a$  and  $K_c$  for the  $\nu_2$  vibration can be determined using Table II-2. For the direction cosine matrix element to be non-zero, the product of the characters of the representations of the initial and final rotational wave functions and of the dipole moment change must be +1 for all of the group operators. For the  $\nu_2$  vibration, the change in the dipole moment belongs to the type  $B_b$  symmetry species, so that the selection rules for  $K_a$  and  $K_c$  are

$$ee \leftrightarrow oo, \quad eo \leftrightarrow oe.$$

This constrains the changes in  $K_a$  and  $K_c$  to be  $\pm 1, \pm 3, \pm 5, \dots$ . Generally transitions with changes of  $\pm 1$  in  $K_a$  and  $K_c$  are the strongest. The dipole selection rule  $\Delta J = 0, \pm 1$  also holds. The vibration-rotation transitions will be denoted by  $J'K'_aK'_c - JK_aK_c$  in this work, with the primed upper state values of  $J, K_a$  and  $K_c$  given first, followed by the lower state values of these numbers. It should be noted that  $g_i$ , the statistical weight factor, is three times larger for the  $eo$  and  $oe$  levels than for the  $oo$  and  $ee$  levels of the same  $J$  due to the nuclear spin statistics of the two identical protons in  $\text{H}_2\text{S}$ .

To take into account the effects of centrifugal distortion on the line strengths, Emerson and Eggers<sup>(1)</sup> used vibrational wavefunctions having coordinates which include centrifugal distortion displacements of the atoms from their rest equilibrium positions. They calculated the shift in the  $Q_1$  and  $Q_2$  normal coordinates from their rest equilibrium positions in both the upper and lower rotational states of each transition. This was done using classical expressions for the molecular distortion, which depend upon the rotational energy and the square of the angular momentum about the a, b, and c axes. The rotational

energies and angular momenta were determined by Emerson and Eggers using the rigid rotor Hamiltonian given in equation II-6. Using these new shifted coordinates in harmonic oscillator vibrational wavefunctions, they evaluated  $\langle V_i | \mu_b | V_f \rangle$  and obtained a first order correction to the rigid rotor line strengths,

$$S = S_{\text{rigid}}(1 + \gamma \delta \mu_b^0 / (\partial \mu_b / \partial Q_2))^2. \quad (\text{II-41})$$

where

$$\delta = \Delta Q_2^f - \Delta Q_2^i$$

is the difference between the centrifugal distortion of the normal coordinate  $Q_2$  in the final state and the initial state, and  $\gamma$  is a factor that depends upon the  $\nu_2$  vibrational frequency.

By choosing  $\mu_b^0$  and  $\partial \mu_b / \partial Q_2$  to have the same sign Emerson and Eggers were able to obtain qualitative agreement between the observed spectrum and a spectrum calculated using their strength correction term, showing that centrifugal distortion was indeed responsible for the observed intensity anomalies in this band. Since  $\delta$  has the same magnitude but a different sign for the transition  $J'_{K'_a K'_c} \leftarrow J_{K_a K_c}$  compared to its reverse  $J_{K_a K_c} \leftarrow J'_{K'_a K'_c}$ , one branch of the band is enhanced while the corresponding branch on the other side of the band center loses intensity. The intensity perturbation is also dependent on the ratio  $\mu_b^0 / (\partial \mu_b / \partial Q_2)$ , which is very large for  $\text{H}_2\text{S}$  compared to other molecules because  $\partial \mu_b / \partial Q_2$  is so small. The small size of  $\partial \mu_b / \partial Q_2$  is illustrated by the fact that the  $\nu_2$  band of  $\text{H}_2\text{S}$  is roughly 130 times weaker than the  $\nu_2$  band of  $\text{H}_2\text{O}$ .

The magnitude of the line strength perturbation is denoted by the F factor, which is the ratio of the observed line strength to the calculated rigid rotor line strength. For the  $\text{H}_2\text{S}$  lines observed in this work, the F factors were experimentally found to vary from about 0.06 in the  $Q^{\text{PR}}$  branch to greater than 4 in the  $Q^{\text{RP}}$  branch. (The branches are designated using the convention  $\Delta J \Delta K_a \Delta K_c$ .) A discussion of the observed F factors can be found in Ch. VI.

Perturbations of  $\text{H}_2\text{O}$  line strengths by centrifugal distortion have also been observed and several theoretical formulations have been devised to take these effects into

account.<sup>(24-26)</sup> Although the F factors for H<sub>2</sub>O lines are much closer to unity than those for H<sub>2</sub>S for the same transitions, lines in the  $\nu_2$  band of H<sub>2</sub>O involving very high energy rotational states have been observed, with F factors ranging from 0.07 to 3. Generally, the above referenced theoretical strength calculations were able, by least squares adjustments of free parameters, to fit the observed line strengths in the  $\nu_2$  band of H<sub>2</sub>O to 10%–20%, which is approximately the accuracy of the H<sub>2</sub>O line strength measurements.

It is hoped that the H<sub>2</sub>S  $\nu_2$  band line strengths measured in this work will be useful for a stringent test of existing theories developed for H<sub>2</sub>O. The H<sub>2</sub>S line strengths should be ideal for this purpose due to the wide range of F factors observed and to the high accuracy of the line strength measurements made here.

## CHAPTER III

### DIODE LASER SPECTROMETER AND DATA ACQUISITION

#### III. A. Introduction

The tunable diode laser spectrometer, constructed as part of this work, was used to measure all of the line strengths and the majority of the line frequencies of H<sub>2</sub>S reported here. The use of semiconductor diode lasers allows almost Doppler limited spectra to be taken in continuous segments about 0.5 cm<sup>-1</sup> to 1 cm<sup>-1</sup> wide. Diode laser fabrication technology has been developed to the point where spectral studies extending over 100 cm<sup>-1</sup> are practical using a single diode laser, so that rather complete studies of even light asymmetric top absorption bands can be made with these lasers.

The laser spectrometer was constructed so to meet several experimental requirements. These include: monitoring the relative frequency tuning of the laser simultaneously with the gas absorption signal; having a relative frequency calibration capability close to the accuracy of the best frequency standards ( $\approx 0.0004$  cm<sup>-1</sup>); being able to produce sample pathlengths from several meters to greater than 50 meters in order to detect the rather weak and variable strength H<sub>2</sub>S absorption lines at low pressure; and recording the data in digital form because of its large volume and information content. In this chapter the laser spectrometer will be described as well as procedures used to obtain a spectrum with this instrument. Several examples of spectra will be shown and discussed to illustrate the capabilities of this technique and to show typical characteristics of the spectrum of H<sub>2</sub>S.

A number of the line frequencies in the R branch region of the  $\nu_2$  band of H<sub>2</sub>S were measured with a high resolution (0.04 cm<sup>-1</sup>) grating spectrometer at the National Bureau of Standards (NBS).<sup>(27)</sup> A short summary of the experimental work performed with this instrument will also be given.

### III. B. Experimental Apparatus

The Pb-salt ( $\text{Pb S}_{1-x} \text{Se}_x$ ,  $\text{Pb}_{1-x} \text{Sn}_x \text{Se}$ ) tunable diode lasers used in this work were fabricated by Laser Analytics Inc. Laser action in these semiconductors results from stimulated emission across the energy gap between the conduction and valence band. A population inversion is achieved by applying a forward bias current to the diode and thereby injecting charge carriers across the p-n junction. The recombination of these carriers provides the gain mechanism for laser action. The end faces of the laser crystal, made by cleaving along natural crystal planes, form the laser resonator. Pb-salt diode laser crystals are typically  $400\mu\text{m}$  long and have cross sections of  $200\mu\text{m}$  by  $200\mu\text{m}$ .  $\text{Pb S}_{1-x} \text{Se}_x$  lasers can be made to operate from about  $2500\text{cm}^{-1}$  to  $1200\text{cm}^{-1}$  and  $\text{Pb}_{1-x} \text{Sn}_x \text{Se}$  lasers from  $1200\text{cm}^{-1}$  to  $300\text{cm}^{-1}$  by controlling their chemical composition ( $x$ ) during fabrication.

The output frequency of any one diode laser can be tuned  $20\text{cm}^{-1}$  to  $200\text{cm}^{-1}$  by changing the laser temperature from 10K to greater than 60K. The laser can be fine-tuned by varying its bias current, which changes the amount of  $I^2R$  heating of the laser and its electrical contacts, and therefore the operating temperature. While the overall tuning of the laser comes from the variation of the band gap energy with temperature, the fine-tuning within one mode is dominated by cavity mode shifts due to the decrease in the index of refraction of the laser material with increasing temperature.

Most diode lasers oscillate in several simultaneous modes separated in frequency by the cavity mode spacing of several wavenumbers. A single mode will usually continuously tune  $0.5\text{cm}^{-1}$  to  $1\text{cm}^{-1}$ . Diode laser linewidths have been measured by a number of workers<sup>(28,33)</sup> and can vary from less than 1MHz to greater than 20MHz FWHH. The diode laser linewidth will be discussed in more detail in Ch. IV. Single mode power levels range from several tens of microwatts to greater than one milliwatt for diode lasers. A PbSSe laser was used for the  $\text{H}_2\text{S}$  R branch region measurements and a PbSnSe laser for the P branch region measurements. A second PbSSe laser was used for the HI study. Several reviews of Pb-salt tunable diode lasers can be consulted for details of their fabrication and operation.<sup>(34,35)</sup>

A layout of the diode laser spectrometer is given in Fig. III-1. The laser is kept in a Cryogenics Technology Inc. closed cycle gaseous helium refrigerator that has an ultimate temperature of about 10K. The laser is mounted on a cold finger with a large thermal inertia that is vibration isolated from the rest of the refrigerator. The heat sink temperature can be varied with a small heater that is feedback controlled using a silicon diode temperature sensor. The heat sink can be varied in temperature from about 10K to greater than 100K and can be held stable to less than 0.3 mK. The refrigerator and temperature control system are available commercially from Laser Analytics Inc.

The laser radiation is collected with a  $f/1$  KRS-5 lens. The beam is then focused onto the entrance slit of a 50 cm focal length grating monochromator to select a single laser mode. A 400Hz tuning fork chopper at the entrance slit modulates the beam for phase-sensitive AC detection. The peak resolution of the grating monochromator is about  $0.25 \text{ cm}^{-1}$  and the wavenumber accuracy is about  $0.5$  to  $1 \text{ cm}^{-1}$ .

The radiation emerging from the monochromator is collimated with a 5 cm diameter, 30 cm focal length off-axis parabola. This results in a maximum beam width of about 2.5 cm. The collimated beam is split approximately fifty-fifty with an uncoated piece of germanium, wedged slightly so not to produce interference fringes. One beam then passes through a 7.65 cm long solid germanium etalon for relative frequency calibration and is focused onto a 1 mm square HgCdTe liquid nitrogen cooled detector with a 5 cm diameter, 15 cm focal length off-axis parabola. The second beam traverses a 1 meter base path multiple pass absorption cell (White cell<sup>(36)</sup>) and is focused onto a second 1 mm square HgCdTe detector with a 15 cm focal length lens. The two lenses marked  $L_2$  and  $L_3$  in Fig. III-1, as well as the White cell windows, are made of  $\text{BaF}_2$ . Lens  $L_2$  has a 27 cm focal length and focuses the collimated beam to a point coincident with the front surface of mirror  $M_1$ .

The optical design of a White cell has been discussed in many references<sup>(36)</sup> and will not be repeated here in detail. Spherical mirrors  $M_1$  (10 X 6 cm),  $M_2$  (9 X 7 cm), and  $M_3$  (9 X 7 cm) all have a 100 cm radius of curvature.  $M_1$  is separated from  $M_2$  and  $M_3$  by their common radius of curvature so that the beam is always focused when it hits  $M_1$ , irrespective of the

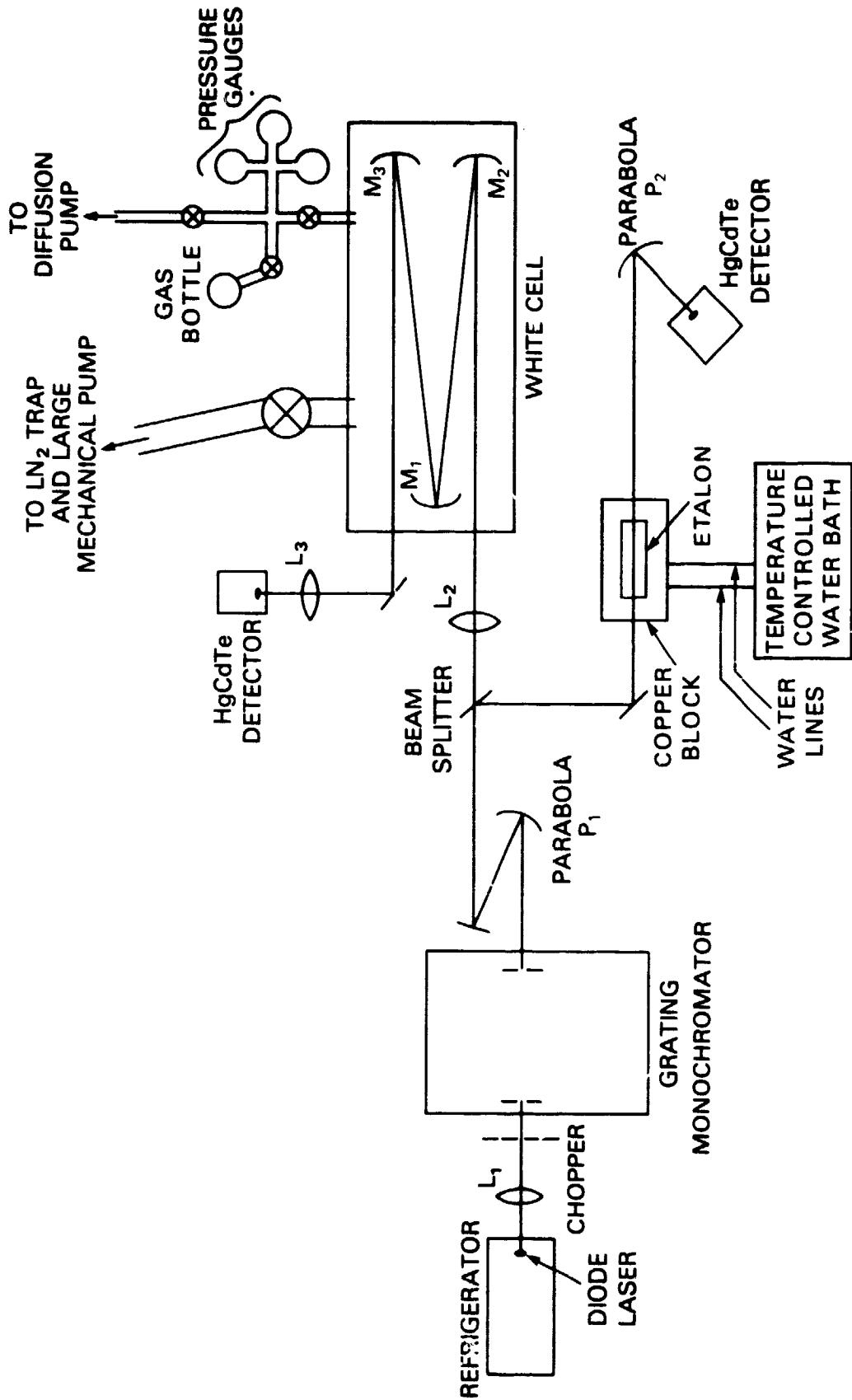


Figure III-1. Diode Laser Spectrometer

number of passes, and no radiation is lost due to vignetting. The top half of  $M_1$  is notched in the usual manner for passage of the entrance and exit beams. By adjusting  $M_2$  about a vertical axis, the beam can be made to traverse the cell from 4 to approximately 60 times in multiples of 4 passes, the only power loss coming from mirror reflection losses or from absorption by the gas in the cell. All three mirrors are gold coated for high reflectivity throughout the infrared. The White cell housing is a 9 inch ID glass pipe. Aluminum end caps sealed to the pipe with "O" rings hold the three mirrors. A rotary vacuum feedthrough near mirror  $M_2$  allows adjustment of the number of passes while the cell is under vacuum. The White cell path-length is given by

$$L = 99.855 \cdot N + 28.840 \text{ cm} \quad (\text{III-1})$$

where  $N$  is the number of passes the radiation makes in the cell. This equation for the path-length was obtained from careful measurements of the cell dimensions and is accurate to about 0.3%. The cell temperature is monitored with a thermocouple attached to the cell wall.

The cell is evacuated with a 21 cfm mechanical pump via a liquid nitrogen trap. This pump can evacuate the cell to several millitorr in a few minutes. A pure gas sample is achieved by filling the cell once with  $H_2S$ , pumping the cell to several millitorr, and then refilling it a second time with  $H_2S$ . Three MKS Baratron capacitance pressure gauges with full scale ranges of 1000 torr, 10 torr, and 1 torr monitored the cell pressure. Over the operating range of each gauge the accuracy is stated to be 0.08% of the pressure reading, if the gauge is zeroed properly. To get an accurate zero setting the gauges can be valved off from the large White cell volume and pumped with a diffusion pump to obtain a high vacuum. Intercomparisons of the three gauges indicate that their accuracy is at least a factor of two worse than the stated 0.08% of reading figure. Care was taken to not allow the 1 torr gauge pressure to go above about 10 torr without it being re-zeroed again, a procedure that takes several hours. If this gauge is let up to atmospheric pressure its zero reading usually changes a significant amount. In any case, leaks in the White cell (or outgassing of cell components) suggests a maximum uncertainty of 1% for the  $H_2S$  gas pressure, well above the inherent uncertainty of the pressure gauges. The 1 torr full scale gauge, used for almost all the pressure measurements here, was calibrated



to a quoted accuracy of less than 0.08% by the manufacturer just before the start of this work.

The H<sub>2</sub>S gas was supplied by Scientific Gas Products and had a stated purity of 99.99%. Two lecture bottles of H<sub>2</sub>S were used in the course of the experiment. One H<sub>2</sub>S line strength was measured using samples of H<sub>2</sub>S gas from each lecture bottle. Both measurements gave the same line strength within the precision of the experiment.

The solid germanium etalon has a free spectral range of about 0.016 cm<sup>-1</sup> and provides relative frequency calibration. Unfortunately, the index of refraction of germanium is very sensitive to temperature, resulting in large shifts of the etalon fringe peaks as the room temperature fluctuates. M. El-Sherbiny et al.<sup>(37)</sup> reduced the magnitude of these shifts by placing their etalon in a copper cylinder whose temperature was stabilized by flowing water from a temperature controller through the cylinder walls. They achieved a stabilization of better than 0.008 K, for time periods up to one hour, which corresponds to a fringe drift of 0.0008 cm<sup>-1</sup>, since for a germanium etalon

$$\frac{d\nu_{\text{peak}}}{dT} \approx 1.05 \times 10^{-4} \nu \text{ (cm}^{-1}\text{/K)}. \quad (\text{III-2})$$

The dependence of  $\frac{d\nu_{\text{peak}}}{dT}$  on the thermal expansion of the etalon is negligible.

We have followed this approach by placing the etalon in a copper cylinder as shown in Fig. III-2, where the top half of the cylinder has been removed for viewing. Water from a Thermomix 1480 temperature controlled water bath is circulated at a rate of about 10 liters per minute through four channels drilled in the copper. The inner surface of the cylinder was hand lapped to achieve good thermal contact between the copper and the etalon. The water bath temperature was set at 303.25K, about 7K above room temperature and was kept constant to about  $\pm 0.004$  K. At 1200 cm<sup>-1</sup>  $\frac{d\nu_{\text{peak}}}{dT} \approx 0.12$  cm<sup>-1</sup>/K so the  $\pm 0.004$  K variation in temperature translates into  $\pm 0.0005$  cm<sup>-1</sup>. The copper cylinder is relatively massive, providing thermal inertia to help keep the frequency drift of the fringes below  $\pm 0.0005$  cm<sup>-1</sup> over the time scale of a diode laser scan (2 to 20 minutes). An extremely slow tuning, and therefore very stable, diode laser was available to test the etalon

ORIGINAL PAGE  
BLACK AND WHITE PHOTOGRAPH

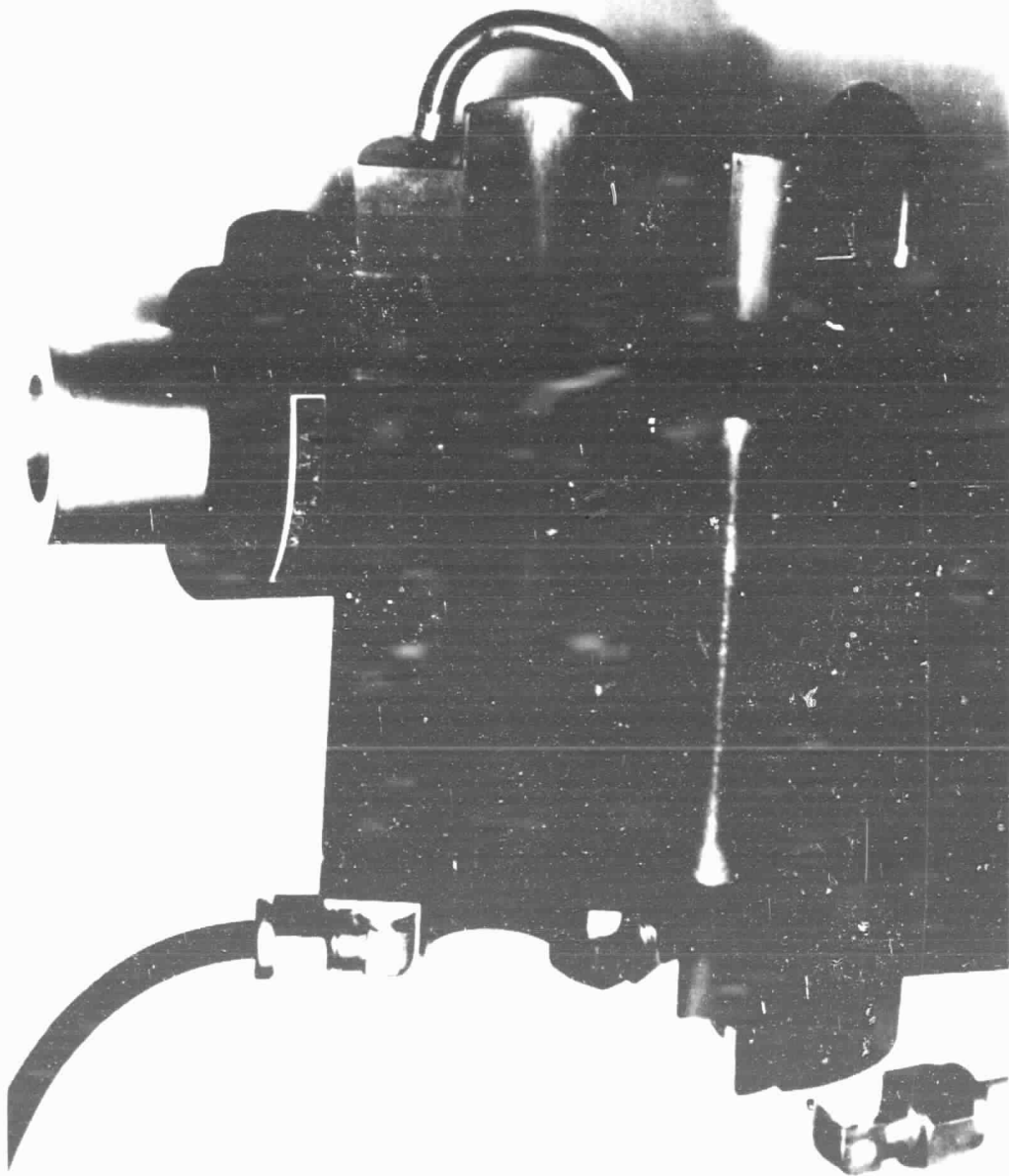


Figure III-2. Germanium Etalon and Temperature Stabilized Copper Holder

stability. Over a period of one half hour the frequency separation of a fringe peak and a gas absorption line next to it was measured six times. The average fringe peak drift between measurements was found to be only  $0.0001 \text{ cm}^{-1}$ , and the maximum drift over the whole one-half hour time period was  $0.0002 \text{ cm}^{-1}$ , an acceptable amount considering other error sources in the measurements.

A block diagram of the diode laser spectrometer electronics is shown in Fig. III-3. The laser is tuned by varying the injection current with a Laser Analytics Model LCM current controller. A 50Hz to 1kHz AC current ramp can be applied to the laser for real time display of the detector signals on an oscilloscope. Digitized data is recorded by exciting the laser with a slowly ramped DC current, mechanically chopping the radiation, and using lock-in amplifiers for AC phase sensitive detection. A switching unit allows the outputs of the lock-in amplifiers to be digitized sequentially at a combined rate of up to 70 samples per second. The readings from the 3-1/2 digit voltmeter are stored in a Hewlett Packard 9825 computer during the spectral scan. The digitized absorption spectrum and the etalon fringes can then be examined on a CRT display and stored on magnetic tape. Housekeeping information such as gas pressure, temperature, cell path-length, laser temperature, etc. are input by hand to the computer and are also stored on magnetic tape.

Each spectrum consisted of 4000 points for both the absorption spectrum and etalon fringes. Although this many points were not required for most of the shorter scans, keeping this number constant made operation of the data recording and analysis programs simple. Only the scan time desired (always 110 seconds or greater) and housekeeping information (if it changed) need be entered to the computer to start a scan. The outputs of the lock-in amplifiers could also be recorded on an analog X-Y-Y recorder when optimizing the experiment parameters before digitization.

### III. C. Operation of the Diode Laser Spectrometer and Sample Spectra

The laser spectrometer optics were aligned with a He-Ne laser and a white light source. The etalon was purposely mis-aligned to prevent back reflections of the laser radiation off

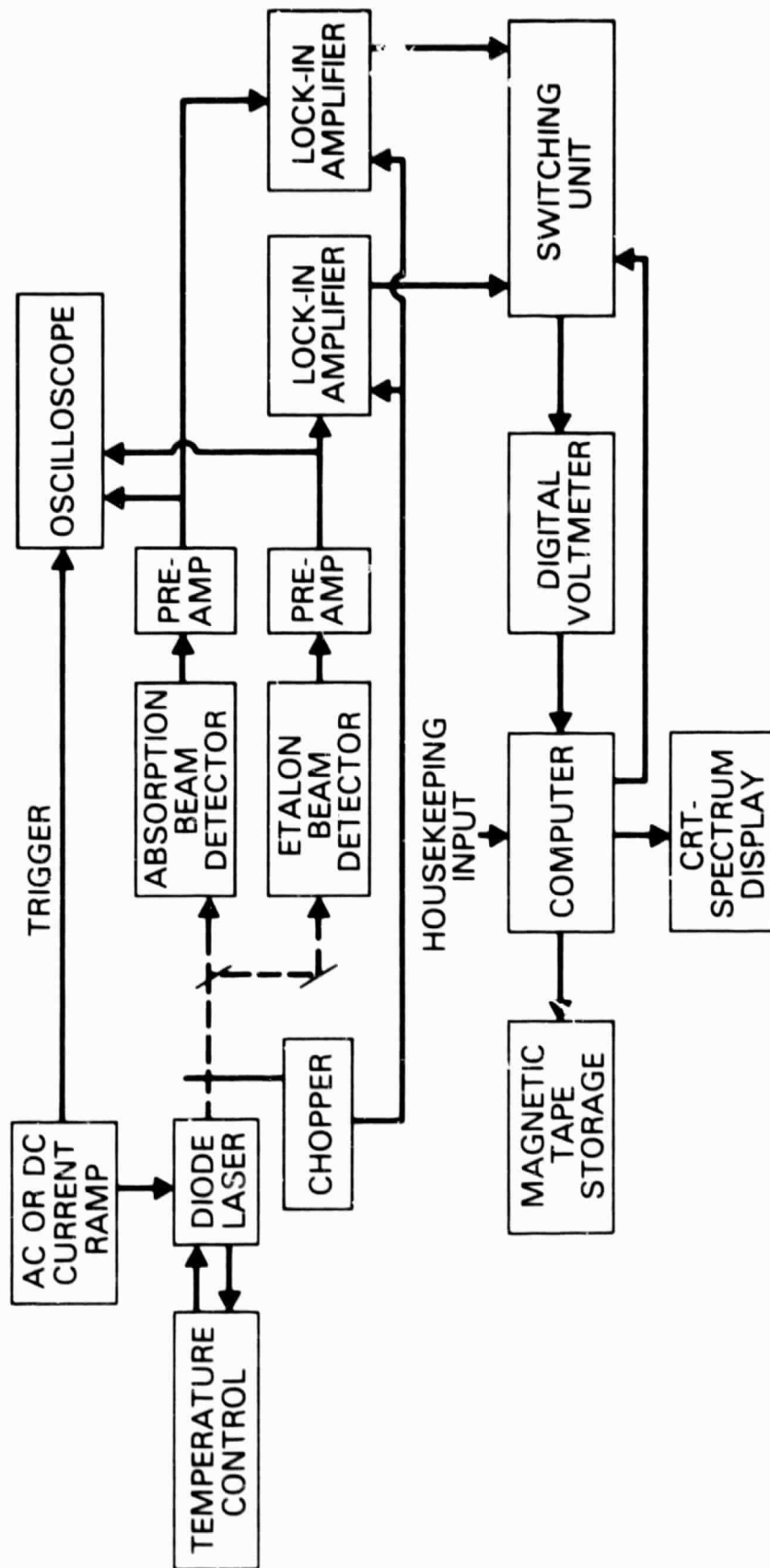


Figure III-3. Diode Laser Spectrometer Electronics

the etalon from re-entering the exit slit of the grating monochromator and feeding back to the laser. Both detector dewars were also tilted slightly so reflections of the laser radiation from the detectors could also not travel back to the diode laser. Without these mis-alignments composite optical cavities are formed that can set up laser modes that may broaden the apparent linewidth of the laser and increase the noise level.<sup>(29)</sup>

Final alignment of the laser spectrometer is performed by observing the detector signals from the diode laser radiation on a dual trace oscilloscope. By reducing the grating monochromator slitwidths and adjusting lens  $L_1$ , the image from a single laser mode is focused at the center of the exit slit. The entrance slit is then opened very wide to prevent reflections off the slit jaws from returning to the laser. The flat mirror before the etalon and the parabola  $P_2$  are adjusted to obtain etalon fringes with the highest finesse possible. Care was taken so that these adjustments did not allow back reflections from the etalon to re-enter the grating monochromator or tilt the etalon too much relative to the collimated beam. The finesse of the etalon fringes was also improved by masking off about 1/3 of the 1 inch diameter etalon. This improvement could be a consequence of poor optical quality of part of the etalon or may be from the effects of unwanted reflected radiation in the optical system. Also, a 3/4 inch diameter iris diaphragm placed just before lens  $L_2$  increased the absorption beam amplitude stability and prevented a slight amount of radiation reflected from the etalon beam from reaching the absorption beam detector. This iris diaphragm decreased the absorption beam signal very little.

The previous alignment procedures did not need to be repeated very often. Each new laser mode could usually be aligned by adjusting lens  $L_1$ , the grating angle, lens  $L_3$ , the White cell mirror  $M_2$ , and the parabola  $P_2$ . With care, amplitude jitter of the laser signal caused by the refrigerator vibrations could be kept below 0.1%. Before recording the spectrum the grating was scanned to be sure that the other laser modes were sufficiently far away in frequency from the mode being used. The ability to observe the absorption signal and the etalon fringes together in real time during the alignment process was invaluable. Very often the

gas absorption spectrum would appear to be of high quality while the etalon fringes would indicate a mode hop or frequency instability.

After these adjustments were made, the chopper was turned on and the laser slowly ramped with a DC current for detection with the lock-in amplifiers. A time constant of 0.1 second on the outputs of the lock-in amplifiers was always used. To be certain that the absorption lines exhibited no distortion, the laser scan rate was set so that the full width at half height of a line was scanned in a time period approximately equal to twenty time constants (2 seconds). For the strength measurements the gas in the White cell was allowed to come to equilibrium for a period of at least 15 minutes after filling. Whenever possible the gas pressure was kept below 0.3 torr and the pathlength chosen to give a peak absorption of 50% to 70%. The optimum peak absorption for determining line strengths from the peak absorption coefficient, as was done here, is 63%.<sup>(38)</sup> Slit widths equivalent to about  $0.4\text{ cm}^{-1}$  were used to separate the laser modes as completely as possible. Usually 3 digitized scans each of an absorption line at 3 different pathlengths were made. A shutter was placed in the laser beam for a short period during each scan to determine the 100% absorption level. Also, in most cases a scan of each mode was made with at least one absorption line saturated (i.e. absorbing 100% of the incident radiation at line center) to test for mode purity. To check for non-linearities, etc. in the apparatus a set of scans was taken with a constant pressure and 13 different pathlengths. Another set of scans with a constant pathlength and 10 different gas pressures was also recorded for the same reason. The line strengths obtained from these scans using the methods described in Ch. IV showed no evidence of non-linearities in the intensity scale or in the pressure readings greater than the measurement precision of about 1%.

To measure the  $\text{H}_2\text{S}$  line frequencies, a calibration gas was mixed with the  $\text{H}_2\text{S}$  in the White cell. Calibration gases included  $\text{CO}_2$ ,  $\text{N}_2\text{O}$ , and  $\text{NH}_3$  (see Ch. IV for details on the calibration lines). Usually three, and sometimes up to seven, scans were made for each frequency measurement. For these scans the grating monochromator slits were opened much wider than in the line strength scans to allow the  $1\text{ cm}^{-1}$  wide modes to be recorded without large changes in laser power across the spectrum.

The general procedure in the search for good laser modes was to start with low laser temperatures and currents and then slowly increase both of these parameters to find new modes. This was done since laser failure is much more likely at high temperatures and currents. By systematically varying the laser temperature, current, and the grating angle all useable modes were found, so as to achieve as complete a spectral coverage of the H<sub>2</sub>S spectrum as possible. Also the laser (heat sink) temperature was kept as high as possible and the injection current as low as possible when working with a given mode. This usually resulted in more stable (but weaker) laser emission and also reduced the number of modes at other frequencies.

A number of diode laser spectra of H<sub>2</sub>S are shown in Figs. III-4 to III-18. Most of the spectra shown are calibration scans since they are longer than the strength scans and better illustrate the spectrum of H<sub>2</sub>S. Most of the strength scans include only a single line over a spectral region of five or six fringes. Lines not identified in these spectra are due to calibration gas absorption lines other than the calibration line itself.

Figs. III-4 through III-10 show spectra containing two or more calibration lines per mode. These spectra and others were used to test the accuracy of the relative frequency calibrations performed here, which are discussed in Ch. IV. High signal-to-noise ratios were obtained for most of the spectra, even at pathlengths as long as 48 meters as can be seen in Fig. III-4. The baseline variations seen in the spectra are due to laser power variations, the slit function of the grating monochromator, and other causes. It should be remembered that as the laser is scanned its image is translated in the focal plane of the monochromator, thereby producing baseline variations.

These figures show that many modes of the laser used for the P branch measurements were at least 1 cm<sup>-1</sup> long. The mode in Fig. III-10 is greater than 1.5 cm<sup>-1</sup> long. Fig. III-15 is a scan more than 2 cm<sup>-1</sup> long that is part of a 5 cm<sup>-1</sup> mode, the longest one for this particular laser. Unfortunately this mode contained very few H<sub>2</sub>S lines. The scan shown here was used to transfer a calibration from the H<sub>2</sub>S 6<sub>34</sub>-7<sub>25</sub> line to an isotopic H<sub>2</sub>S line. The 6<sub>34</sub>-7<sub>25</sub> line was calibrated with a N<sub>2</sub>O line in the lower frequency portion of this mode. The isotopic line was then used to calibrate the blended doublet 7<sub>07</sub>-8<sub>18</sub>, 7<sub>17</sub>-8<sub>08</sub> at 1101.060 cm<sup>-1</sup>

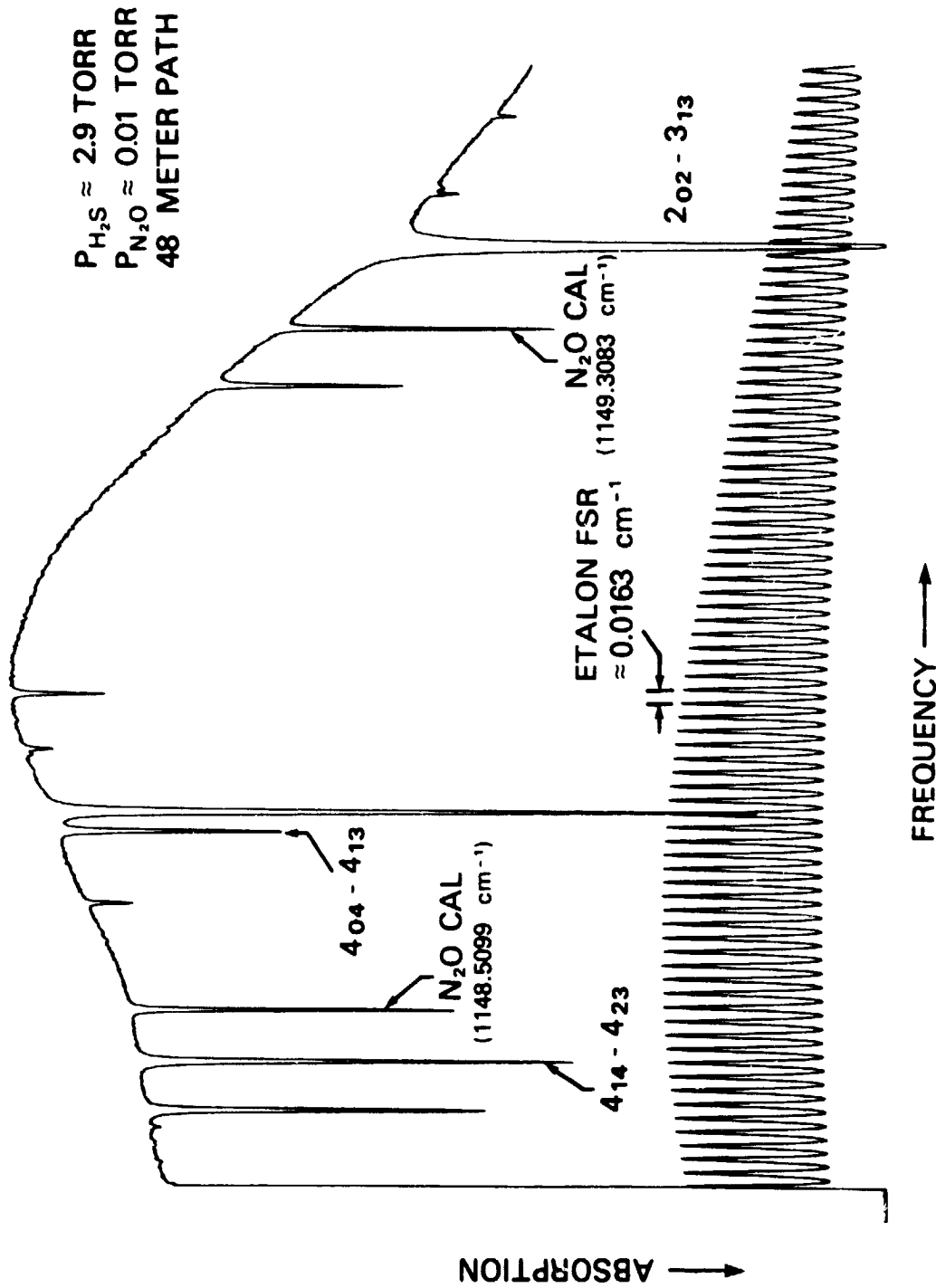


Figure III-4. Diode Laser Spectrum of H<sub>2</sub>S and N<sub>2</sub>O Near 1149.4 cm<sup>-1</sup>



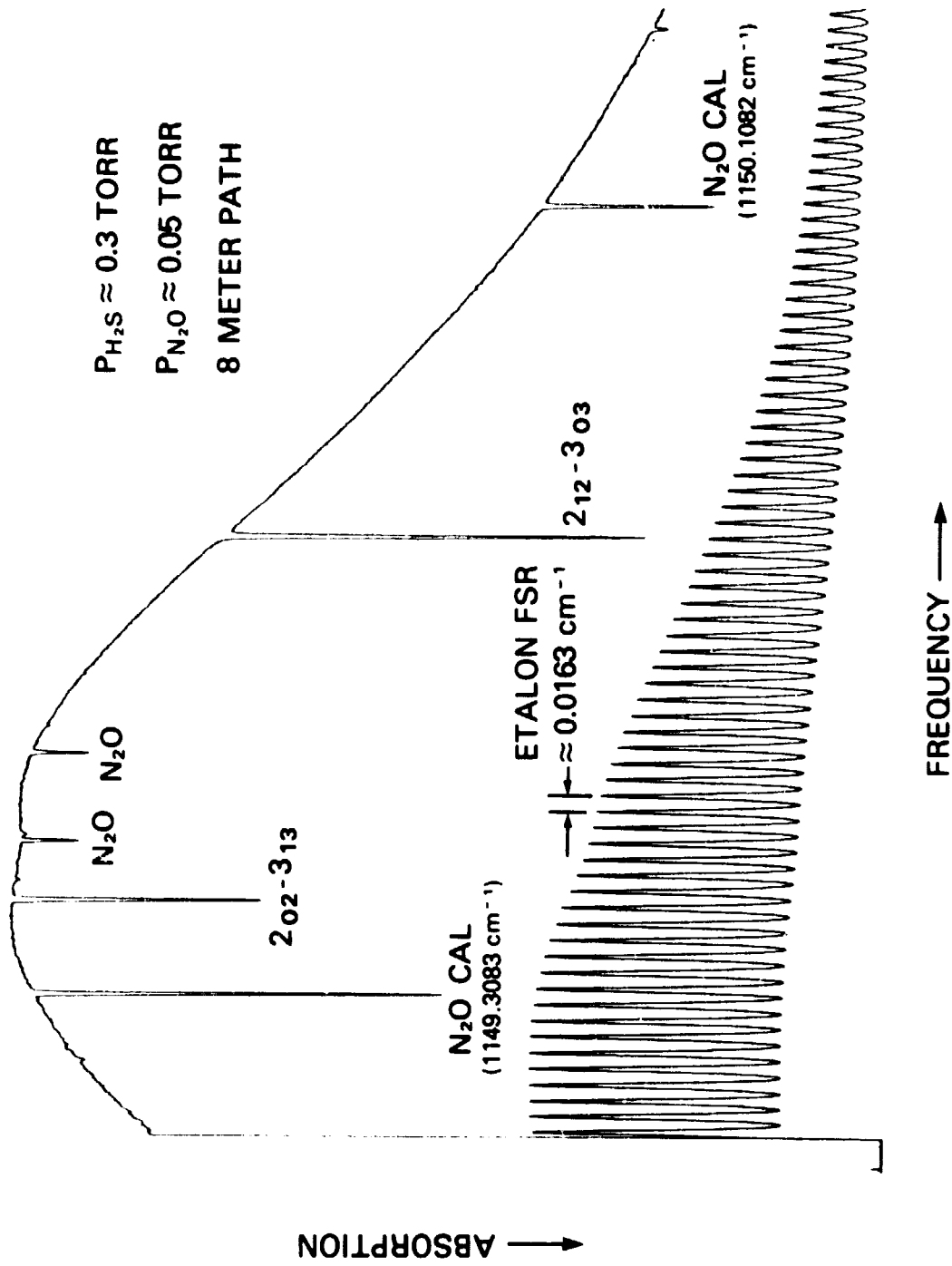


Figure III-5. Diode Laser Spectrum of H<sub>2</sub>S and N<sub>2</sub>O Near 1149.7 cm<sup>-1</sup>

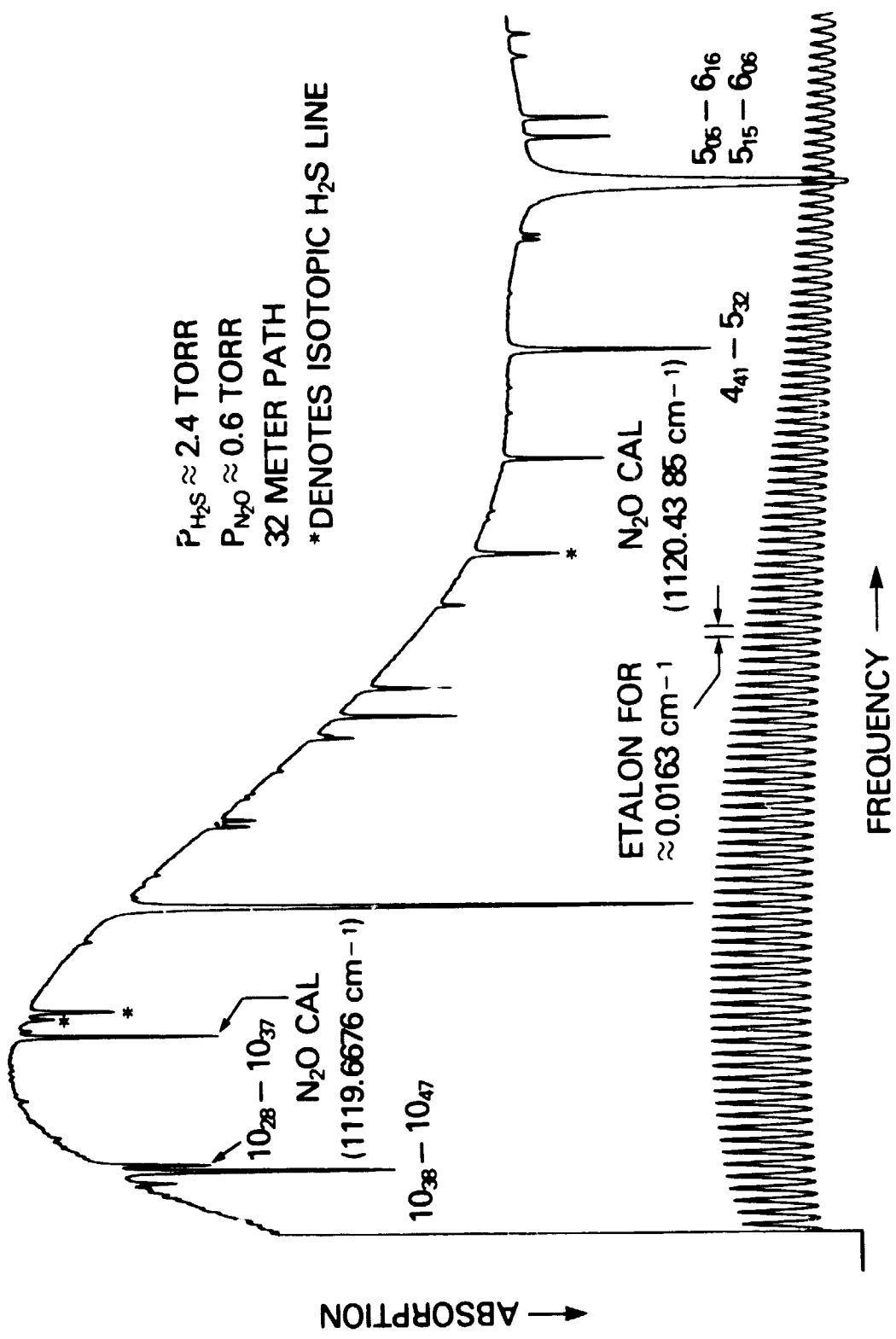


Figure III-6. Diode Laser Spectrum of  $\text{H}_2\text{S}$  and  $\text{N}_2\text{O}$  Near 1120  $\text{cm}^{-1}$

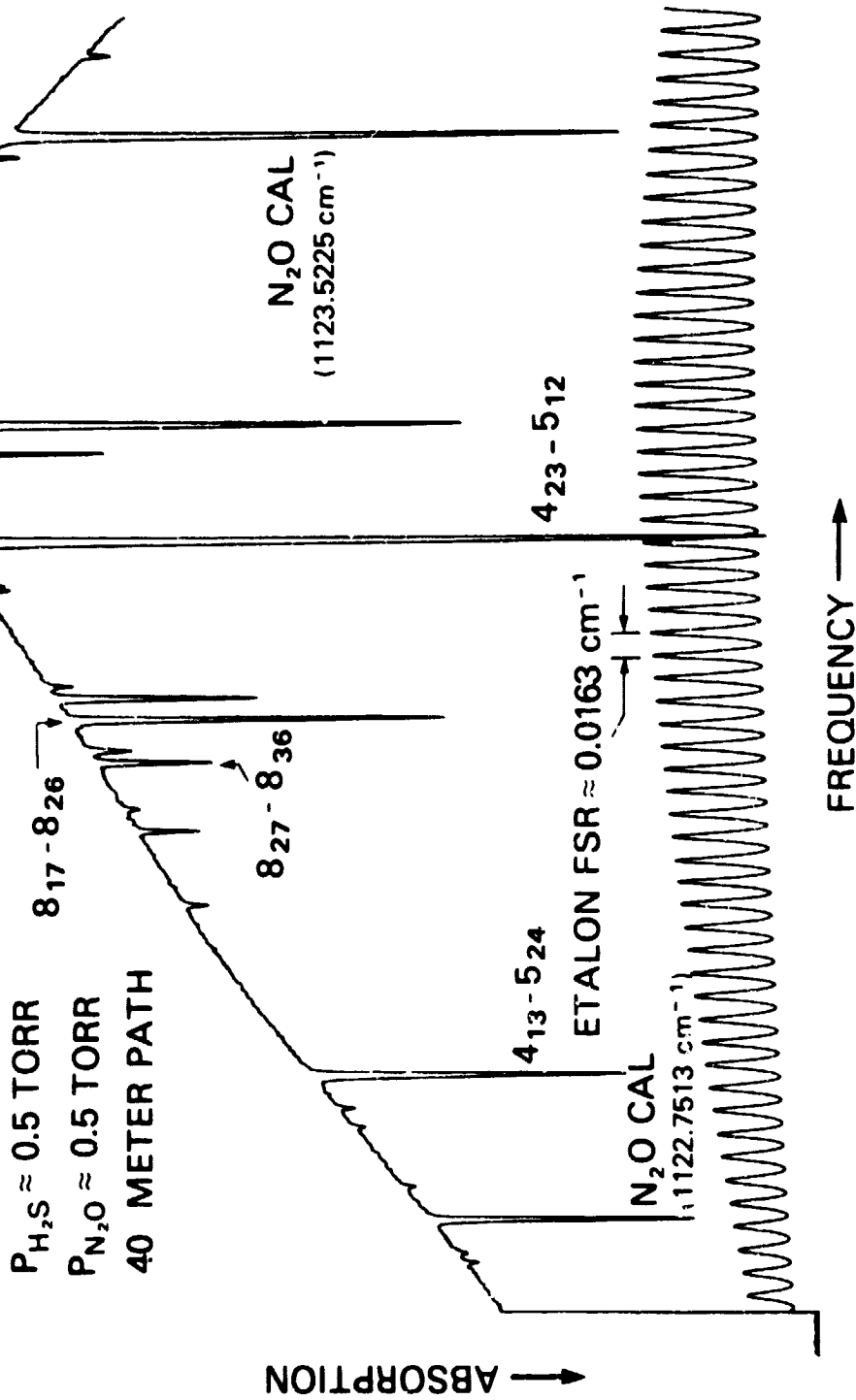


Figure III-7. Diode Laser Spectrum of H<sub>2</sub>S and N<sub>2</sub>O Near 1123 cm<sup>-1</sup>

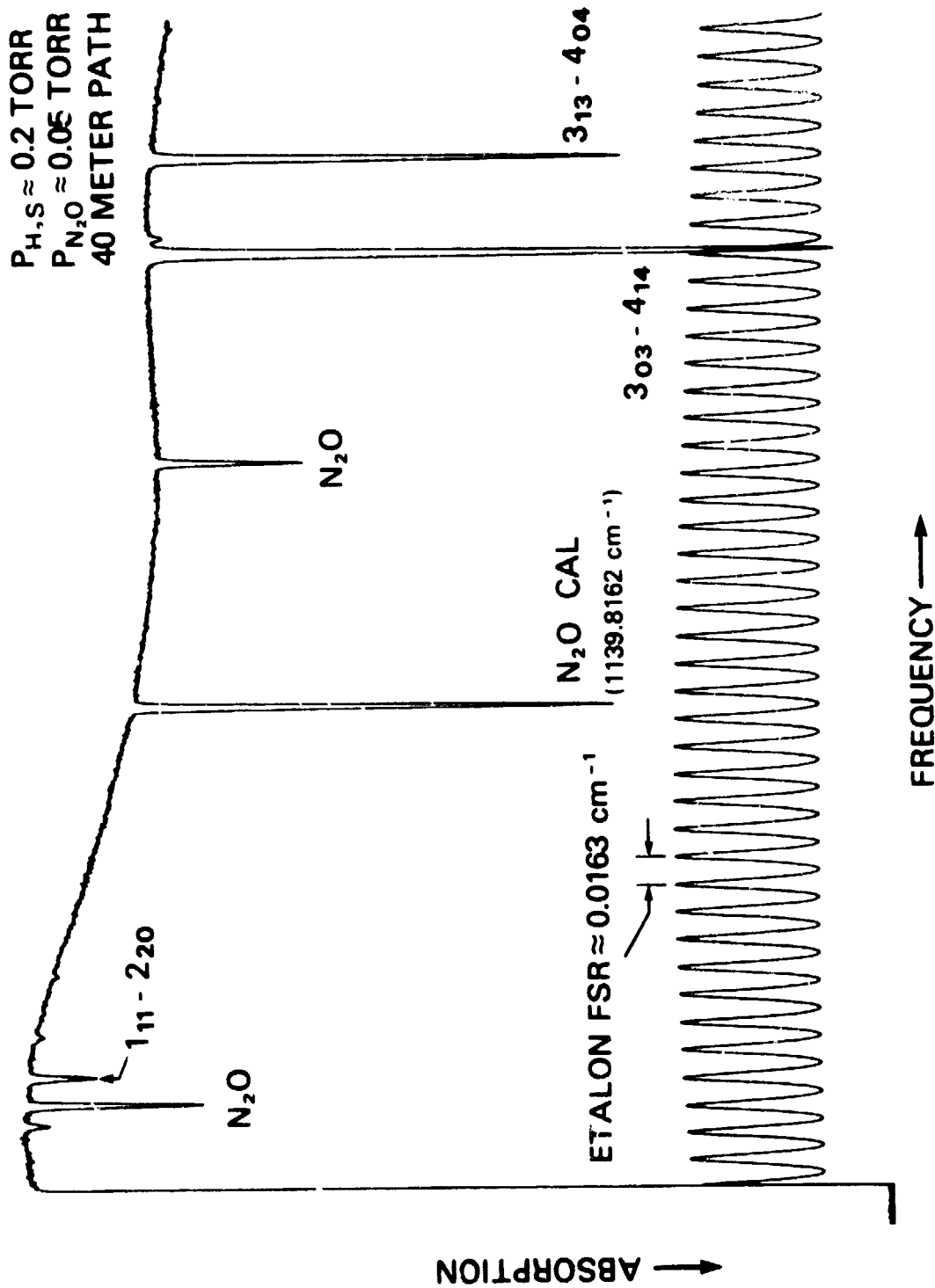


Figure III-8. Diode Laser Spectrum of  $\text{H}_2\text{S}$  and  $\text{N}_2\text{O}$  Near  $1140 \text{ cm}^{-1}$

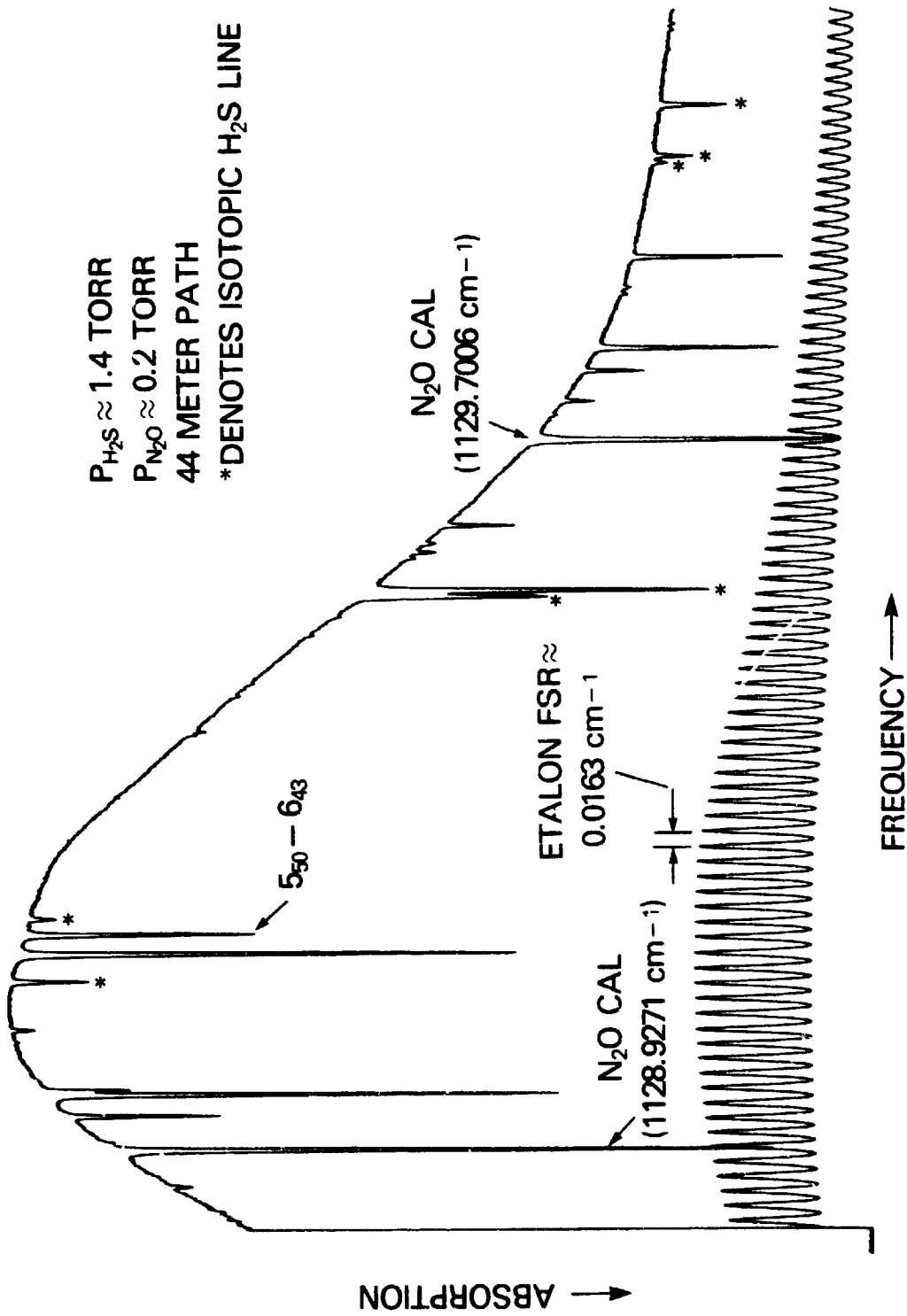


Figure III-9. Diode Laser Spectrum of H<sub>2</sub>S and N<sub>2</sub>O Near 1129 cm<sup>-1</sup>

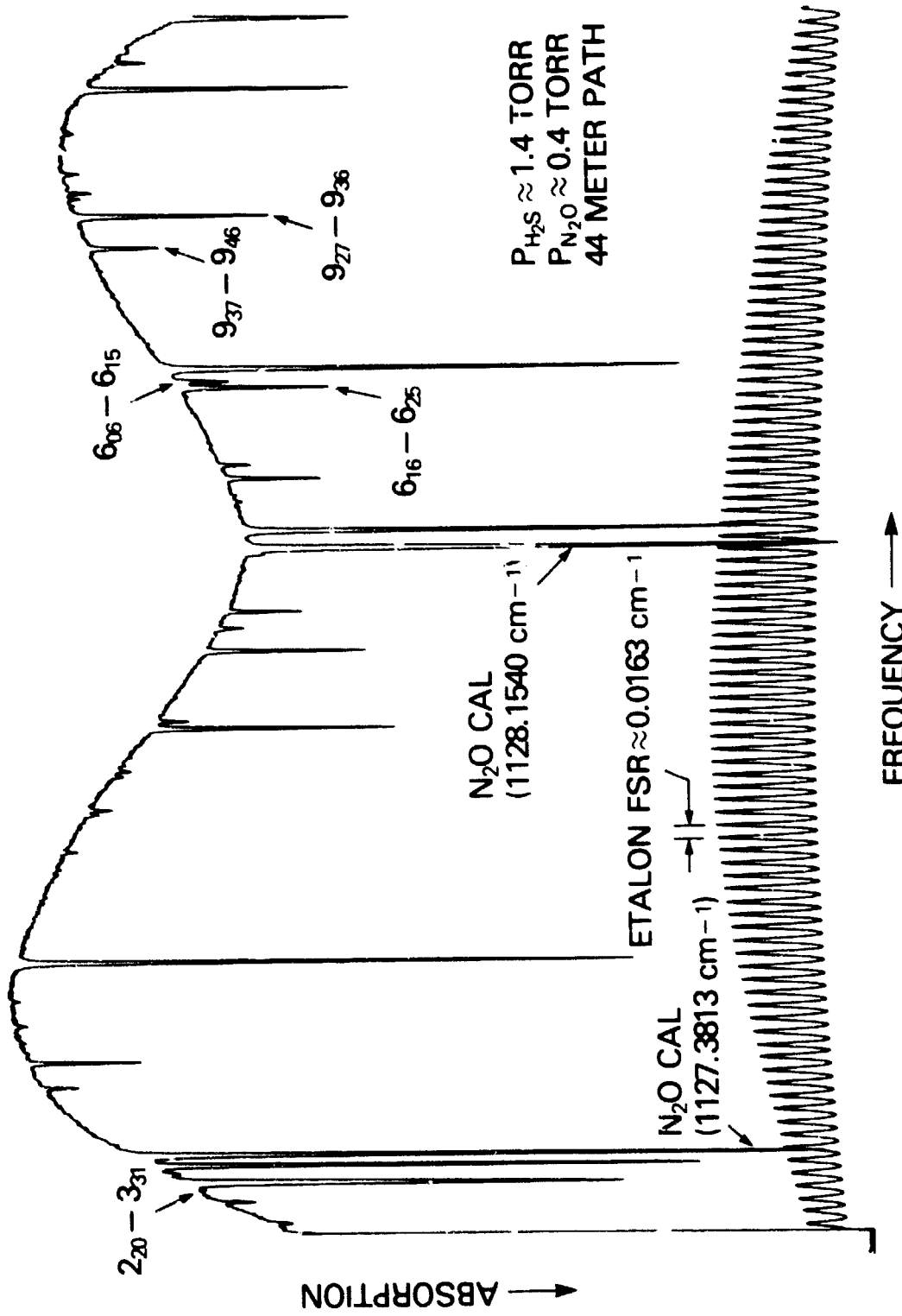


Figure III-10. Diode Laser Spectrum of H<sub>2</sub>S and N<sub>2</sub>O Near 1128 cm<sup>-1</sup>

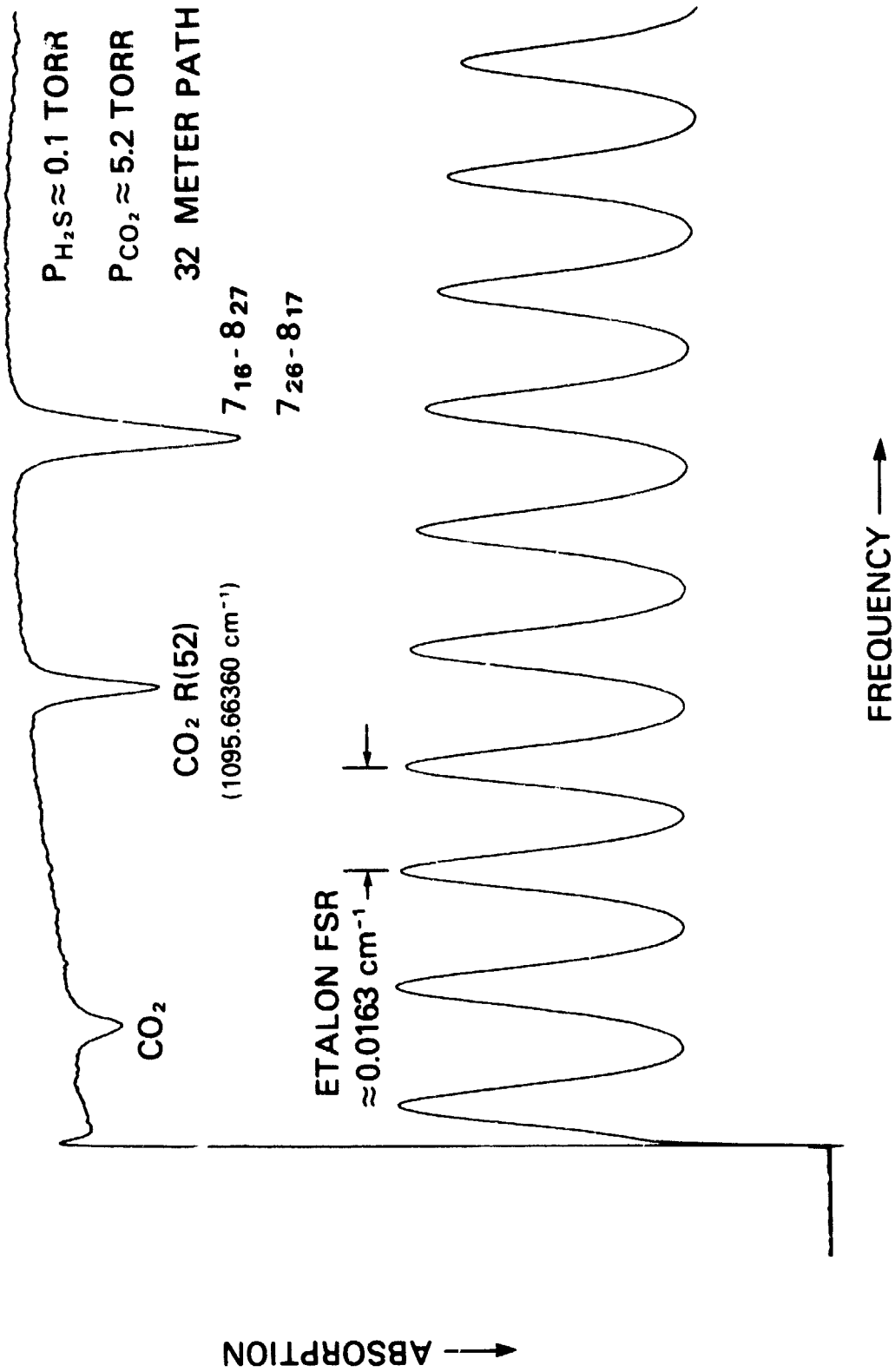


Figure III-11. Diode Laser Spectrum of H<sub>2</sub>S and CO<sub>2</sub> Near 1095.7 cm<sup>-1</sup>

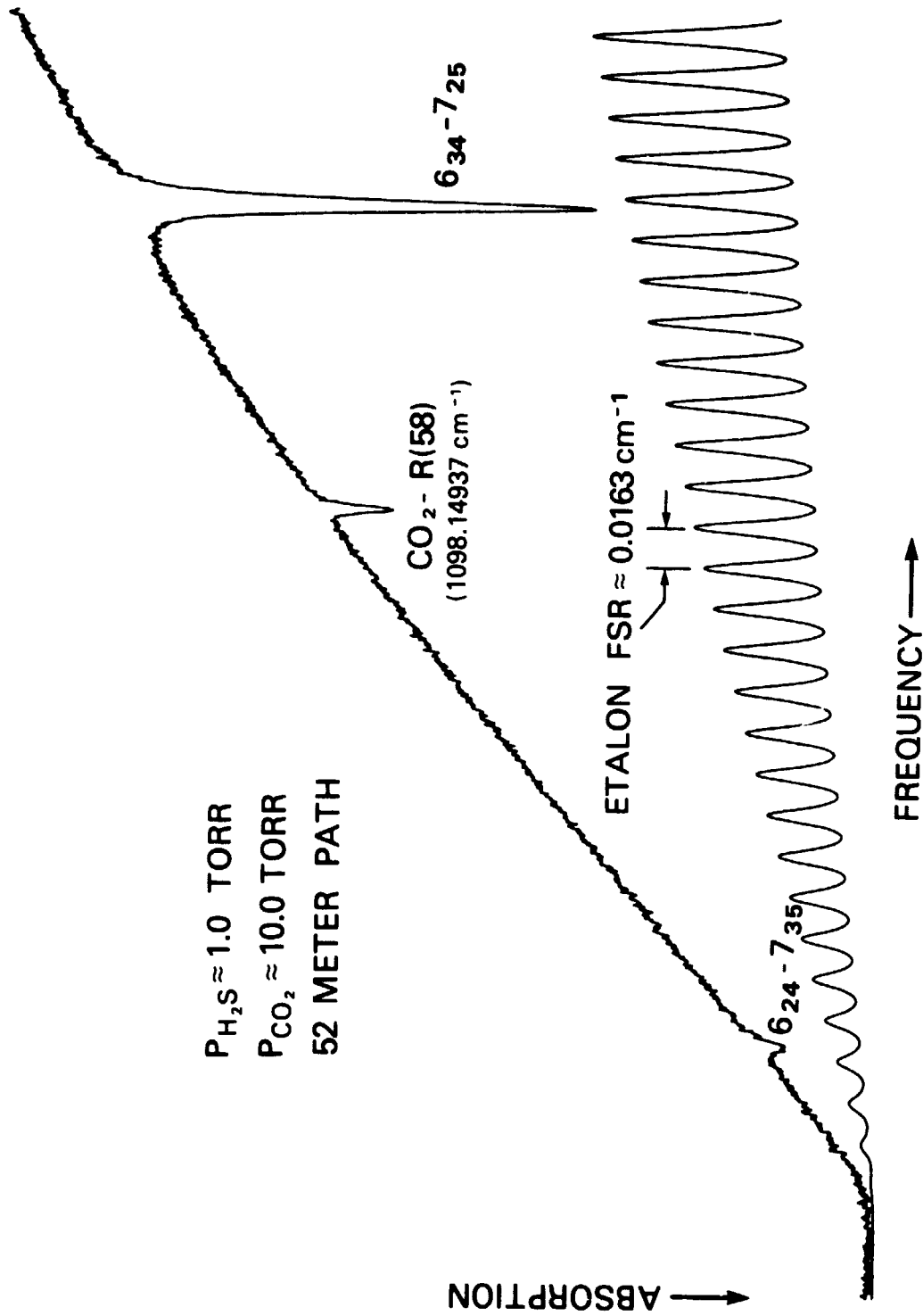


Figure III-12. Diode Laser Spectrum of H<sub>2</sub>S and CO<sub>2</sub> Near 1098 cm<sup>-1</sup>



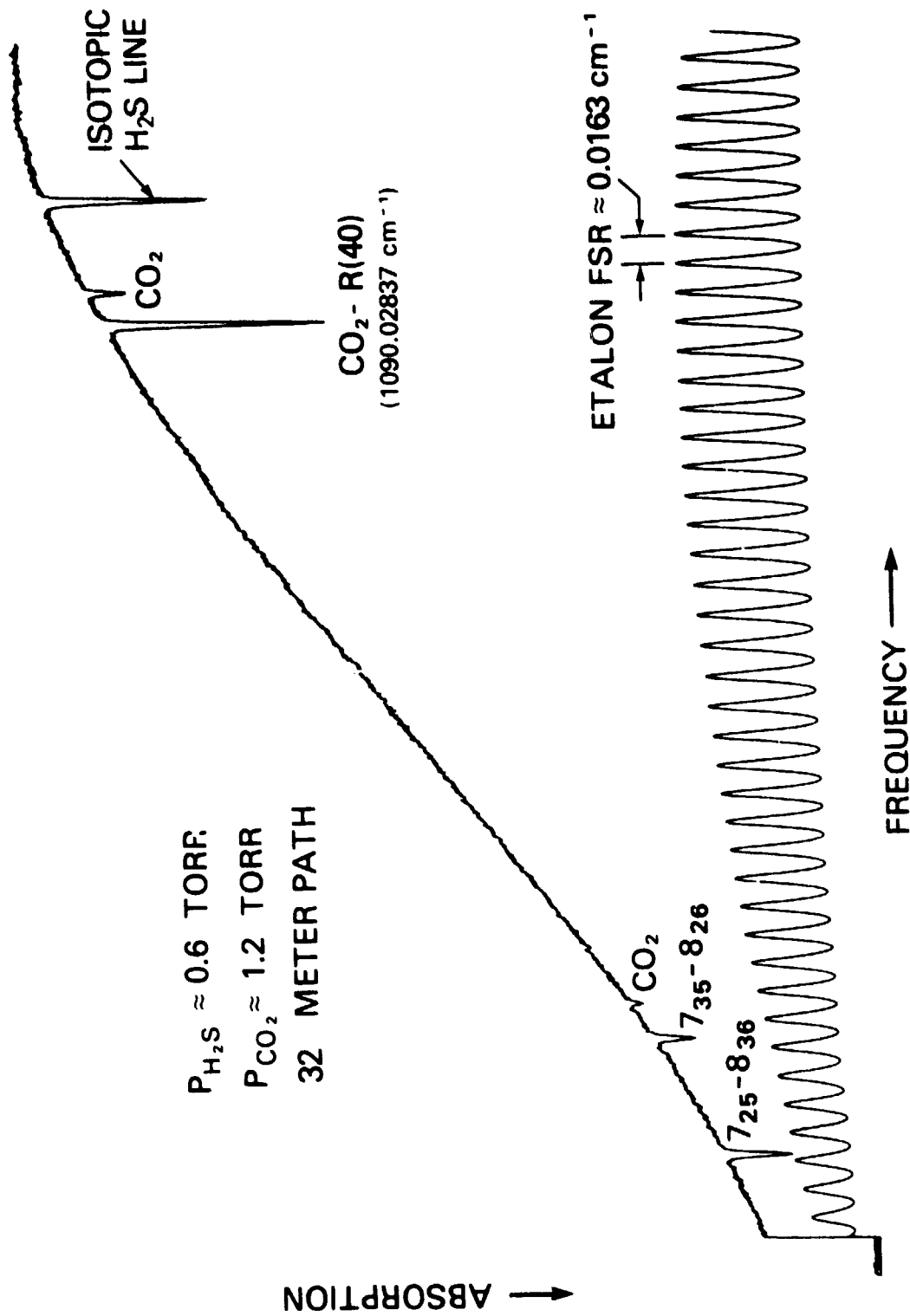


Figure III-13. Diode Laser Spectrum of  $\text{H}_2\text{S}$  and  $\text{CO}_2$  Near  $1090 \text{ cm}^{-1}$

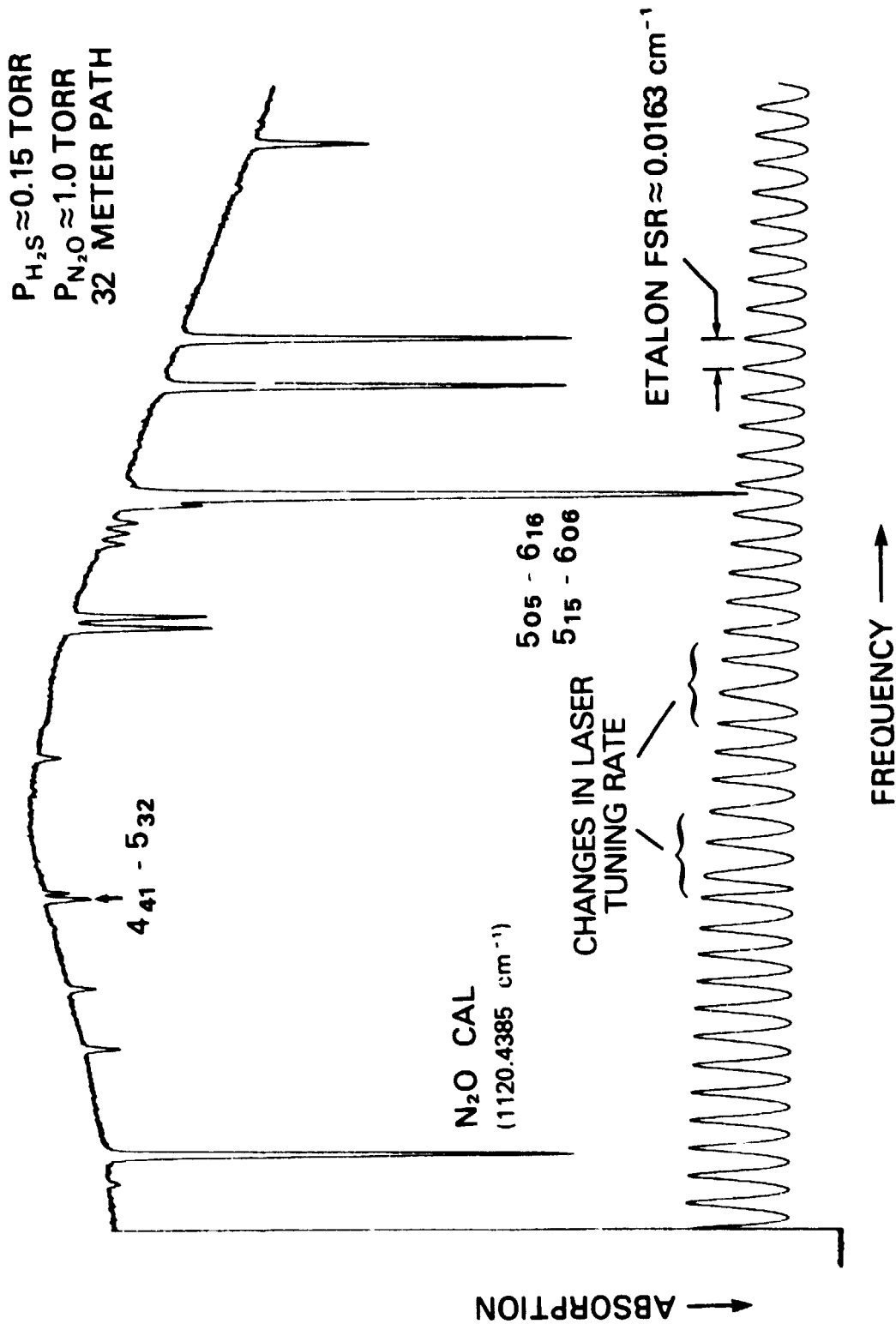


Figure III-14. Diode Laser Spectrum of  $\text{H}_2\text{S}$  and  $\text{N}_2\text{O}$  Near  $1120.5 \text{ cm}^{-1}$

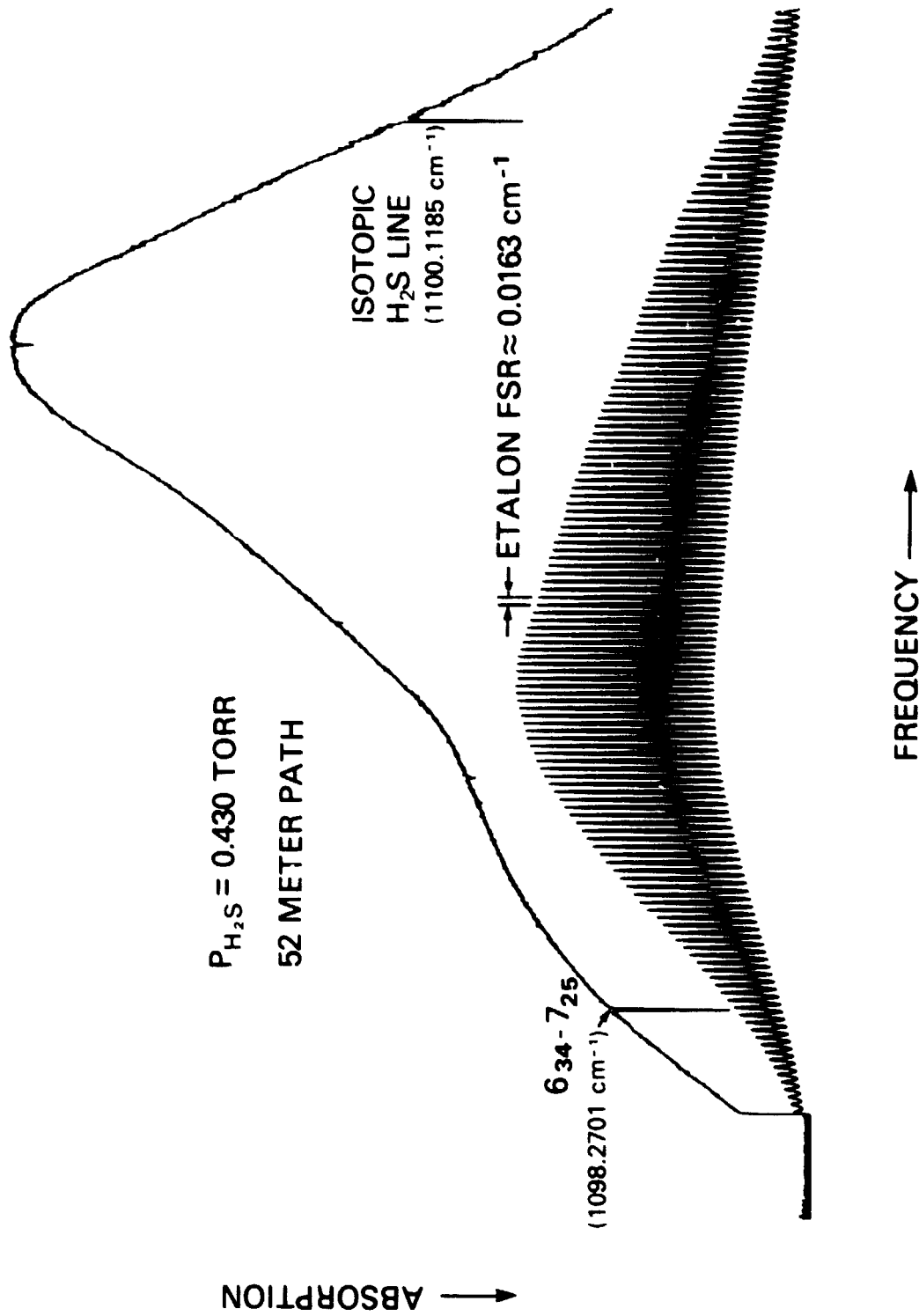


Figure III-15. Diode Laser Spectrum of  $\text{H}_2\text{S}$  Near  $1099 \text{ cm}^{-1}$

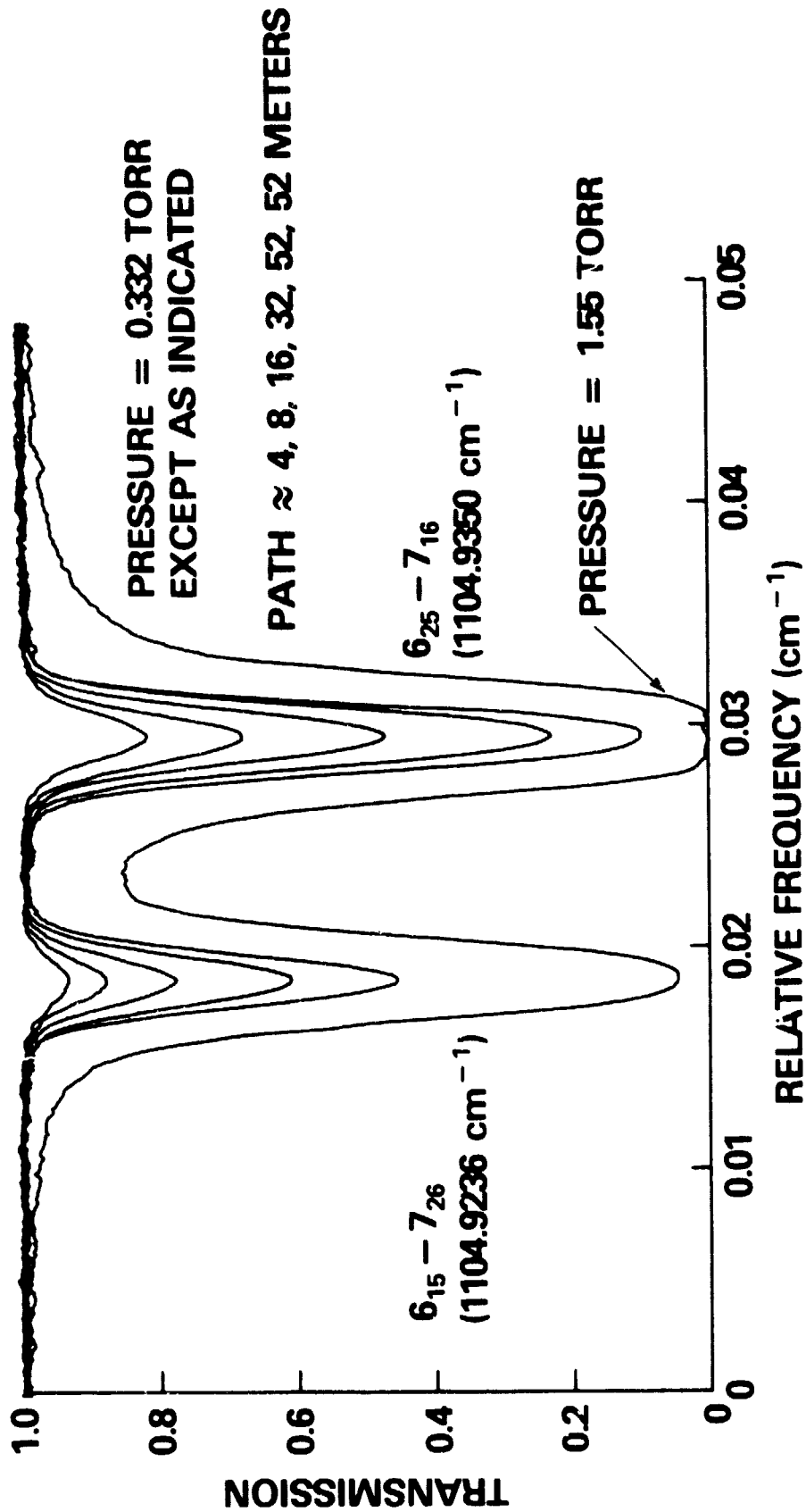


Figure III-16. Diode Laser Spectra of  $6_{15}-7_{26}$  and  $6_{25}-7_{16}$   $\text{H}_2\text{S}$  Transitions at Different Optical Depths

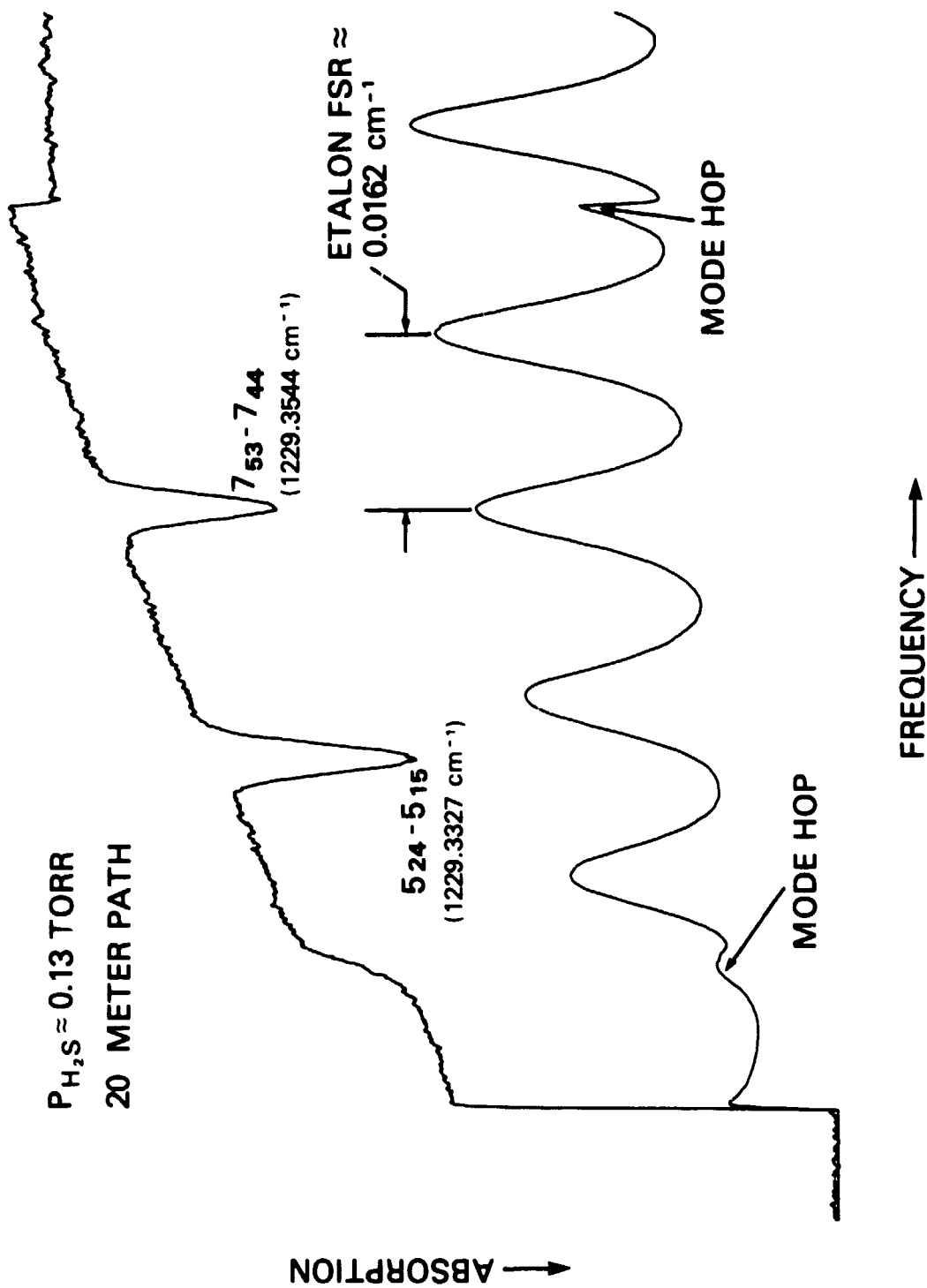


Figure III-17. Diode Laser Spectrum of  $\text{H}_2\text{S}$  Near  $1229.34 \text{ cm}^{-1}$

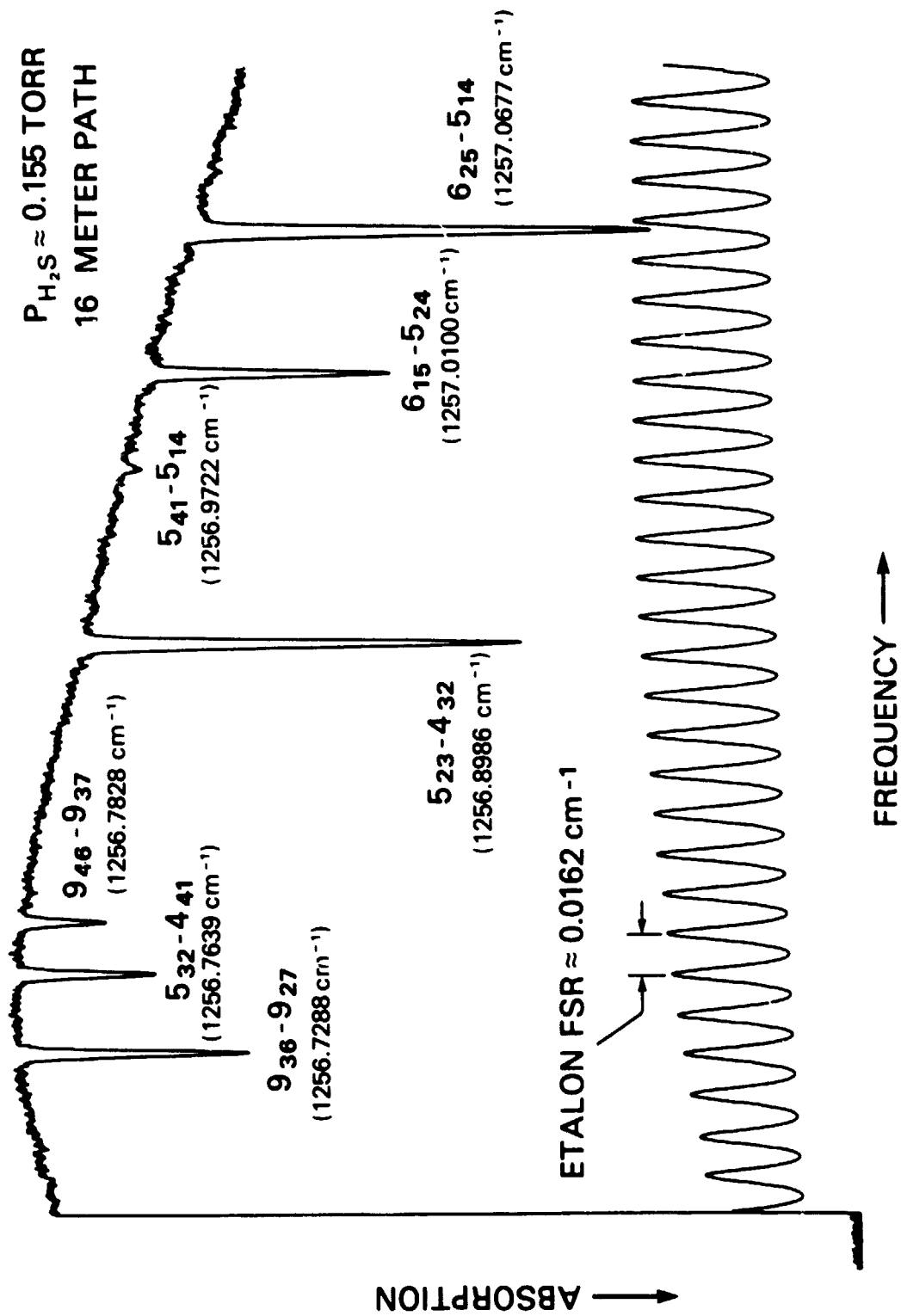


Figure III-18. Diode Laser Spectrum of  $\text{H}_2\text{S}$  Near  $1257 \text{ cm}^{-1}$

in the high frequency portion of this same mode. This was the only time a H<sub>2</sub>S line was calibrated in an indirect manner and over such a long frequency interval.

Whenever possible, CO<sub>2</sub> lines in the very accurately measured 9.6 μm band were used as calibration standards. Some of the spectra using CO<sub>2</sub> standards are shown in Figs. III-11 through III-13. Since the CO<sub>2</sub> lines used here are at the far end of the CO<sub>2</sub> R branch, relatively large optical depths of CO<sub>2</sub> were required. The weakest CO<sub>2</sub> line used was the R(58) transition for which a 52 meter path and 10 torr of CO<sub>2</sub> was required. Large optical depths of H<sub>2</sub>S were sometimes used to bring out weaker lines in the spectrum while saturating other lines, as can be seen in Figs. III-4 and III-6.

Another feature of the H<sub>2</sub>S spectrum is absorption lines due to isotopic H<sub>2</sub>S. The natural abundances of the sulphur 34 and sulphur 33 isotopes are 4.2% and 0.75% respectively. Isotopic lines are indicated in the spectra shown in Figs. III-6 and III-9.

Fig. III-14 is an example of a spectrum not used for any measurements due to instabilities in the frequency scale. These frequency non-uniformities are evident in the etalon fringes and illustrate the importance of recording the etalon fringes at the same time as the absorption signal. Subsequent scans of the same laser mode showed no evidence of frequency instabilities.

Some examples of spectra used for line strength measurements are given in Figs. III-16 through III-18. A number of scans at different pathlengths of the same transitions are superimposed in Fig. III-16. Also shown is a scan with the gas pressure and pathlength increased enough to saturate one transition for the determination of the 100% absorption level. The spectra shown here have been normalized to correct for a slightly sloping background. These spectra, as well as those in many of the other figures, show H<sub>2</sub>S doublets characterized by 3 to 1 intensity ratios which result from the effects of the nuclear spin statistics on the lower state rotational energy level populations.

Fig. III-18 is an example of the lowest signal to noise ratio obtained for any of the spectra recorded. This is also the most dense spectrum recorded for H<sub>2</sub>S. This spectrum has the only  $|\Delta K \pm 1| = 3$  line observed in the  $\nu_2$  band, the  $5_{41} - 5_{14}$  transition.

Fig. III-17 shows the shortest laser mode used in this work. This spectrum and those in Fig. II-16 are representative of the signal-to-noise ratio for the majority of the strength measurements. The appearance of two H<sub>2</sub>S lines in the mode shown in Fig. III-17 made the line assignments possible.

### III. D. Grating Spectrometer Measurements

About forty percent of the H<sub>2</sub>S line frequencies were measured with a high resolution grating spectrometer at the National Bureau of Standards. This work was performed before completing the construction of the diode laser spectrometer. Only a portion of the more strongly absorbing R and Q<sup>RP</sup> branches from 1180 cm<sup>-1</sup> to 1250 cm<sup>-1</sup> was recorded. High resolution measurements of the weaker P branch region could not be made since only a 60cm long absorption cell was available. With a continuous spectrum 70 cm<sup>-1</sup> long in the R branch the first quantum number assignments in the band could be easily made and an initial band fit obtained before the diode laser study. The molecular constants from this fit were used to generate a calculated spectrum of the  $\nu_2$  band of H<sub>2</sub>S. This spectrum enabled the line assignments in the diode laser spectra to be made quickly and easily. The grating spectra were also taken since the frequency measurements made with this instrument are more accurate than the calibration line frequencies available for use with the diode laser spectrometer from 1220 cm<sup>-1</sup> to 1235 cm<sup>-1</sup>.

The spectrometer, which has been described in detail elsewhere<sup>(27)</sup>, has an Ebert optical design with a 3.81 meter focal length and a 40.8 cm wide echelle diffraction grating. It was not practical to measure any line strengths with the grating spectrometer due to poor signal-to-noise, low resolution, and non-linear 100% transmission levels.

The H<sub>2</sub>S spectra were taken at a resolution of 0.04 cm<sup>-1</sup> and a signal-to-noise ratio of about 70 with a 1 second time constant on the output of the lock-in amplifier. The 60cm long gas cell contained about 20 torr of H<sub>2</sub>S. The spectrum from 1180 cm<sup>-1</sup> to 1250 cm<sup>-1</sup> was scanned and recorded on magnetic tape three times. It was calibrated by the standard method of inserting well known CO absorption lines appearing in other orders



of the grating into the H<sub>2</sub>S spectrum every 4 cm<sup>-1</sup>. A computer peak finder program found the line centers and computed a quadratic or cubic polynomial calibration curve from which the H<sub>2</sub>S line center frequencies were calculated. The reported frequencies are averages of the three trials. The calibration lines could generally be fit to better than ±0.001 cm<sup>-1</sup> and the overall error in the measured frequencies is believed to be about ±0.002 cm<sup>-1</sup>.

CHAPTER IV  
EXPERIMENTAL RESULTS - DETERMINATION OF THE H<sub>2</sub>S LINE  
FREQUENCIES AND STRENGTHS

IV. A. Introduction

The determination of the H<sub>2</sub>S frequencies and strengths from the diode laser spectra will be discussed in this chapter. This will include a brief description of the computer analysis of the raw digital data. Errors in the line center frequency measurements from using solid germanium etalons to determine the relative frequency scale will be analyzed and tests of the overall experimental accuracy presented. The method of measuring the line strengths from the line center absorption at low pressure and the errors associated with this method will be discussed in detail. These errors include the effects of laser lineshape and pressure broadening on the line center absorption. Corrections to the measured line strengths for either a Lorentzian or Gaussian laser lineshape will be presented.

A total of about 1200 spectra were recorded with the diode laser in the course of this work. A total of 126 line frequencies were measured, distributed as 32 P branch, 25 R branch, 14 Q<sup>PR</sup> branch, and 55 Q<sup>RP</sup> branch lines. Of these lines, 77 were measured with the diode laser spectrometer and 49 with the grating spectrometer. All 49 lines measured with the grating spectrometer were in the R and Q<sup>RP</sup> branches between 1081 cm<sup>-1</sup> and 1250 cm<sup>-1</sup>. A total of 94 line strengths were measured (all with the diode laser), distributed as 32 P branch, 16 R branch, 13 Q<sup>PR</sup> branch, and 33 Q<sup>RP</sup> branch lines. All of the lines measured here fell between 1081 cm<sup>-1</sup> and 1260 cm<sup>-1</sup>.

The H<sub>2</sub>S line assignments were made using a spectrum calculated with the molecular constants obtained from a fit of the grating spectrometer data. This spectrum, along with the known frequency setting of the diode laser mode selecting grating monochromator and with the H<sub>2</sub>S and calibration gas line patterns in the spectra allowed the assignments to be made with ease.

#### IV. B. Frequency Measurements and Error Analysis

The H<sub>2</sub>S line center frequencies were determined by measuring the frequency difference between a well known reference absorption line and the H<sub>2</sub>S line. The relative frequency scale was derived from the etalon fringe peaks using a calculated free spectral range for the etalon. A total of 66 lines was calibrated relative to N<sub>2</sub>O lines, 7 relative to CO<sub>2</sub> lines, and 4 relative to NH<sub>3</sub> lines. The N<sub>2</sub>O calibration standards<sup>(39)</sup> were either from the  $\nu_1$  band centered at 1284.9 cm<sup>-1</sup> or from the  $2\nu_2$  band centered at 1168.1 cm<sup>-1</sup>. The errors quoted for the N<sub>2</sub>O line frequencies range from  $\pm 0.0018$  cm<sup>-1</sup> to  $\pm 0.00098$  cm<sup>-1</sup> for the  $\nu_1$  band and from  $\pm 0.0018$  cm<sup>-1</sup> to  $\pm 0.00035$  cm<sup>-1</sup> for the  $2\nu_2$  band. The CO<sub>2</sub> calibration line frequencies<sup>(40)</sup> are known to better than 0.00001 cm<sup>-1</sup>, well within the precision of this experiment. The NH<sub>3</sub> lines have been measured with a high resolution grating spectrometer<sup>(41)</sup> to an accuracy of about  $\pm 0.005$  cm<sup>-1</sup>. The average uncertainty in the calibration line frequencies used here was  $\pm 0.0010$  cm<sup>-1</sup>.

The digitized absorption spectra and etalon fringes were analyzed with a computer program to obtain relative line center frequencies, line center absorptions, linewidths, and etalon fringe peak positions. A least squares fit of the 100% transmission region surrounding each absorption line to a cubic polynomial was used to determine the 100% transmission level across the line. The line center frequency, line center absorption, and linewidth were determined from least squares fits of portions of the line profile to a cubic polynomial. Cubic polynomials were chosen for the fits to the line profile rather than a single fit to a Doppler lineshape for reasons of computing speed (a desktop computer was used and over 1100 spectra were analyzed) and because of possible deviations of the true lineshape from the Doppler, especially at higher pressures. The etalon peaks were also determined from fitting the region around each peak to a cubic polynomial. Since most of the line strength spectra were only 0.1 cm<sup>-1</sup> to 0.2 cm<sup>-1</sup> long, the line profile fits usually included 30 to 60 points. For the longer frequency calibration scans the number of points per line fit ranged from 6 to 12.

The fringe peak positions were fit to cubic spline functions for interpolation between fringe peaks. In most cases the fringe separations were constant enough that linear interpolation between peaks would have sufficed. The H<sub>2</sub>S line frequencies and widths were then converted to wavenumber units using the free spectral range of the etalon and the calibration line frequency.

It is of utmost importance to use an accurate value for the etalon free spectral range. For example, a 0.5 cm<sup>-1</sup> separation between the calibration line and unknown line translates into about 30 etalon fringes. If we wish to measure this frequency difference to 0.0002 cm<sup>-1</sup>, the etalon free spectral range must be known to 6.7 × 10<sup>-6</sup> cm<sup>-1</sup> or 0.04%.

The free spectral range of an etalon is given to a high degree of accuracy by

$$\Delta\nu_{\text{FSR}} = \frac{1}{2t \left( n + \frac{dn}{d\lambda} \lambda \right)}, \quad (\text{IV-1})$$

where  $n$  is the index of refraction of germanium at the wavelength  $\lambda$  and  $t$  is the etalon thickness. To calculate  $\Delta\nu_{\text{FSR}}$  accurately very good values for  $n(\lambda)$  and  $t$  are required. A careful measurement of the etalon length gave  $t = 7.65048 \pm 0.00038$  cm, accurate enough so to not introduce large errors into the calculated free spectral range. Fortunately, the index of refraction of germanium has been measured at eleven wavelengths between 2.55 μm and 12.36 μm to an accuracy of 0.015%.<sup>(42)</sup> A cubic spline fit to this data was used to interpolate between the measured values of the index of refraction and to determine  $dn/d\lambda$ . The cubic spline coefficients for this fit are given in Table IV-1. Before calculating the free spectral range, the room temperature values for the index of refraction obtained using Table IV-1 were corrected to  $T = 303.3$  K, the temperature at which the etalon was stabilized.

There are several other errors associated with the use of etalons in relative frequency calibration. One of these, fringe pattern fluctuations from etalon temperature drifts, was shown in Chapter III to have a maximum value of  $\pm 0.0001$  cm<sup>-1</sup>. Another possible calibration error comes from angular misalignment of the etalon relative to the collimated

Table IV-1

## Spline Fit Coefficients for Index of Refraction of Germanium

(a) Wavelength, $\lambda_i$ ( $\mu\text{m}$ )	(b) Index, $n_i$	B	C	D
2.554	4.06230	$-2.6322 \times 10^{-2}$	$-3.3061 \times 10^{-1}$	1.0568
2.652	4.05754	$-6.0672 \times 10^{-2}$	$-1.9902 \times 10^{-2}$	1.0568
2.732	4.05310	$-4.3565 \times 10^{-2}$	$2.3374 \times 10^{-1}$	$-9.5556 \times 10^{-1}$
2.856	4.04947	$-2.9676 \times 10^{-2}$	$-1.2173 \times 10^{-1}$	$7.2885 \times 10^{-1}$
2.958	4.04595	$-3.1760 \times 10^{-2}$	$1.0130 \times 10^{-1}$	$-2.6202 \times 10^{-1}$
3.090	4.04292	$-1.8714 \times 10^{-2}$	$-2.4617 \times 10^{-3}$	$3.2369 \times 10^{-3}$
4.120	4.02457	$-1.3483 \times 10^{-2}$	$7.5404 \times 10^{-3}$	$-2.1275 \times 10^{-3}$
5.190	4.01617	$-4.6538 \times 10^{-3}$	$7.1115 \times 10^{-4}$	$-4.1458 \times 10^{-5}$
8.230	4.00743	$-1.4794 \times 10^{-3}$	$3.3305 \times 10^{-4}$	$-1.0377 \times 10^{-5}$
10.270	4.00571	$-2.5008 \times 10^{-4}$	$2.6955 \times 10^{-4}$	$-1.0377 \times 10^{-5}$
12.360	4.00627			

(a)  $\lambda_i$  and  $n_i$  are experimental values from ref. (28) for  $T = 297\text{K}$ .

(b)  $n(\lambda) = n_i + B(\lambda - \lambda_i) + C(\lambda - \lambda_i)^2 + D(\lambda - \lambda_i)^3$ ,  $\lambda_i < \lambda < \lambda_{i+1}$ .

laser beam. Since the mode selecting grating monochromator is before the etalon in this experiment, the laser beam angle will shift as the laser frequency is scanned (the grating angle is kept fixed during the scan). This changing angular misalignment will produce an observed free spectral range different from the one calculated using equation IV-1.

Flicker et al.<sup>(43)</sup> have shown that this can result in large calibration errors when an air-gap etalon is used in conjunction with a high dispersion monochromator and a short focal length collimating element before the etalon. This error, defined to be the actual separation between two lines minus the observed frequency separation, was calculated using our experimental parameters and was found to equal  $+0.00006\text{ cm}^{-1}$  for a  $0.8\text{ cm}^{-1}$  measurement. It should be noted that the large index of refraction of germanium permits relatively large angular misalignments of the etalon to be made without introducing

significant changes in the observed free spectral range. The etalon errors are summarized in Table IV-2. The total error due to the etalon in the relative frequency measurements should range from approximately  $+0.0002 \text{ cm}^{-1}$  to  $-0.0001 \text{ cm}^{-1}$ .

Table IV-2  
Etalon Errors

Error Source	*Error ( $\text{cm}^{-1}$ )
Index of Refraction	$\pm 0.00012$
Etalon Thickness	$\pm 0.00004$
Scanning Error	$+0.00006$
Temperature Drift	$\pm 0.00010$

\*Assuming a  $0.8 \text{ cm}^{-1}$  measurement, except for the Temperature Drift, which is independent of the frequency range measured.

Fortunately, a total of seven laser modes were recorded that contained two calibration standards, separated by about  $0.8 \text{ cm}^{-1}$ , which could be used to test the accuracy of the frequency difference measurements. The frequency separation of the calibration standards was always very well known compared to the precision of our measurements. The results of these tests are given in Table IV-3. The measured frequency separations are averages of three to five trials and the assigned error is the standard deviation of these trials.

The average deviation between the actual frequency difference and the measured difference was  $-0.00004 \text{ cm}^{-1}$ , well below the precision of any one measurement. This indicates that there are no significant systematic errors in the calculated values for the etalon free spectral range or in the data. Also, the average assigned experimental error of  $0.00047 \text{ cm}^{-1}$  is close to the standard deviation of the measured frequency separations from the correct values. Because of this agreement, and since any systematic errors appear to be very small, the experimental error in the line frequencies was taken to be the standard deviation of the trials used in the measurement of each line. This error is probably dominated by random laser frequency fluctuations and etalon temperature drifts.

Table IV-3

## Diode Laser Calibration Accuracy Tests

Lines Used	Approx. Frequency Separation - $\Delta$ (cm <sup>-1</sup> )	Calc $\Delta$ - Meas $\Delta$ (cm <sup>-1</sup> )	Assigned Experimental Error in $\Delta$ (cm <sup>-1</sup> )
CO <sub>2</sub> - CO <sub>2</sub>	1.00	-0.00078	0.00037
N <sub>2</sub> O - N <sub>2</sub> O	0.77	+0.00049	0.00033
N <sub>2</sub> O - N <sub>2</sub> O	0.77	-0.00036	0.00072
N <sub>2</sub> O - N <sub>2</sub> O	0.77	+0.00001	0.00015
N <sub>2</sub> O - N <sub>2</sub> O	0.80	+0.00049	0.00064
N <sub>2</sub> O - N <sub>2</sub> O	0.80	-0.00018	0.00057
N <sub>2</sub> O - N <sub>2</sub> O	0.80	+0.00004	0.00050
		Average = -0.00004 cm <sup>-1</sup>	0.00047
		*(±0.00042 cm <sup>-1</sup> )	

\*This is the standard deviation of the measured frequency separations from the true separations.

The measured line frequencies are given in Table IV-4. The calculated error given in this table is the root mean square of the measurement error discussed above and the uncertainty in the calibration line frequency. The average calibration line error was  $\pm 0.0010$  cm<sup>-1</sup> and the average total error for the diode laser frequency measurements was  $\pm 0.0013$  cm<sup>-1</sup>. The lines denoted with an asterisk in Table IV-4 were measured with the NBS grating spectrometer. The average total error for all the frequencies given in Table IV-4 is  $\pm 0.0016$  cm<sup>-1</sup>.

#### IV. C. Strength Measurements and Error Analysis

Only a small fraction of the studies made with diode lasers have been concerned with the measurement of line strengths. Usually, the method of equivalent widths<sup>(44,45)</sup> has been used to determine the line strength from the observed absorption.<sup>(46)</sup> The line strength can also be determined from the line center absorption if the laser linewidth is negligible compared to the width of the absorption line.<sup>(37)</sup> Or, if the laser linewidth is not too large, the line

Table IV-4

Measured Transition Frequencies in  $\nu_2$  Band of H<sub>2</sub>S

Upper J'(K <sub>a</sub> ', K <sub>c</sub> ')-J(K <sub>a</sub> , K <sub>c</sub> )	Lower	Observed Frequency (cm <sup>-1</sup> )	Experimental Error (cm <sup>-1</sup> )	(a)Obs-Calc Frequency (cm <sup>-1</sup> )
6(2,5)-5(1,4)		1257.0689	0.0040	-0.0004
6(1,5)-5(2,4)		1257.0100	0.0034	-0.0016
5(4,1)-5(1,4)		1256.9713	0.0015	-0.0005
5(2,3)-4(3,2)		1256.8985	0.0025	-0.0017
9(4,6)-9(3,7)		1256.7848	0.0014	-0.0014
5(3,2)-4(4,1)		1256.7639	0.0016	-0.0007
9(3,6)-9(2,7)		1256.7313	0.0014	-0.0012
4(3,2)-3(2,1)		1253.4679	0.0010	0.0000
7(1,6)-7(0,7)		*1249.2231	0.0020	0.0008
3(3,0)-2(2,1)		*1248.3825	0.0020	0.0018
5(2,4)-4(1,3)		*1247.5366	0.0020	-0.0006
5(1,4)-4(2,3)		*1247.1994	0.0020	-0.0001
8(4,5)-8(3,6)		1246.0787	0.0012	-0.0010
8(3,5)-8(2,6)		1245.8463	0.0011	-0.0010
6(1,6)-5(0,5)		1243.6170	0.0013	0.0001
9(6,4)-9(5,5)		1243.5780	0.0011	0.0010
3(3,1)-2(2,0)		*1243.0679	0.0020	0.0010
7(3,5)-7(2,6)		1242.5596	0.0011	-0.0013
7(2,5)-7(1,6)		1242.5022	0.0013	-0.0012
4(2,2)-3(3,1)		*1241.3277	0.0020	0.0070
6(2,5)-6(1,6)		*1239.3377	0.0020	-0.0038
8(5,4)-8(4,5)		*1239.1324	0.0020	-0.0008
4(2,3)-3(1,2)		*1238.3986	0.0020	-0.0008
9(5,4)-9(4,5)		*1238.2410	0.0020	0.0021
4(1,3)-3(2,2)		1236.7275	0.0015	0.0004
8(4,4)-8(3,5)		1236.6533	0.0030	-0.0003
8(7,2)-8(6,3)		*1235.7061	0.0020	0.0004
7(4,4)-7(3,5)		*1235.3761	0.0020	-0.0022
8(6,3)-8(5,4)		1234.6136	0.0019	-0.0004
5(1,5)-4(0,4)		1234.5850	0.0019	0.0003
5(0,5)-4(1,4)		1234.5788	0.0019	0.0004
6(3,4)-6(2,5)		*1232.1437	0.0020	-0.0020
7(7,0)-7(6,1)		*1230.3327	0.0020	-0.0003
3(2,2)-2(1,1)		*1229.8478	0.0020	0.0002
5(2,4)-5(1,5)		*1229.3386	0.0020	0.0049
5(1,4)-5(0,5)		*1229.2731	0.0020	-0.0013
7(6,2)-7(5,3)		*1228.1318	0.0020	-0.0034
2(2,0)-1(1,1)		*1227.5982	0.0020	0.0028
9(7,2)-9(6,3)		*1226.3977	0.0020	-0.0021
9(6,3)-9(5,4)		*1225.9818	0.0020	-0.0023
4(1,4)-3(0,3)		*1225.4417	0.0020	-0.0015
6(4,3)-6(3,4)		*1225.1607	0.0020	-0.0012
6(6,1)-6(5,2)		1224.3336	0.0048	-0.0005
3(1,2)-2(2,1)		*1224.2811	0.0020	0.0019
8(5,3)-8(4,4)		*1223.9543	0.0020	0.0006



Table IV-4 (Continued)

Upper Lower $J'(K_a', K_c')-J(K_a, K_c)$	Observed Frequency ( $\text{cm}^{-1}$ )	Experimental Error ( $\text{cm}^{-1}$ )	(*)Obs-Calc Frequency ( $\text{cm}^{-1}$ )
7(4,3)-7(3,4)	*1222.9320	0.0020	-0.0022
6(3,3)-6(2,4)	*1221.9920	0.0020	-0.0037
5(3,3)-5(2,4)	*1221.8686	0.0020	0.0044
6(5,2)-6(4,3)	*1221.6799	0.0020	0.0035
5(2,3)-5(1,4)	1220.6479	0.0020	-0.0023
2(2,1)-1(1,0)	*1219.9501	0.0020	0.0015
8(6,2)-8(5,3)	*1218.6091	0.0020	0.0050
7(6,1)-7(5,2)	*1217.9880	0.0020	0.0011
5(5,1)-5(4,2)	*1216.8640	0.0020	0.0029
5(4,2)-5(3,3)	1216.4365	0.0013	-0.0005
3(1,3)-2(0,2)	1216.2968	0.0010	-0.0004
3(0,3)-2(1,2)	*1215.9665	0.0020	0.0007
7(5,2)-7(4,3)	*1213.3871	0.0020	-0.0006
4(3,2)-4(2,3)	*1212.4180	0.0020	0.0002
5(5,0)-5(4,1)	*1211.1931	0.0020	0.0026
6(4,2)-6(3,3)	*1210.4286	0.0020	-0.0005
4(4,1)-4(3,2)	*1210.3639	0.0020	0.0013
6(5,1)-6(4,2)	*1209.5985	0.0020	-0.0004
3(2,2)-3(1,3)	*1209.5252	0.0020	0.0026
5(3,2)-5(2,3)	1209.0831	0.0006	0.0005
4(2,2)-4(1,3)	1208.5210	0.0005	0.0002
3(1,2)-3(0,3)	1208.0164	0.0005	-0.0002
2(1,2)-1(0,1)	*1207.4508	0.0020	0.0012
2(0,2)-1(1,1)	*1205.7807	0.0020	0.0026
3(3,1)-3(2,2)	*1205.0435	0.0020	0.0003
5(4,1)-5(3,2)	*1203.4497	0.0020	-0.0004
4(4,0)-4(3,1)	1202.8244	0.0005	-0.0006
2(2,1)-2(1,2)	*1201.0267	0.0020	0.0002
4(3,1)-4(2,2)	1199.5292	0.0005	-0.0003
1(1,1)-0(0,0)	*1197.9709	0.0020	0.0037
3(2,1)-3(1,2)	*1197.4967	0.0020	0.0007
2(1,1)-2(0,2)	1196.8217	0.0004	0.0001
3(3,0)-3(2,1)	*1196.1755	0.0020	0.0014
2(2,0)-2(1,1)	1191.5453	0.0006	-0.0001
1(1,0)-1(0,1)	1188.7735	0.0004	-0.0002
6(3,3)-6(4,2)	1171.4822	0.0007	-0.0006
1(0,1)-2(1,2)	1158.1694	0.0005	-0.0001
2(1,2)-3(0,3)	1149.7713	0.0005	-0.0003
2(0,2)-3(1,3)	1149.4026	0.0008	-0.0004
4(0,4)-4(1,3)	1148.7198	0.0004	-0.0003
4(1,4)-4(2,3)	1148.4491	0.0004	-0.0001
1(1,0)-2(2,1)	1147.3581	0.0006	-0.0003
2(2,1)-3(1,2)	1144.2681	0.0008	0.0001
3(1,3)-4(0,4)	1140.1403	0.0006	-0.0007
3(0,3)-4(1,4)	1140.0855	0.0008	-0.0004
1(1,1)-2(2,0)	1139.5982	0.0005	-0.0001
2(1,1)-3(2,2)	1138.4452	0.0004	-0.0001
3(2,2)-4(1,3)	1132.8476	0.0004	0.0004
7(1,6)-7(2,5)	1132.7146	0.0007	-0.0000

Table IV-4 (Continued)

Upper $J'(K_a', K_c')$	Lower $J(K_a, K_c)$	Observed Frequency ( $\text{cm}^{-1}$ )	Experimental Error ( $\text{cm}^{-1}$ )	(a)Obs-Calc Frequency ( $\text{cm}^{-1}$ )
7(2,6)	-7(3,5)	1132.6721	0.0007	0.0005
4(1,4)	-5(0,5)	1130.5247	0.0005	0.0006
4(0,4)	-5(1,5)	1130.5172	0.0005	0.0007
5(5,0)	-6(4,3)	1129.1619	0.0003	0.0000
9(2,7)	-9(3,6)	1128.5689	0.0011	0.0007
9(3,7)	-9(4,6)	1128.5302	0.0013	0.0004
6(0,6)	-6(1,5)	1128.3660	0.0012	0.0002
6(1,6)	-6(2,5)	1128.3583	0.0013	0.0001
2(2,0)	-3(3,1)	1127.3454	0.0007	0.0005
4(2,3)	-5(1,4)	1123.2380	0.0010	-0.0005
8(1,7)	-8(2,6)	1123.0877	0.0013	-0.0007
8(2,7)	-8(3,6)	1123.0794	0.0014	-0.0008
4(1,3)	-5(2,4)	1122.8542	0.0011	-0.0007
5(0,5)	-6(1,6)	1120.8093	0.0016	-0.0016
4(4,1)	-5(3,2)	1120.5884	0.0016	-0.0025
10(2,8)	-10(3,7)	1119.4978	0.0018	0.0002
10(3,8)	-10(4,7)	1119.4895	0.0019	0.0003
6(1,6)	-7(0,7)	1110.9883	0.0050	-0.0022
6(2,5)	-7(1,6)	1104.9311	0.0050	-0.0039
6(1,5)	-7(2,6)	1104.9201	0.0050	-0.0035
5(4,2)	-6(3,3)	1104.3112	0.0050	-0.0032
7(0,7)	-8(1,8)	1101.0598	0.0010	-0.0001
7(1,7)	-8(0,8)	1101.0598	0.0010	-0.0001
6(3,4)	-7(2,5)	1098.2698	0.0004	-0.0006
6(2,4)	-7(3,5)	1097.9380	0.0005	-0.0003
7(1,6)	-8(2,7)	1095.6973	0.0003	0.0000
8(1,8)	-9(0,9)	1091.0226	0.0001	0.0000
8(0,8)	-9(1,9)	1091.0226	0.0001	0.0000
7(3,5)	-8(2,6)	1089.6241	0.0002	0.0002
7(2,5)	-8(3,6)	1089.5570	0.0004	0.0003
8(2,7)	-9(1,8)	1086.3629	0.0002	-0.0000
7(3,4)	-8(4,5)	1082.0329	0.0003	0.0002

\*Indicates that the transition frequency was measured with the NBS grating spectrometer.

(a)See Ch. V for details on the calculated frequencies.

strength can be determined from the line center absorption and then corrected for the distortion of the absorption line profile by the laser. For the reasons outlined below, this second method (called the direct method) is expected to yield more accurate line strengths and was used in this work.

One of the most difficult problems associated with any line strength measurement is the determination of the 100% transmission level in the region of the line. This is especially difficult for high pressure absorption when the line wing, described by a Lorentzian lineshape, absorbs an appreciable distance away from the line center. To avoid this problem the gas pressure was kept as low as possible in this experiment, usually between 0.15 and 0.25 torr. Under these conditions, the lineshape is very nearly Doppler, so that the absorption in the line wing goes to zero very rapidly.

In the method of equivalent widths, the line strength is determined from the integrated absorption of the line, and is therefore independent of the laser lineshape. This method has been used for most diode laser line strength measurements since the observed low pressure linewidths in these studies were 8% to 40% wider than the Doppler width, indicating that the observed absorption line profiles were significantly distorted. The accuracy of the equivalent width method, though, is more sensitive than the direct method to errors in the 100% transmission baseline<sup>(47)</sup> and to slight frequency non-linearities in the laser tuning.<sup>(37)</sup>

In our case, the observed low pressure linewidths were only about 1% larger than the Doppler width. Therefore, it was possible to measure the line strengths using the direct method, with corrections for distortion of the absorption line by the laser, and to avoid some of the errors associated with the use of equivalent widths. Also, the H<sub>2</sub>S data contained a number of blended lines with 3 to 1 strength ratios. The strengths of these blended lines can be measured much more easily using the direct method than the method of equivalent widths.

The intensity,  $I(\nu)$ , of a spectrum containing a single absorption line is given by Beer's law,

$$I(\nu) = I_0(\nu) e^{-k(\nu)X} \quad (\text{IV-2})$$

where  $I_0(\nu)$  is the intensity if there is no absorption,  $k(\nu)$  is the absorption coefficient, and  $X$  is the optical depth, which is equal to the pressure-pathlength product. For a Doppler lineshape the absorption coefficient has the form

$$k(\nu) = \frac{S}{\gamma_D} \sqrt{\frac{\ln 2}{\pi}} e^{-\ln 2 \left( \frac{\nu - \nu_0}{\gamma_D} \right)^2} \quad (\text{IV-3})$$

where  $S$  is the line strength,  $\nu_0$  is the frequency of the line center, and  $\gamma_D$  is the Doppler width and is equal to the half width at half height of the absorption coefficient. The Doppler width is given by

$$\gamma_D = \nu_0 \sqrt{\frac{2kT \ln 2}{Mc^2}} \quad (\text{IV-4})$$

where  $M$  is the molecular mass,  $k$  is Boltzmann's constant,  $T$  is the temperature, and  $c$  is the speed of light. From the line center transmission,  $T_0 = I(\nu_0)/I_0(\nu_0)$ , we can solve for the line strength since

$$S_D = \frac{\gamma_D \ln(1/T_0)}{PL \sqrt{\frac{\ln 2}{\pi}}} \quad (\text{IV-5})$$

The line strength calculated in this manner will be denoted by  $S_D$  since a Doppler lineshape was assumed. This quantity was determined for each absorption line and was subsequently corrected for the effects of pressure broadening and the laser lineshape on the absorption line profile.

If a saturated absorption scan was available, the 100% absorption level in each spectrum was compared to the signal level recorded when the shutter was blocking the laser beam. If the difference between the shutter signal and the 100% absorption level was greater than a few tenths of one percent, the saturated absorption level was used instead of the shutter zero as the  $I_0(\nu_0) = 0$  level. Saturated absorption scans were made for all but seventeen of the lines measured. These seventeen lines are marked in Table IV-5, which is a listing of the measured line strengths.

Fifteen of these seventeen lines were in the P branch region since the H<sub>2</sub>S absorption is so much weaker on the low frequency side of the band. The saturated absorption levels of all but two of the other P branch region lines were less than 1% higher than the shutter zero, and averaged only 0.3% higher. The other two saturated absorption levels were 1.9% and 1.6% higher than the shutter zero. These two lines were recorded with the highest currents used with the P branch region laser, for which poorer mode quality and separation can be expected. Since the lines for which saturated absorption scans were not made occurred at lower laser currents, it is likely that the shutter zero is an accurate measure of the 100% absorption for these scans. Rather high error bars were assigned to most of the strengths measured for these lines anyway since their spectra had to be recorded at relatively high pressures.

Only two lines recorded with the R branch region laser could not be saturated to check the shutter zero level. The shutter zero and the saturated absorption level were within 3% of each other for all but four of the other transitions in this region. The saturated absorption level was from 3% to 9% higher than the shutter zero for these four transitions. The two lines that could not be saturated in the R branch region were recorded with low laser injection currents for which the agreement between the shutter zero and the 100% absorption level was always better than 1%, when it could be measured.

Corrections to  $S_D$  for the effects of any pressure broadening can be determined using the Voigt lineshape, which is a convolution of the Doppler and pressure broadened Lorentzian absorption line profiles. For 80% of the lines measured here the pressure was less than 0.4 torr, so that these corrections are small, although not negligible when compared to other error sources. The corrections for these low pressure lines were determined in conjunction with corrections for distortion of the line profile by the laser and will be discussed later. Eighteen lines were recorded with pressures ranging from 0.4 to 4 torr. The pressure broadening corrections to these lines will now be discussed.

The Voigt lineshape is given by<sup>(48)</sup>

$$k^v(\nu) = \frac{k_0 y}{\pi} \int_{-\infty}^{\infty} \frac{e^{-y^2}}{y^2 + (x - t)^2} dt \quad (IV-6)$$

where

$$k_0 = \frac{S}{\gamma_D} \sqrt{\frac{\ln 2}{\pi}}, \quad y = \frac{\gamma_L}{\gamma_D} \sqrt{\ln 2}, \quad x = \left( \frac{\nu - \nu_0}{\gamma_D} \right) \sqrt{\ln 2}$$

and

$$\gamma_L = \gamma_L^0 P.$$

$k_0$  is the absorption coefficient at  $\nu_0$ , the line center, for a Doppler lineshape.  $\gamma_L$  is the half width at half height of the pressure broadened Lorentzian lineshape,  $\gamma_L^0$  is the pressure broadening coefficient in  $\text{cm}^{-1}/\text{atm}$ , and  $P$  is the pressure in atm. At the line center  $k^v(\nu = \nu_0)$  can be considerably simplified<sup>(48)</sup> to give

$$k^v(\nu_0) = k_0 e^{y^2} (1 - \text{erf}(y)). \quad (IV-7)$$

The line strength corrected for the effects of pressure broadening, denoted by  $S_p$ , is therefore given by

$$S_p = \frac{S_D}{e^{y^2} (1 - \text{erf}(y))}. \quad (IV-8)$$

For the pressures used here  $y$  is always less than 1 so that  $\text{erf}(y)$  can be accurately calculated from the power series

$$\text{erf}(y) = \frac{2}{\sqrt{\pi}} \int_0^y e^{-t^2} dt = \frac{2}{\sqrt{\pi}} \sum_{n=0}^{\infty} \frac{(-1)^n y^{2n+1}}{n! (2n+1)}. \quad (IV-9)$$

The correction to  $S_D$  for pressure broadening as a function of  $y$  is plotted in Fig. IV-1. For example, if a line with a Doppler width of  $0.0012 \text{ cm}^{-1}$  and a pressure broadening coefficient of  $0.1 \text{ cm}^{-1}/\text{atm}$  was recorded at a pressure of 1 torr, Fig. IV-1 shows that the value of  $S_D$  found for this line must be increased 10% to account for the decrease in the line center absorption due to pressure broadening.

If  $\gamma_L$  is known, the correction to  $S_D$  for pressure broadening can be calculated.

Olivero and Longbothum<sup>(49)</sup> have developed an empirical equation for the half width of the

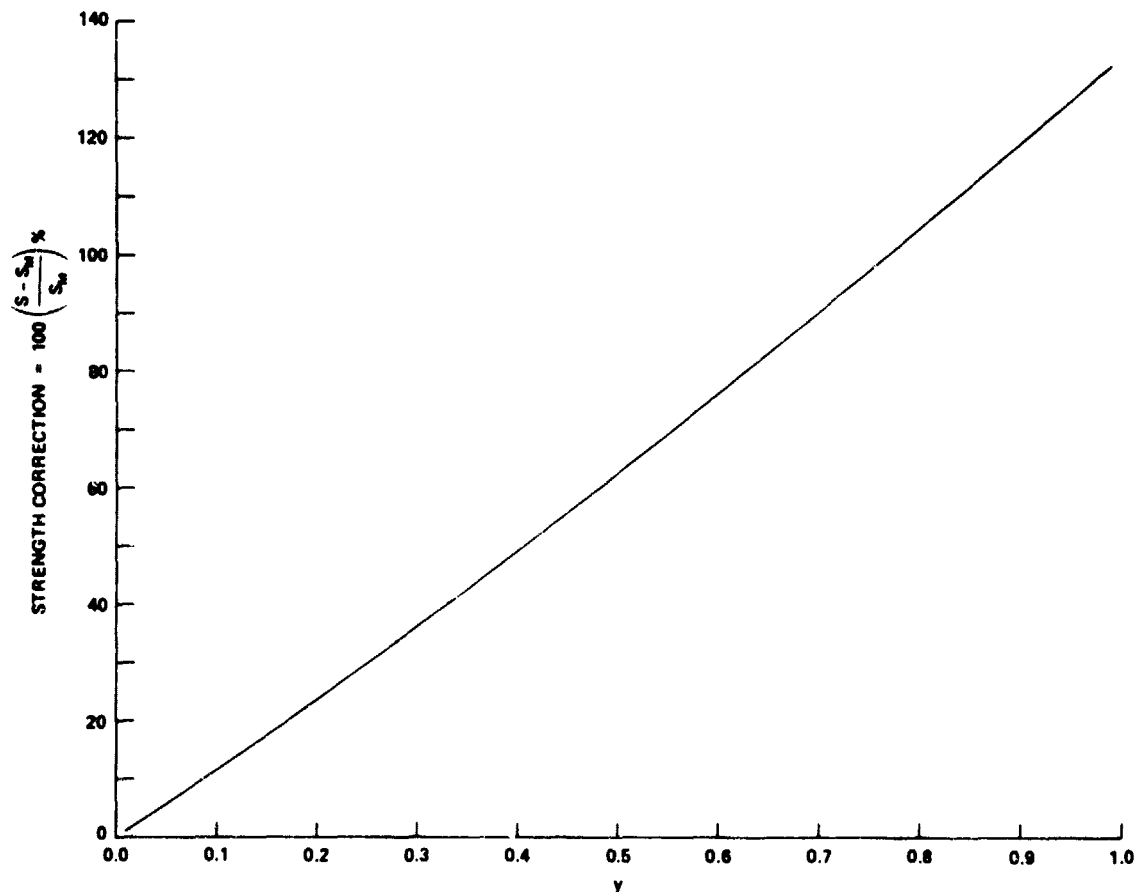


Figure IV-1. Correction to Measured Line Strength,  $S_M$ , as a Function of  $y = \frac{\gamma_L}{\gamma_D} \sqrt{\ln 2}$

Voigt lineshape,  $\gamma_V$ , as a function of  $\gamma_L$  and  $\gamma_D$ . This equation can be inverted<sup>(47)</sup> to obtain

$$\gamma_L = \gamma_V \left( 7.7254 - 6.7254 \sqrt{1 + 0.3195 (\gamma_D/\gamma_V)^2} \right). \quad (\text{IV-10})$$

This relation was used to determine  $\gamma_L$  and therefore  $\gamma_L^0$  from the measured halfwidths of nine of the lines, all recorded at pressures greater than 1 torr. The residual line broadening of about 1% due to the diode laser linewidth was neglected since the observed linewidths were 20% to 50% wider than the Doppler width.

For these nine lines, the measured pressure broadening coefficient was used for the correction of each line strength. The error in the  $\gamma_L^0$  values was estimated to be about  $\pm 0.02 \text{ cm}^{-1}/\text{atm}$ . The uncertainty in the line strength correction from the uncertainty of  $\pm 0.02 \text{ cm}^{-1}/\text{atm}$  in  $\gamma_L^0$  was included in the total error for these line strength measurements.

The measured values of  $\gamma_L^0$  ranged from 0.11 to 0.19 cm<sup>-1</sup>/atm, the average being 0.15 cm<sup>-1</sup>/atm. The lower state J values of these lines varied from J = 2 to J = 10.

The average value for  $\gamma_L^0$  of 0.15 cm<sup>-1</sup>/atm was used to determine the pressure broadening corrections for the remainder of lines measured at pressures between 0.4 and 1 torr. Errors corresponding to an uncertainty of  $\pm 0.05$  cm<sup>-1</sup>/atm in  $\gamma_L^0$  were included in the error bars for these line strengths. This uncertainty of  $\pm 0.05$  cm<sup>-1</sup> in the average value of  $\gamma_L^0$  is large enough to encompass all nine of the values of  $\gamma_L^0$  measured here.

The corrections to  $S_D$  for these 18 lines ranged from 7% to 60% and the resulting errors in the line strengths from the uncertainty in these corrections ranged from 2% to 10%.

A good estimate of the diode laser lineshape is required to determine its effect on an absorption line profile. Studies<sup>(50,51)</sup> of line profile distortions in diode laser spectra have assumed that the laser lineshape is Gaussian. Also, previous line strength measurements<sup>(37)</sup> using the direct method were not corrected for laser lineshape effects since the assumption of a Gaussian shape led to a negligible correction.

In a review of the literature, six direct measurements of the lineshape and linewidth of a diode laser were found.<sup>(28-33)</sup> These measurements were all performed by heterodyning the output of a diode laser with a highly stable and very narrow CO<sub>2</sub> or CO laser line. In all six cases the observed diode laser lineshape was clearly best described by a Lorentzian lineshape. The diode laser linewidths in these measurements varied from less than 2 MHz to greater than 20 MHz full width at half height. We therefore determined our corrections to the measured line strengths using a Lorentzian lineshape for the laser emission profile.

To determine the effect of the laser lineshape on the line profile and to find corrections for the measured line strengths a procedure similar to that used in grating spectroscopy was followed.<sup>(47,52)</sup> The laser lineshape was convolved with a series of Doppler absorption line profiles for various ratios of the laser linewidth to the Doppler width. Using these convolutions, corrections to the line strength can be determined either from the laser linewidth, if it is known, or from the observed broadening of the line above the Doppler



width, if this broadening can be measured accurately enough. Convolutions were performed for both a Gaussian and Lorentzian lineshape. The Gaussian lineshape convolutions were made for comparison purposes and to check our convolution routine since the results of other convolutions of a Gaussian with a Doppler line profile are available in the literature.<sup>(52)</sup>

The convolved line profile, for a laser lineshape described by the function  $f(\nu - \nu')$  is given by

$$A_{\text{OBS}}(\nu) = \int_{-\infty}^{\infty} A_{\text{TRUE}}(\nu') f(\nu - \nu') d\nu' \quad (\text{IV-11})$$

where  $A_{\text{OBS}}$  and  $A_{\text{TRUE}}$  are the observed and true absorption of the line. For a Lorentzian laser lineshape

$$f(\nu - \nu') = \frac{1}{\pi} \frac{\alpha_{\text{DL}}}{(\nu - \nu')^2 + \alpha_{\text{DL}}^2} \quad (\text{IV-12})$$

and for a Gaussian laser lineshape

$$f(\nu - \nu') = \frac{1}{\alpha_{\text{DL}}} \sqrt{\frac{\ln 2}{\pi}} e^{-\ln 2 \left( \frac{\nu - \nu'}{\alpha_{\text{DL}}} \right)^2} \quad (\text{IV-13})$$

where  $\alpha_{\text{DL}}$  is the laser linewidth. The lineshape functions have been properly normalized so that

$$\int_{-\infty}^{\infty} f(\nu - \nu') d\nu' = 1. \quad (\text{IV-14})$$

The convolutions were performed numerically with a desktop computer. The ratio of the laser linewidth to the Doppler width was varied from 2% to 50% and the true absorption of the Doppler profile was varied from about 3% to 97%. To save computation time the convolved profile was only evaluated at line center and in the vicinity of its halfwidth point, defined as the halfwidth of the effective absorption coefficient giving rise to this convolved profile.

The results of these convolutions, in terms of corrections to the measured line strengths, are plotted in Fig. IV-2 for a Lorentzian laser lineshape and in Fig. IV-3 for a

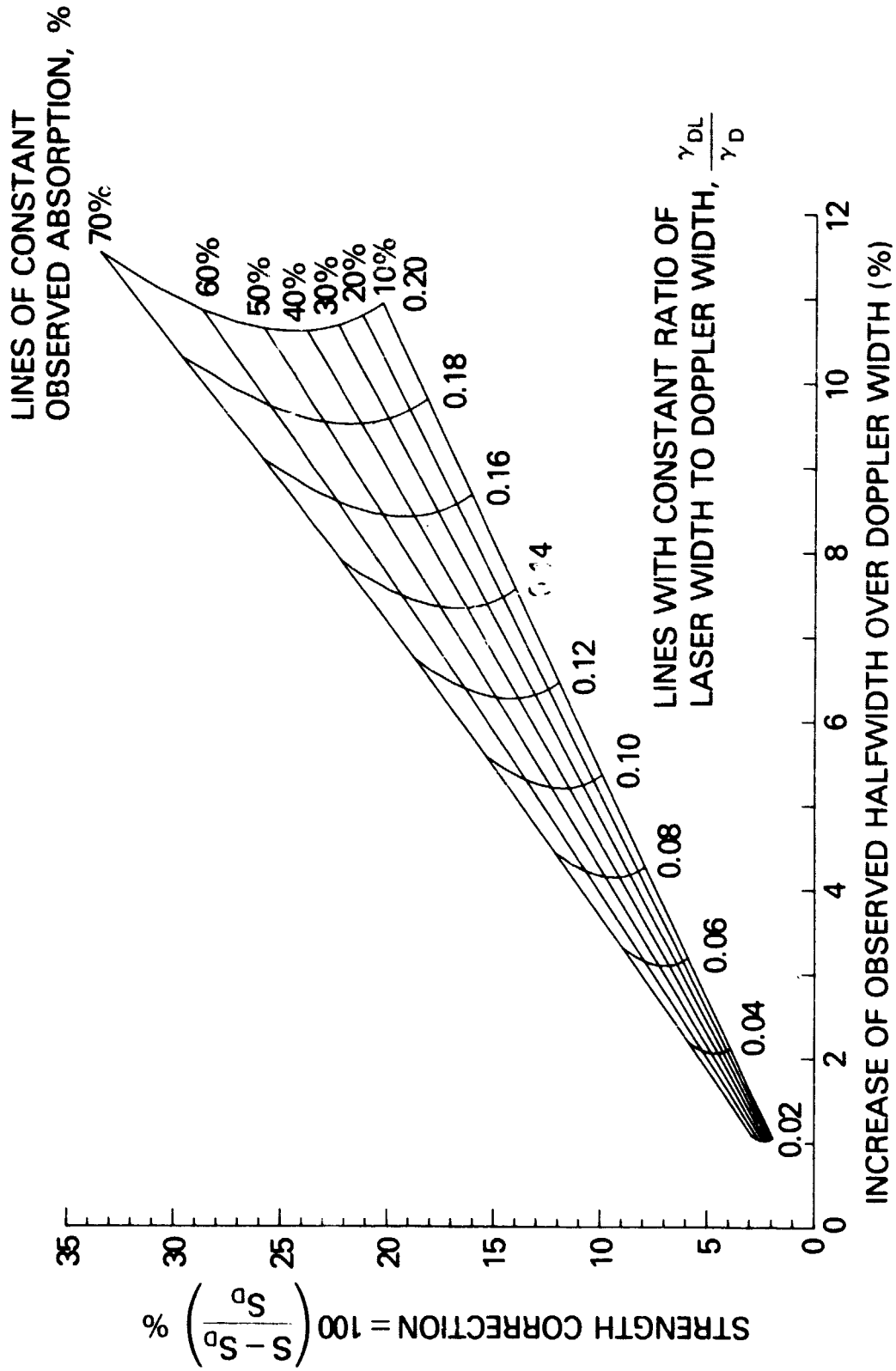


Figure IV-2. Correction to Measured Line Strength,  $S_D$ , for a Lorentzian Laser Lineshape

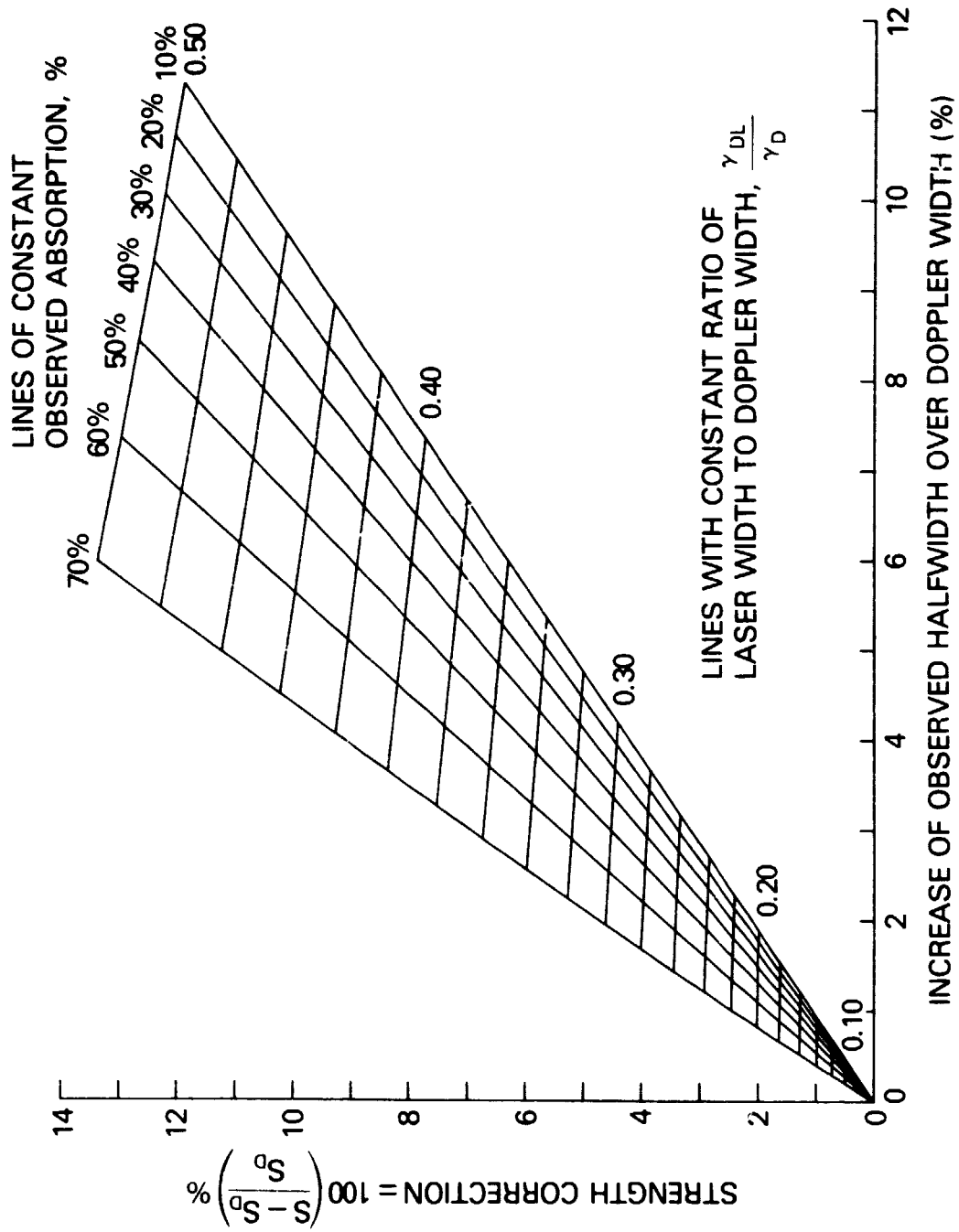


Figure IV-3. Correction to Measured Line Strength,  $S_D$ , for a Gaussian Laser Lineshape

Gaussian lineshape. In each of these figures, lines of constant observed absorption are plotted as well as correction curves for a constant ratio of the laser width to the Doppler width.

As one would expect, for a given laser linewidth the line center absorption is decreased much more by the Lorentzian lineshape since its wings extend so far compared to the wings of the Gaussian lineshape. For example, if the laser width is 20% of the Doppler width, the line strength correction for a Gaussian laser lineshape is 2% while the correction for a Lorentzian laser lineshape is about 23%. If the line strength correction is determined from the observed increase in the linewidth the difference between the two laser lineshapes is smaller. If the laser lineshape is Gaussian and the absorption line is broadened by X%, the line strength correction will also be about X%. If the laser lineshape is Lorentzian though, a broadening of X% in the observed line indicates that a line strength correction of about 2X% is required.

Since the diode laser linewidth could not be directly measured, the strength corrections were determined from the increase of the observed H<sub>2</sub>S linewidths over the Doppler width. Since the Doppler width of H<sub>2</sub>S in the  $\nu_2$  band is only about 0.0012 cm<sup>-1</sup>, the halfwidth measurement of a single line is not nearly accurate enough to use for the determination of the strength correction. Also, even at pressures below 0.4 torr, pressure broadening can distort the line profile as much as the laser lineshape. Therefore, the average of a large number of low pressure linewidth measurements was used to determine the combined line strength correction due to pressure broadening and the laser lineshape.

A total of 513 low pressure linewidths from 66 different transitions were used to measure the average broadening. The average pressure for these linewidth measurements was 0.24 torr and the average absorption was 45%. Care was taken to exclude any blended lines from the average. Several transitions recorded using laser modes with poor frequency stability were also excluded. The mean ratio of the observed halfwidth to the Doppler width for these transitions was 1.013. The standard deviation of the average linewidth ratio for each of the 66 transitions about the mean ratio was  $\pm 0.021$ . This number is believed to be a conservative estimate of the amount of variation in the line broadening

of these transitions since it may also contain a contribution from the rather large random error in any one individual linewidth measurement. The probability that this estimate is on the high side is supported by the fact that the mean ratio minus one standard deviation is less than one, implying an observed width smaller than the Doppler width. The test results given in Table IV-3 show that there is no possibility of a systematic error in the linewidth measurements due to a poor relative frequency scale. The average linewidth ratio obtained here should statistically be very accurate, since it was determined from 513 linewidth measurements.

The average linewidth ratio plus one standard deviation, or 1.034, was taken as the upper limit of the observed line broadening. If due totally to the laser, this excess broadening of 3.4% implies a laser linewidth of 2 MHz. This maximum ratio of the observed halfwidth to the Doppler width implies a maximum correction to the measured line strengths of 7% for any combination of broadening due to the laser lineshape and the gas pressure. The minimum possible correction to the line strengths was determined to be 3%. This minimum is the combined correction for a laser linewidth of 0.5 MHz, the smallest linewidth usually observed for diode lasers, and for a pressure broadening coefficient of  $0.07 \text{ cm}^{-1}/\text{atm}$ , which is one half the value of the average pressure broadening coefficient measured for  $\text{H}_2\text{S}$ . Our best estimate for the low pressure line strength corrections is therefore  $5\% \pm 2\%$ . If the laser was assumed to have a Gaussian rather than Lorentzian lineshape, the line strength correction was found to be  $3\% \pm 2\%$ , 2% lower than the correction for a Lorentzian lineshape.

As previously mentioned, the strength corrections were determined from a set of absorption lines whose average peak absorption was 45%. If the observed excess line broadening was due solely to the diode laser linewidth, the correction to the line strength would depend upon the peak absorption of the line being measured. In this case, a laser linewidth that results in a 5% correction at an absorption of 45% should be used for the calculation of the strength corrections. If the excess broadening was due completely to pressure broadening, the line strength correction is not a function of the line center absorption.

However, since the correction curves shown in Fig. IV-2 for different laser linewidths are almost parallel as the peak absorption is varied, it is not necessary to know the relative amounts of laser and pressure broadening very accurately. Also, because the vast majority of the strength measurements were made using lines with peak absorptions between 30% and 70%, the variation with absorption of any one of the possible laser correction curves is at most only  $\pm 0.6\%$ . We could therefore use a constant correction factor of 5% for the line strengths.

Eight of the transitions measured here were blended doublets whose lines have a known strength ratio of 3 to 1. The frequency separation of the two lines in each doublet can be calculated from the  $\nu_2$  band constants, which are discussed in Ch. V. With a knowledge of the frequency separation and the relative strengths, the strength of the stronger line,  $S_1$ , can be determined from the relation

$$S_1 = \frac{\gamma_D}{PL \sqrt{\frac{\ln 2}{\pi}}} \frac{\ln(1/T_0)}{\alpha} \quad (\text{IV-15})$$

where  $T_0$  is the minimum transmission of the blended doublet. The factor  $\alpha$  is given by

$$\alpha = e^{-\ln 2 \left( \frac{\nu - \nu_1}{\gamma_D} \right)^2} + \frac{1}{3} e^{-\ln 2 \left( \frac{\nu - \nu_2}{\gamma_D} \right)^2} \quad (\text{IV-16})$$

where  $\nu$  is the frequency at which the blended doublet profile has its peak absorption, and  $\nu_1$  and  $\nu_2$  are the unblended line center frequencies of the stronger and weaker lines in the doublet. The frequency differences  $\nu - \nu_1$  and  $\nu - \nu_2$  were determined from a theoretical calculation of the blended line profiles using a Doppler lineshape and the known strength ratio and unblended frequency separation. All but one of the blended doublets were measured at low pressures. The doublet  $12_{2,10} - 12_{3,9}$ ,  $12_{3,10} - 12_{4,9}$  was measured at about 2.2 torr, but the error in using a Doppler instead of a Voigt lineshape in this calculation should be small compared to other errors in the measurement of its line strength.  $S_1$  for each doublet was then increased by 5% to correct for the effects of the laser linewidth and pressure broadening. Two of the doublets were measured at line separations of less than

$0.00001 \text{ cm}^{-1}$ , while the other separations varied from  $0.00015 \text{ cm}^{-1}$  to  $0.00196 \text{ cm}^{-1}$ . Since the line blending was very severe for all of these doublets,  $\alpha$  always had a value close to  $4/3$ .

The line strength measurements will now be summarized and the use of the direct method in making these measurements discussed. The first step was to determine, if possible, the 100% absorption level from saturated absorption scans. Then the quantity  $S_D$ , given in equation IV-5, was calculated for all the unblended lines with the assumption that the line profile was Doppler. For all the lines measured at pressures less than 0.4 torr  $S_D$  was increased by 5% to correct for the effects of pressure broadening and the laser lineshape on the observed line profile. Three sources of error were considered in determining the total error for these line strengths. The total error was taken to be the root mean square of the 2% error in the combined correction for pressure broadening and the laser lineshape, the 1% estimated error in the gas pressure measurement, and the standard deviation of the individual strengths used to obtain an average line strength for each transition. The uncertainty of  $\pm 0.3\%$  in the gas cell pathlength was small enough to be neglected. The average total error for these line strengths was 2.7%.

Eighteen transitions were measured at pressures greater than 0.4 torr. Their strengths,  $S_D$ , were corrected for pressure broadening using equation IV-8. To calculate this correction one must know the pressure broadening coefficient,  $\gamma_L^0$ , for the line being measured. Nine of these eighteen line strengths were corrected using the measured value of  $\gamma_L^0$  for each line. The average value of  $\gamma_L^0$  for these nine lines was used to calculate the correction for the other nine lines, which were recorded at too low a pressure for their pressure broadening coefficient to be measured. The resulting line strengths were then increased another 3% for the effects of the laser lineshape on the line profile. The 5% correction used for the low pressure measurements was for both pressure broadening and for distortion of the line profile by the laser so that increasing these eighteen lines by the full 5% would result in a slight over-correction for pressure broadening. Therefore, an estimated correction for the laser distortion alone of 3% was used, this being the lower bound of full  $5\% \pm 2\%$  correction. An uncertainty of  $\pm 2\%$  was also assigned to this 3% correction.

In general, though, the total error in these higher pressure measurements was dominated by the uncertainty in  $\gamma_L^0$ . The errors in these eighteen strengths were determined the same way as the errors in the low pressure strength measurements, except for an extra term added to account for the error from the uncertainty in the values of  $\gamma_L^0$  used to calculate the pressure broadening corrections. The average total error for these line strengths was 6.6%.

The averaged strengths and their experimental errors are listed in Table IV-5. Their values have been normalized to 300K using the relation

$$S(T_0 = 300K) = S(T) \left( \frac{T}{T_0} \right)^{5/2} e^{-\frac{E_i}{k} \left( \frac{1}{T_0} - \frac{1}{T} \right)} \frac{(1 - e^{-h\nu/kT_0})}{(1 - e^{-h\nu/kT})} \quad (IV-17)$$

which can be derived from equation II-32 and the dependence of Q and N on temperature. The partition function Q is primarily dependent on temperature through its rotational part, given in equation VI-2. N, the number of molecules/cm<sup>3</sup>-atm, is inversely proportional to temperature. The listed strengths have also been divided by 0.9502 to account for the naturally occurring abundance<sup>(53)</sup> of the sulphur 32 isotope. The average total error for all the line strengths in this table is 3.4%.

We have found the direct method of measuring line strengths to have an accuracy of about 3%. However, the relatively high accuracy of the direct method can only be retained if the line broadening due to the diode laser is less than several percent. Also, the gas pressure must be kept very low, or else the pressure broadening coefficient must be measured for each transition if the highest possible accuracy is to be achieved. In other line strength studies using diode lasers,<sup>(46)</sup> low pressure linewidths 8% to 40% greater than the Doppler widths have been observed. To keep the error in the strength correction for these lines below 5% for example, their linewidths must be measured to an accuracy of about 2%, which is difficult to achieve without a large number of measurements, especially for heavy molecules with small Doppler widths. Also, the line strength correction factor becomes more sensitive to the details of the actual laser lineshape and to the observed absorption level as the distortion of the line profile by the laser increases.



Table IV-5

Measured Line Strengths in  $\nu_2$  Band of  $H_2S$ 

Upper $J'(K_a', K_c')$	Lower $J(K_a, K_c)$	Observed Strength ( $cm^{-1}/atm-cm$ )	Experimental Error (%)	(a)F Factor	Calculated Frequency ( $cm^{-1}$ )	(b)	(c)
6(2,5)	5(1,4)	1.62E-02	2.7	1.44	1257.068		
6(1,5)	5(2,4)	5.44E-03	3.1	1.45	1257.010		
5(4,1)	5(1,4)	3.11E-04	3.9	4.71	1256.972		X
5(2,3)	4(3,2)	1.13E-02	3.0	1.84	1256.899		
9(4,6)	9(3,7)	1.41E-03	2.8	3.95	1256.783		
5(3,2)	4(4,1)	2.34E-03	2.6	1.81	1256.764		
9(3,6)	9(2,7)	4.31E-03	2.7	4.01	1256.729		
4(3,2)	3(2,1)	1.85E-02	2.5	2.23	1253.468		
8(3,6)	8(2,7)	7.50E-03	2.3	4.43	1252.874		
8(2,6)	8(1,7)	2.45E-03	2.4	4.34	1252.862		
8(4,5)	8(3,6)	6.56E-03	2.5	3.72	1246.076		
8(3,5)	8(2,6)	2.29E-03	3.1	3.89	1245.843		
D 6(1,6)	5(0,5)	1.66E-02	2.7	0.96	1243.617		
* 6(0,6)	5(1,5)	5.54E-03	2.7	0.96	1243.616		
7(3,5)	7(2,6)	3.09E-03	2.3	3.64	1242.557		
7(2,5)	7(1,6)	9.11E-03	2.6	3.57	1242.500		
4(1,3)	3(2,2)	5.03E-03	2.4	1.52	1236.727		
8(4,4)	8(3,5)	1.70E-03	3.4	2.92	1236.650		
8(7,2)	8(6,3)	2.92E-03	2.8	2.61	1235.705		
8(6,3)	8(5,4)	4.38E-03	2.6	2.84	1234.613		
5(1,5)	4(0,4)	6.80E-03	2.4	1.14	1234.585		
5(0,5)	4(1,4)	2.04E-02	2.4	1.14	1234.579		
7(5,3)	7(4,4)	2.44E-03	2.8	2.79	1229.354		
5(2,4)	5(1,5)	3.53E-03	2.6	3.14	1229.333		
5(1,4)	5(0,5)	1.07E-02	2.4	3.18	1229.273		
4(1,4)	3(0,3)	1.91E-02	2.8	1.13	1225.443		
4(0,4)	3(1,3)	6.40E-03	3.0	1.14	1225.395		
6(4,3)	6(3,4)	1.08E-02	2.4	2.65	1225.161		
6(6,1)	6(5,2)	5.06E-03	3.6	2.45	1224.333		
3(1,2)	2(2,1)	7.84E-03	2.5	1.46	1224.279		
5(2,3)	5(1,4)	1.25E-02	3.2	2.49	1220.649		
6(6,0)	6(5,1)	1.58E-03	2.4	2.22	1220.589		
2(2,1)	1(1,0)	1.38E-02	3.6	1.46	1219.949		
4(1,3)	4(0,4)	3.65E-03	2.4	2.59	1218.947		
5(5,1)	5(4,2)	2.56E-03	2.4	2.26	1216.760		
5(4,2)	5(3,3)	4.17E-03	3.3	2.38	1216.437		
3(1,3)	2(0,2)	5.68E-03	2.6	1.23	1216.297		
3(0,3)	2(1,2)	1.59E-02	2.9	1.16	1215.965		
7(5,2)	7(4,3)	7.30E-03	2.6	1.96	1213.387		
4(3,2)	4(2,3)	1.37E-02	3.0	2.24	1212.418		
5(5,0)	5(4,1)	8.04E-03	2.7	2.11	1211.190		
6(5,1)	6(4,2)	3.25E-03	2.5	1.94	1209.599		X
3(2,2)	3(1,3)	3.76E-03	3.0	2.28	1209.523		X
5(3,2)	5(2,3)	1.40E-02	2.7	2.08	1209.082		
3(1,2)	3(0,3)	1.15E-02	2.3	2.25	1208.016		

Table IV-5 (Continued)

Upper Lower	Observed Strength (cm <sup>-1</sup> /atm-cm)	Experimental Error (%)	(a)F Factor	Calculated Frequency (cm <sup>-1</sup> )	(b)	(c)
2(1,2)-1(0,1)	1.25E-02	2.3	1.29	1207.449		
3(3,1)-3(2,2)	3.50E-03	3.3	1.84	1205.043		
4(4,0)-4(3,1)	3.79E-03	2.4	1.78	1202.825		
4(3,1)-4(2,2)	5.86E-03	2.3	1.66	1199.530		
2(1,1)-2(0,2)	3.76E-03	2.4	1.68	1196.822		
2(2,0)-2(1,1)	4.95E-03	2.5	1.31	1191.546		
3(2,1)-3(3,0)	5.05E-03	2.5	0.56	1175.161		
5(3,2)-5(4,1)	3.69E-03	2.6	0.47	1175.088		
1(0,1)-2(1,2)	6.40E-03	2.3	0.78	1158.169		
2(1,2)-3(0,3)	9.05E-03	2.6	0.81	1149.771		
2(0,2)-3(1,3)	2.91E-03	2.5	0.78	1149.403		
4(0,4)-4(1,3)	7.12E-05	4.4	0.063	1148.720		X
4(1,4)-4(2,3)	2.01E-04	5.0	0.059	1148.449		X
1(1,0)-2(2,1)	3.06E-03	2.5	0.41	1147.359		
2(2,1)-3(1,2)	2.39E-03	2.6	0.56	1144.268		
3(1,3)-4(0,4)	3.42E-03	2.5	0.80	1140.141		
3(0,3)-4(1,4)	1.02E-02	2.4	0.80	1140.086		
2(1,1)-3(2,2)	9.28E-04	2.5	0.41	1138.446		
3(2,2)-4(1,3)	1.27E-03	2.4	0.53	1132.847		
4(1,4)-5(0,5)	1.02E-02	2.3	0.80	1130.524		
4(0,4)-5(1,5)	3.39E-03	2.4	0.80	1130.517		
5(5,0)-6(4,3)	1.32E-04	4.2	0.87	1129.162	X	X
9(2,7)-9(3,6)	1.22E-04	4.8	0.17	1128.570	X	X
9(3,7)-9(4,6)	4.34E-05	8.3	0.18	1128.531	X	X
6(0,6)-6(1,5)	3.76E-05	9.4	0.062	1128.366	X	X
6(1,6)-6(2,5)	1.04E-04	9.1	0.057	1128.359	X	X
2(2,0)-3(3,1)	4.32E-04	5.5	0.16	1127.345	X	X
4(2,3)-5(1,4)	3.95E-03	2.6	0.51	1123.238		
8(1,7)-8(2,6)	8.52E-05	10.2	0.22	1123.085		X
8(2,7)-8(3,6)	2.51E-04	10.1	0.22	1123.077		X
4(1,3)-5(2,4)	1.29E-03	2.4	0.50	1122.854		
* 5(1,5)-6(0,6)	3.06E-03	2.5	0.80	1120.813		
D 5(0,5)-6(1,6)	9.19E-03	2.5	0.80	1120.812		
4(4,1)-5(3,2)	3.42E-04	6.3	0.39	1120.591		X
10(2,8)-10(3,7)	6.08E-05	6.9	0.45	1119.500	X	X
10(3,8)-10(4,7)	1.72E-04	6.6	0.43	1119.491	X	X
5(2,4)-6(1,5)	1.19E-03	2.6	0.51	1114.083		
5(1,4)-6(2,5)	3.63E-03	2.4	0.51	1114.015		
D 6(1,6)-7(0,7)	7.94E-03	2.9	0.82	1110.992		
* 6(0,6)-7(1,7)	2.55E-03	2.9	0.82	1110.992		
5(2,3)-6(3,4)	1.05E-03	2.6	0.24	1105.720		
6(2,5)-7(1,6)	3.01E-03	2.7	0.51	1104.935		
6(1,5)-7(2,6)	9.92E-04	2.8	0.51	1104.923		
5(4,2)-6(3,3)	1.15E-04	3.4	0.18	1104.316	X	X
* 12(2,10)-12(3,9)	5.20E-05	9.6	1.50	1101.248	X	X
D 12(3,10)-12(4,9)	1.56E-04	9.6	1.50	1101.248	X	X
D 7(0,7)-8(1,8)	6.02E-03	2.7	0.80	1101.062		
* 7(1,7)-8(0,8)	2.01E-03	2.7	0.80	1101.062		

Table IV-5 (Continued)

Upper $J'(K_a', K_c')$	Lower $J(K_a, K_c)$	Observed Strength ( $\text{cm}^{-1}/\text{atm-cm}$ )	Experimental Error (%)	(a) F Factor	Calculated Frequency ( $\text{cm}^{-1}$ )	(b)	(c)
6(3,4)	-7(2,5)	1.01E-03	3.2	0.28	1098.270	X	X
* 7(2,6)	-8(1,7)	7.85E-04	2.3	0.53	1095.699		
D 7(1,6)	-8(2,7)	2.35E-03	2.3	0.53	1095.697		
* 8(0,8)	-9(1,9)	1.46E-03	2.4	0.80	1091.023		
D 8(1,8)	-9(0,9)	4.39E-03	2.4	0.80	1091.023		
7(3,5)	-8(2,6)	2.60E-04	3.7	0.29	1089.624	X	
7(2,5)	-8(3,6)	7.61E-04	2.4	0.28	1089.557	X	
D 8(2,7)	-9(1,8)	1.67E-03	2.6	0.52	1086.363		
* 8(1,7)	-9(2,8)	5.55E-04	2.6	0.52	1086.363		
7(3,4)	-8(4,5)	1.74E-04	5.0	0.10	1082.034	X	X

(a) Observed line strength divided by calculated rigid rotor line strength - see Ch. VI.

(b) An X is placed in this column if a saturated absorption scan was not available to determine the 100% absorption level for the strength measurement.

(c) An X is placed in this column if the strength was measured at a gas pressure greater than 0.4 torr.

D- Denotes stronger line in blended doublet.

\*- Denotes weaker line in blended doublet. This line strength is obtained by dividing the stronger line strength by three.

In conclusion, this work has shown the feasibility of using diode lasers for wide ranging ( $>150\text{ cm}^{-1}$ ) studies of infrared vibrational bands. Relative line frequencies were measured to an accuracy of about  $\pm 0.0004\text{ cm}^{-1}$  with the diode laser spectrometer. Any systematic errors in the frequency measurements were shown to be very small. It was demonstrated that line strengths can be measured to an accuracy of about 3% using the direct method, if the diode laser linewidth is narrow enough. Corrections to the measured line strengths to account for the distortion of the line profile by the diode laser were calculated and the importance of using the proper laser lineshape to determine these corrections was shown.

## CHAPTER V

### ROTATIONAL ANALYSIS OF THE $\nu_2$ BAND OF H<sub>2</sub>S

#### V. A. Rotational Structure of the $\nu_2$ Band and Line Assignments

In this chapter, a least-squares analysis of the observed  $\nu_2$  band frequencies using Watson's AS and NS reduced Hamiltonians will be presented. A large part of this discussion will center on the characteristics of the AS Hamiltonian in the III<sup>r</sup> representation, which was found to fit the transition frequencies about 100 times worse than the other reduced Hamiltonians used in this work. First, the line assignments and some of the general features of the  $\nu_2$  band of H<sub>2</sub>S will be discussed.

In order to assign the observed transitions a trial spectrum of the  $\nu_2$  band was calculated with a computer program written by Maki<sup>(54)</sup>, which uses Watson's AS reduced Hamiltonian in the I<sup>r</sup> representation. This program also provides relative rigid rotor line strengths as well as the transition frequencies. Initial values for the band center and for A, B, and C in the upper vibrational state were taken from the work of Allen and Plyler,<sup>(2)</sup> who performed the only previous rotational analysis of this band. They were able to assign 55 transitions from 1080 cm<sup>-1</sup> to 1257 cm<sup>-1</sup> from a spectrum recorded with a resolution of 0.3 cm<sup>-1</sup>. The ground state constants for this trial calculation were obtained from a least-squares fit of the H<sub>2</sub>S pure rotational frequencies<sup>(16)</sup> to the AS-I<sup>r</sup> Hamiltonian. Terms up to sixth order in J were included in the ground state Hamiltonian. Although a better fit of the pure rotational frequencies could be obtained if higher order terms are included in the Hamiltonian, these terms are not required for the purpose of making line assignments.

With this first trial calculation about 20 lines in the R branch spectrum taken with the NBS grating spectrometer could be positively assigned. The measured frequencies for these 20 transitions were then fit to the AS-I<sup>r</sup> Hamiltonian to get approximate upper state values for A, B, C and the five quartic constants, which were in turn used in a second trial

calculation of the  $\nu_2$  band. This calculated spectrum was accurate enough to allow the rest of the R branch grating spectrum to be assigned. Another fit to the AS-IF Hamiltonian was then made using all of the lines assigned in the R branch grating spectrum so to determine as many upper state constants as possible. These constants were used to calculate one last trial spectrum of the  $\nu_2$  band in order to assign the H<sub>2</sub>S lines observed in the spectra taken with the diode laser spectrometer. Since the J values of the transitions observed with the diode laser spectrometer were no larger than those in the R branch grating spectrum, this calculated spectrum was sufficiently accurate for the assignment of all the lines in the diode laser spectra.

Although the spectrum of a highly asymmetric rotor appears to be a somewhat random collection of lines at first glance, there are some regularities in the spectrum which help with line assignments. A number of sub-bands with fairly regularly spaced lines were identified in the spectrum of H<sub>2</sub>S. In the R and Q<sup>RP</sup> branches, the six sub-bands

$$\begin{aligned} & (J)_{1,J-1} - (J)_{0,J} \quad , \quad (J)_{2,J-1} - (J)_{1,J} \\ & (J)_{1,J} - (J-1)_{0,J-1} \quad , \quad (J)_{0,J} - (J-1)_{1,J-1} \\ & (J)_{2,J-1} - (J-1)_{1,J-2} \quad \text{and} \quad (J)_{1,J-1} - (J-1)_{2,J-1} \end{aligned}$$

were observed with J usually running from one to about nine. As J increases, the two sub-bands shown together on each line above converge. For intermediate values of J, this gives rise to doublets in the spectrum from the two converging sub-bands. The assignment of the lines in these doublets to the proper sub-band is easy because the spin statistics of H<sub>2</sub>S require the ratio of their strengths to be equal to either 3 to 1 or 1 to 3, depending on the value of J. By J = 9 some of these converging sub-bands are separated by less than 0.0001 cm<sup>-1</sup> so that only a single line is observed in the spectrum. Detailed discussions of the general structure of asymmetric rotor vibration bands can be found in the book by Allen and Cross.<sup>(19)</sup>

A stick spectrum of only those transitions whose frequencies were measured in this work is shown in Fig. V-1. Below the plot of these transitions is a calculated stick spectrum for the  $\nu_2$  band. In these plots the length of the stick is proportional to

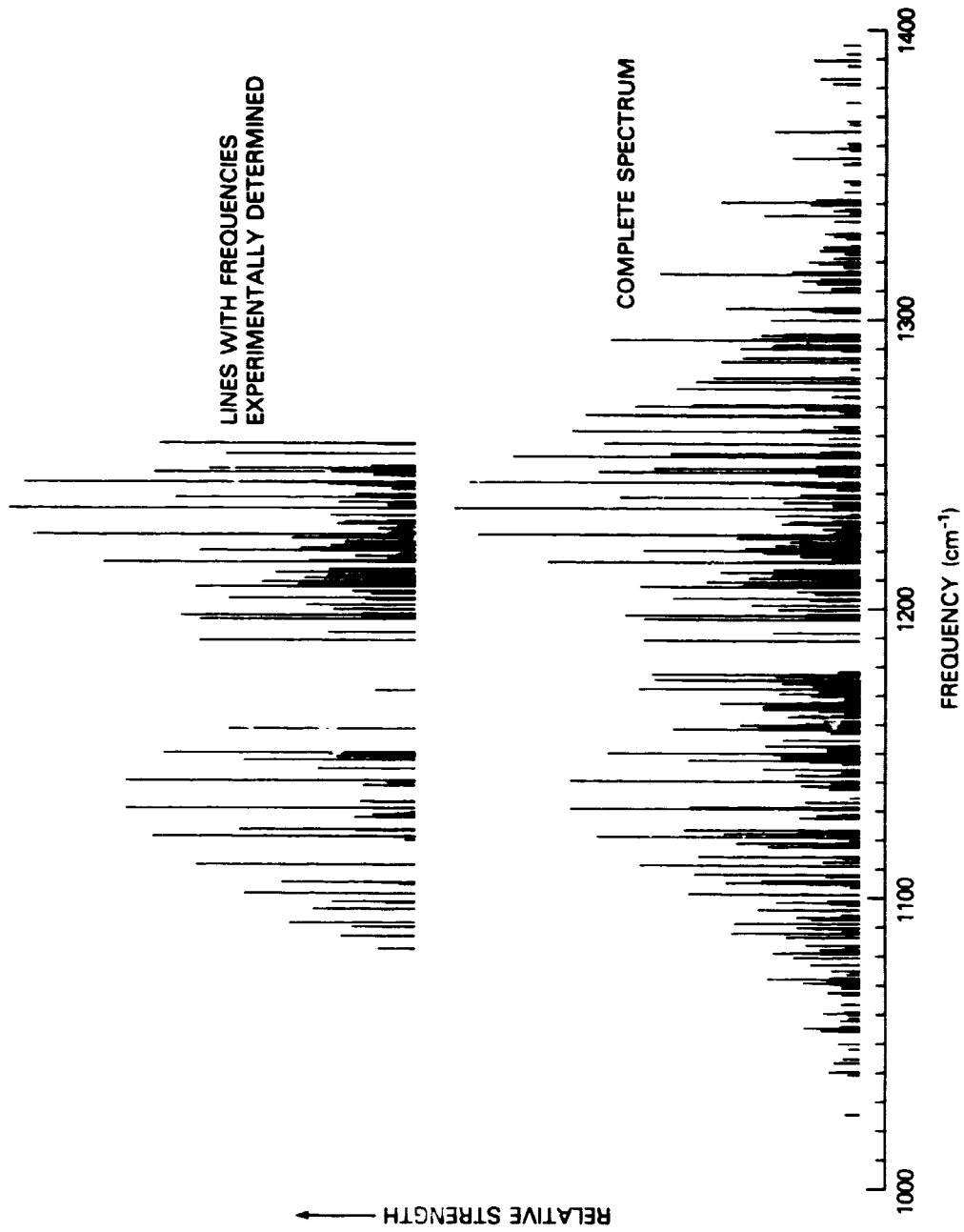


Figure V-1: Stick Spectrum of  $\nu_2$  Band of  $H_2S$  with Experimentally Observed Lines Indicated, Theoretical Rigid Rotor Strengths Used in this Plot

C-2

the relative rigid rotor strength for that transition. This spectrum was calculated using the AS- $I^r$  Hamiltonian to sixth order in angular momentum. The rotational constants for this Hamiltonian were determined from a least-squares fit of the  $\nu_2$  band and microwave pure rotational frequencies of  $H_2S$ . Though higher order terms in the ground state Hamiltonian are required to fit the microwave rotational data to its experimental accuracy, any changes to the stick spectrum from these terms would not be visible. These least-squares fits will be discussed in detail later in this chapter. In Fig. V-2 the calculated spectrum of  $\nu_2$  is again shown, but with the P, Q, and R branch lines displaced vertically from each other. In this figure the  $(J)_{1,J} - (J-1)_{0,J-1}$  and  $(J)_{0,J} - (J-1)_{1,J-1}$  sub-bands are indicated to illustrate two converging sub-bands. By  $J = 6$  these two sub-bands are separated by only  $0.0008\text{cm}^{-1}$ , less than the Doppler widths of the lines. The frequency difference between adjacent lines in each of these sub-bands is about  $9.1\text{cm}^{-1}$ , and is equal to the line separations in the  $R(J, K = J)$  series of an oblate symmetric top molecule with  $A_{H_2S} = B_{H_2S}$ , given by  $2(B_{H_2S} - C_{H_2S}) = 9.1\text{cm}^{-1}$ . The gap in the calculated spectrum at the band origin ( $\nu_0 \approx 1182.6\text{cm}^{-1}$ ) and the relatively spread out Q branch are the two main features that characterize this band as a type B asymmetric rotor band. When viewing the stick spectra in Fig. V-1 and V-2, it should be remembered that the line strengths shown are for a rigid rotor while in the experimentally observed spectrum the R branch is much stronger than the P branch.

As discussed in Chapter IV, the frequencies of 49 R and Q branch lines were measured with the NBS grating spectrometer and 77 P, Q, and R branch lines with the diode laser spectrometer. The maximum values of  $J$ ,  $K_a$ , and  $K_c$  involved in these transitions were 10, 7, and 9 respectively. These line frequencies were fit to the AS and NS forms of Watson's rotational Hamiltonian in both the  $I^r$  and  $III^r$  representations using a computer program written by Kirshner.<sup>(21)</sup> Conventionally the  $I^r$  (or  $I^l$ ) representation is used for a prolate asymmetric top ( $-1 < \kappa < 0$ ) and the  $III^r$  (or  $III^l$ ) representation for an oblate asymmetric top ( $0 < \kappa < 1$ ). The representation is usually chosen in this way because as  $\kappa$  approaches  $-1$  the off-diagonal matrix elements of the rigid rotor Hamiltonian become



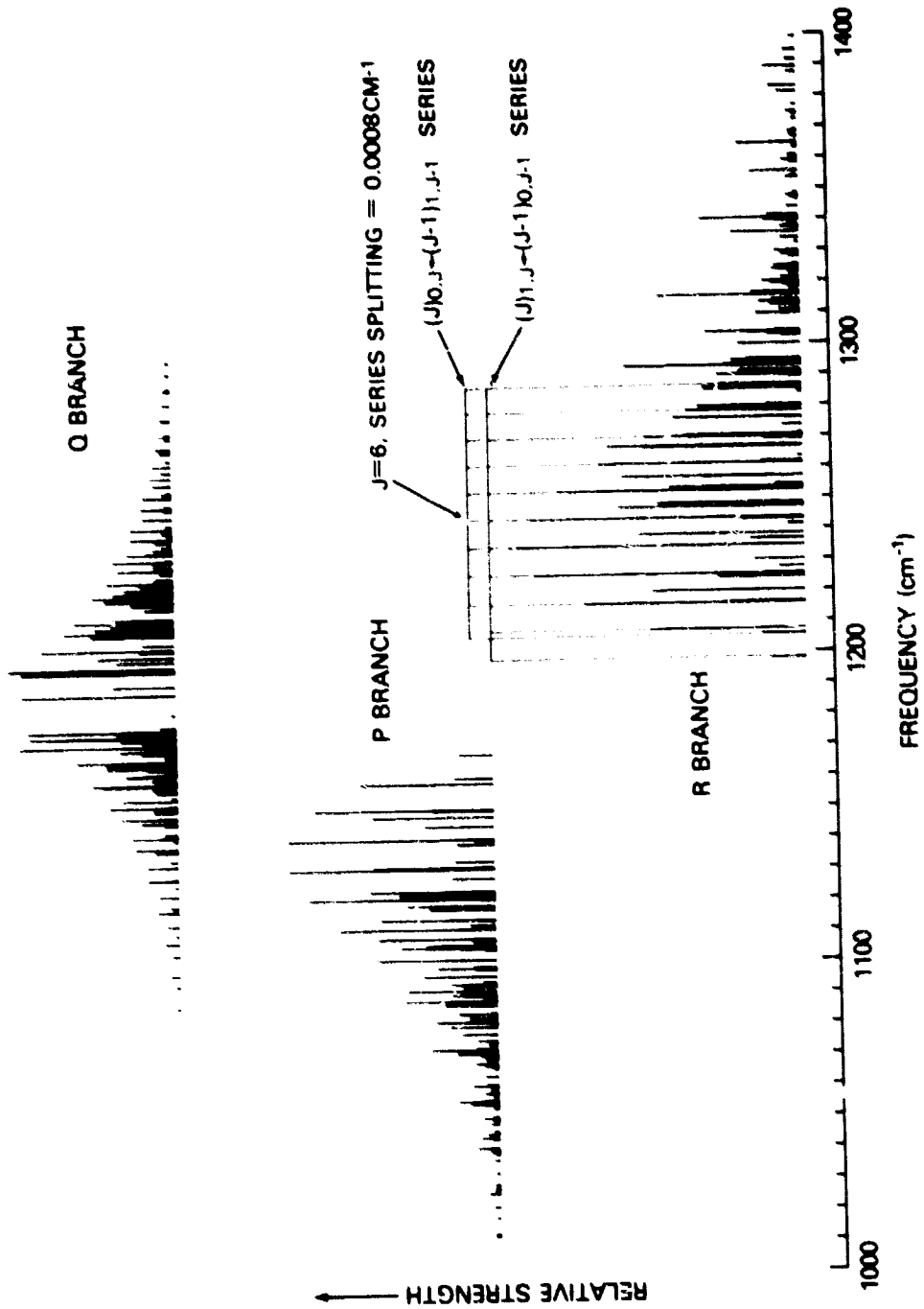


Figure V-2. Stick Spectrum of  $\nu_2$  Band of  $\text{H}_2\text{S}$ , Theoretical Rigid Rotor Strengths Used in this Plot

very small for the I<sup>r</sup> representation, and as  $\kappa$  approaches +1 they become very small for the III<sup>r</sup> representation. Since  $\kappa \approx 0.5$  for H<sub>2</sub>S, the two most recent studies of H<sub>2</sub>S rotational spectra used either the III<sup>r</sup>(17) or the III<sup>r</sup>(16) representations. For a molecule as asymmetric as H<sub>2</sub>S, though, the choice of representation would appear to be somewhat arbitrary. Since a program was available that could fit both reduced Hamiltonians in either representation, fits were made using all four of the Hamiltonian forms AS-I<sup>r</sup>, AS-III<sup>r</sup>, NS-I<sup>r</sup>, and NS-III<sup>r</sup>.

To predict the  $\nu_2$  band transition frequencies one needs both the ground and upper vibrational state Hamiltonian constants. In this study the ground state constants were determined from the very accurate ( $\approx 0.1$  MHz) pure rotational transition frequencies reported by Helminger et al.<sup>(16)</sup> and from the ground state combination differences (GSCD) obtained from the  $\nu_2$  band transitions. A ground state combination difference is the magnitude of the frequency difference between two lines in a vibrational band with common upper states. This frequency difference is equivalent to the frequency of a pure rotational transition between the ground state levels of these two lines. The pure rotational microwave transitions had maximum values of J, K<sub>a</sub>, and K<sub>c</sub> of 9, 7, and 7 respectively. Best fit ground state constants were determined for all four Hamiltonian forms. These ground state constants were then used to calculate the lower state energy levels of the  $\nu_2$  band transitions in order to obtain the upper state energy levels required for the least-squares fit of the upper state Hamiltonian constants.

#### V. B. Least-Squares Fitting of the Rotational Hamiltonian

Least-squares fits of the rotational Hamiltonian to the transition frequencies were performed with a computer program written by Kirschner<sup>(21)</sup> and extended by Hillman.<sup>(55)</sup> The methods used in this program are discussed in detail by Kirshner and will only be summarized here, stressing those points important for the interpretation of our results.

We wish to find the set of statistically significant constants,  $C_i$ , that can most accurately predict the measured frequencies from the Hamiltonian  $H_R = \sum_i C_i Op^i$ , where  $Op^i$  is an

angular momentum operator. Since the calculated frequencies,  $\nu_i^{\text{calc}}$ , are not linear functions of the  $C_i$ , an iterative approach is used in the least-squares fitting routine. This is done by making initial guesses for the  $C_i$  and then finding the set of corrections,  $\delta C_i$ , that best solve the set of linear equations

$$y_i = \sum_k x_{ki} \delta C_k \quad (\text{V-1})$$

where  $y_i = \nu_i^{\text{obs}} - \nu_i^{\text{calc}}$ ,  $x_{ki} = \partial \nu_i^{\text{calc}} / \partial C_k$ , and  $\nu_i^{\text{obs}}$  is the observed frequency of the  $i^{\text{th}}$  transition. In this equation  $i$  runs over the  $N$  transitions and  $k$  over the  $M$  Hamiltonian constants. The best  $\delta C_i$ , in a least-squares sense, are those that minimize the goodness of fit expression,

$$\chi^2 = \sum_{i=1}^N w_i (y_i - \sum_k x_{ki} \delta C_k)^2 \quad (\text{V-2})$$

where  $w_i = 1/\sigma_i^2$  is the weight of the  $i^{\text{th}}$  transition, and  $\sigma_i$  is the experimental error assigned to that transition. When the best  $\delta C_i$  are found, the original values of the  $C_i$  are corrected and another set of corrections to these new  $C_i$  are found. This process is continued until the  $\delta C_i$  satisfy the relation  $|\delta C_i| \leq 10^{-2} \sigma(C_i)$ , where  $\sigma(C_i)$  is the standard deviation for the constant  $C_i$ .

For a vibrational transition where the ground state constants are kept fixed during the fit we have, for example,

$$x_{ki} = \frac{\partial \nu_i^{\text{calc}}}{\partial C_k} = \langle i | \text{Op}^k | i \rangle \quad (\text{V-3})$$

where  $|i\rangle$  is the  $i^{\text{th}}$  upper state asymmetric top eigenfunction which satisfies

$$E_i^{\text{upper}} = \langle i | H_R | i \rangle = \sum_k C_k \langle i | \text{Op}^k | i \rangle. \quad (\text{V-4})$$

For a pure rotational transition we have

$$x_{ki} = \frac{\partial \nu_i^{\text{calc}}}{\partial C_k} = \langle i | \text{Op}^k | i \rangle - \langle i' | \text{Op}^k | i' \rangle \quad (\text{V-5})$$

where the upper state energy is

$$E_i^{\text{upper}} = \langle i | H_R | i \rangle \quad (\text{V-6})$$

and the lower state energy is

$$E_i^{\text{lower}} = \langle i' | H_R | i' \rangle. \quad (\text{V-7})$$

To find the set of  $\delta C_i$  that minimize  $\chi^2$  one usually generates the normal equations from the condition  $\partial \chi^2 / \partial (\delta C_j) = 0$ . The normal equations are

$$\underline{Y} = A \underline{\delta C} \quad (\text{V-8})$$

where

$$Y_k = \sum_j w_j y_j x_{jk}$$

and

$$A_{ki} = \sum_j w_j x_{jk} x_{ji}.$$

The corrections  $\delta C_i$  are found by inverting the normal matrix A to give

$$\underline{\delta C} = A^{-1} \underline{Y}. \quad (\text{V-9})$$

In practice, difficulties can arise in the inversion of A when a large number of  $\delta C_i$  are being determined, because the determinant of A can become very small. This can be due to near linear dependencies in the independent variables (the expectation values of the angular momentum operators) or from a lack of sufficient experimental data to determine some of the  $\delta C_i$  independently of the others. Even in cases where near linear dependencies do not exist round-off errors incurred when inverting the normal matrix can be significant.

To overcome this difficulty Kirshner used an algorithm called ORTHO<sup>(56)</sup> that avoids the need for matrix inversions in the least squares calculation. We originally wanted to find the  $\delta C_i$  that best solve the set of equations V-1, which can be written

$$\underline{y} = X \underline{\delta C}, \quad (\text{V-10})$$

but problems in the inversion of the normal matrix A arise from near linear dependences in the columns of X, or between the vectors  $\underline{x}_j$ . To treat this problem, the set of M vectors  $\underline{x}_j$  can be transformed to an orthonormal set of vectors  $\underline{\epsilon}_j$  using the Gram-Schmidt orthonormalization procedure. The transformation of X is given by  $\underline{\epsilon} = X D$ . We now must solve the set of equations

$$\underline{\chi} = \underline{\epsilon} \underline{\delta C'} \quad (V-11)$$

to get

$$\underline{\delta C'} = \underline{\epsilon}^T \underline{\chi}, \quad (V-12)$$

which can be written this way since the  $\underline{\epsilon}_j$  are orthonormal and therefore  $\underline{\epsilon}^T = \underline{\epsilon}^{-1}$ . The original corrections,  $\underline{\delta C}$ , can easily be shown to be given by

$$\underline{\delta C} = \underline{A} \underline{\epsilon}^T \underline{\chi}. \quad (V-13)$$

The  $\underline{\delta C'}$  obtained this way are the best least-squares estimates for the  $\underline{\delta C'}$ . Because the  $\underline{\epsilon}_j$  vectors are orthonormal, the  $\delta C'_i$  are their Fourier coefficients, which, it can be shown,<sup>(56)</sup> are identical to the best least-squares estimates for the  $\delta C'_i$ . Therefore a matrix inversion is avoided and only the Gram-Schmidt orthonormalization matrix  $\underline{A}$  and the vectors  $\underline{\epsilon}_j$  need be calculated. The weighting of the  $y_j$  can be accomplished by scaling the  $y_j$  and  $x_{kj}$  by  $\sqrt{w_j}$ .

A natural product of the orthonormalization routine in ORTHO is information on the orthogonality of the  $\underline{x}_i$  vectors, which indicates how independently the  $\delta C_i$  can be determined from the measured transition frequencies. The quantity found by ORTHO is the ratio  $GF_i/ENF_i$  where  $ENF_i$  is the magnitude of the vector  $\underline{x}_i$  and  $GF_i$ , called the Gram Factor of the orthonormal vector  $\underline{\epsilon}_i$ , is the magnitude of the component of  $\underline{x}_i$  orthogonal to  $\underline{x}_1, \underline{x}_2, \underline{x}_3, \dots, \underline{x}_{i-1}$ . In our case the vector  $\underline{x}_1$  is associated with the constant  $X$ ,  $\underline{x}_2$  with  $Y$ ,  $\underline{x}_3$  with  $Z$ ,  $\underline{x}_4$  with  $\Delta_j$  or  $D_j$ , and so on in the order the constants are given in equations II-24 for the AS form or II-27 for the NS form. A small  $GF_i/ENF_i$  ratio indicates a near linear dependence of  $\underline{x}_i$  on the previous  $i - 1$  vectors while a  $GF_i/ENF_i$  ratio close to one means that  $\underline{x}_i$  is nearly linearly independent from the previous vectors. The over-all degree of linear dependence in the fit is given by the Gram Determinant,

$$GMDT = \prod_{i=1}^M (GF_i/ENF_i)^2. \quad (V-14)$$

Quantities determined for each fit were the best fit values for the Hamiltonian coefficients,  $C_i$ ; the standard deviation of the coefficients,  $\sigma(C_i)$ ; the correlation matrix,  $\rho_{ik}$ ; the

calculated frequencies,  $\nu_i^{\text{calc}}$ ; the frequency residuals,  $\nu_i^{\text{obs}} - \nu_i^{\text{calc}}$ ; the standard deviation of the residuals,  $\sigma_R$ ; and the weighted standard deviation of the fit,  $\sigma_F$ . The standard deviation of the residuals, hereafter often referred to as the standard deviation of the fit, is given by

$$\sigma_R = \left( \frac{1}{(N - M)} \sum_{i=1}^N (\nu_i^{\text{calc}} - \nu_i^{\text{obs}})^2 \right)^{1/2}. \quad (\text{V-15})$$

$\sigma_F$ , which will always be referred to as the weighted standard deviation of the fit, is given by

$$\sigma_F = \left( \frac{1}{(N - M)} \sum_{i=1}^N w_i (\nu_i^{\text{obs}} - \nu_i^{\text{calc}})^2 \right)^{1/2}, \quad (\text{V-16})$$

and for a perfect fit should equal one. For more rigorous definitions of the above quantities see Kirshner<sup>(21)</sup> or the book by Hamilton.<sup>(57)</sup>

In order to obtain the best least-squares fit for a given data set and Hamiltonian, the set of constants (and their associated operators) included in the Hamiltonian were varied until all statistically significant constants ( $C_i > 2\sigma(C_i)$ ) were used, and hopefully the standard deviation of the residuals became approximately equal to the average experimental error. Generally, quite a number of fits (>10), using different combinations of constants in the Hamiltonian, had to be made until it was clear that the standard deviation of the residuals could not be lowered by adding another term in the Hamiltonian that would in turn be statistically significant.

#### V. C. Results of Least-Squares Fits for the Rotational Constants of the $\nu_2$ Band

The standard deviations of the residuals for the best ground and upper state fits are given in Table V-1. Also included in this table are the standard deviations for fits that only included terms in the Hamiltonian up to second, fourth, and sixth power in angular momentum. The fitting program used here contains all Hamiltonian terms up to eighth power for the AS form but does not contain the off-diagonal eighth power terms for the NS Hamiltonian. The program was not modified to include the eighth order off diagonal terms in the NS Hamiltonian because good fits of the data were obtained with the AS-IF Hamiltonian. No eighth order terms were required for any of the upper state fits.

Table V-1  
Standard Deviation of Ground and Upper State Fits

Maximum Power of Angular Momentum in Hamiltonian	Hamiltonian Form		
	AS-I <sup>F</sup>	AS-III <sup>F</sup>	NS-I <sup>F</sup> NS-III <sup>F</sup>
(a) Ground State (MHz)			
2	9622	9622	9622
4	171	2198	172
(c) 6	1.96, 88	136, 3241	2.91, 92
(c,d) 8	0.15, 84	14.6, 2572	0.49, 84
(d) 8 (e) $\sigma_F =$	0.84	57	2.2
(b) $\nu_2 = 1$ Excited State ( $\text{cm}^{-1}$ )			
2	0.74	0.74	0.74
4	0.010	0.211	0.011
6	0.0018	0.170	0.0018
6 (e) $\sigma_F =$	0.96	130	0.94

(a) 39 microwave lines fit with average expt. error = 0.17 MHz, 51 GSCD fit with average expt. error = 75 MHz; if only one number is given it is the standard deviation of the microwave transitions in MHz.

(b) 126 infrared lines fit with average expt. error = 0.0016  $\text{cm}^{-1}$ , standard deviations given in  $\text{cm}^{-1}$  units.

(c) The two numbers given are the standard deviations of the microwave transitions and GSCD respectively, both in MHz.

(d) Results for best ground state fits, not all eight power coefficients are necessarily used in these fits - see Tables V-2 to V-5.

(e)  $\sigma_F =$  weighted standard deviation of the fit and is unitless.

In Tables V-2 through V-9 the best fit molecular constants for all four Hamiltonian forms for both the ground state and the first excited state of the  $\nu_2$  vibration are given. The microwave transitions were weighted using the uncertainties in their frequencies given by Helminger et. al.<sup>(58)</sup> The weights for the GSCD and the infrared transitions were determined from the experimental errors given in Table IV-4 for the infrared frequencies. The errors quoted for the molecular constants equal twice their standard deviations, which corresponds to 95% confidence intervals. From Table V-1 we see that fits with standard deviations comparable to the experimental errors were obtained for the ground state with the AS-I<sup>r</sup> Hamiltonian and for the upper vibrational state with the AS-I<sup>r</sup>, NS-I<sup>r</sup>, and NS-III<sup>r</sup> Hamiltonians. The weighted standard deviations of the fit for these three upper state Hamiltonian forms were all close to one. It is not surprising that the microwave frequencies could not be fit to the experimental accuracy of about 0.2 MHz with the NS-I<sup>r</sup> and NS-III<sup>r</sup> Hamiltonian forms since they did not contain any eighth order off-diagonal terms. These terms had to be included in the AS-I<sup>r</sup> Hamiltonian to get a fit comparable to the accuracy of the data. If the Hamiltonian is truncated to sixth order, the NS-I<sup>r</sup> and NS-III<sup>r</sup> forms fit the microwave data as well as the AS-I<sup>r</sup> form, so there appears to be no fundamental inaccuracy in the NS form Hamiltonians.

It was very surprising though, that the fits using the AS-III<sup>r</sup> form had such large standard deviations. When all four forms are truncated to fourth power, the standard deviation of the residuals is about 13 times greater for the ground state AS-III<sup>r</sup> Hamiltonian and about 21 times greater for the upper state AS-III<sup>r</sup> Hamiltonian than for the other three ground and upper state Hamiltonian forms. When the Hamiltonians are extended to sixth power the standard deviation of the AS-III<sup>r</sup> form fit is greater than the standard deviations for the other three forms by a factor of 68 for the ground state and 94 for the upper state. The best eighth order ground state fit using the AS-III<sup>r</sup> form has a standard deviation about 100 times larger than the experimental accuracy of the microwave data. For the upper state fit, where only terms up to sixth order were found to be statistically significant, the standard deviation of AS-III<sup>r</sup> form fit was again about 100 times larger than the accuracy of the infrared frequencies. As would be expected, the standard deviations of the AS-III<sup>r</sup> Hamiltonian constants



Table V-2

Molecular Constants for Ground State, AS Form, I<sup>r</sup> Representation

	Constant (MHz)	2 $\sigma$ (MHz)
A <sup>AS</sup>	310590.038	0.032
B <sup>AS</sup>	270357.131	0.038
C <sup>AS</sup>	141825.442	0.030
$\Delta_J$	19.5708	0.0025
$\Delta_{JK}$	-68.3542	0.0089
$\Delta_K$	111.0269	0.0086
$\delta_J$	8.8627	0.0015
$\delta_K$	-3.9769	0.0052
H <sub>J</sub> x 10 <sup>3</sup>	8.038	0.061
H <sub>JK</sub> "	-45.17	0.25
H <sub>KJ</sub> "	35.55	0.84
H <sub>K</sub> "	43.37	0.88
h <sub>J</sub> "	-4.159	0.051
h <sub>JK</sub> "	-14.71	0.13
h <sub>K</sub> "	36.96	0.34
L <sub>JK</sub> x 10 <sup>6</sup>	71	10
L <sub>KKJ</sub> "	-108	13
ℓ <sub>J</sub> "	-3.29	0.34
ℓ <sub>JK</sub> "	35.35	0.83
ℓ <sub>KJ</sub> "	-93.2	4.1
ℓ <sub>K</sub> "	31.2	2.1

Standard Deviation of Microwave Transitions = 0.15 MHz  
 Standard Deviation of GSCD = 84 MHz

Table V-3

Molecular Constants for Ground State, AS Form, III<sup>F</sup> Representation

	Constant (MHz)	2 $\sigma$ (MHz)
A <sup>AS</sup>	310192.7	2.4
B <sup>AS</sup>	270875.0	2.2
C <sup>AS</sup>	141706.2	2.1
$\Delta_J$	50.51	0.30
$\Delta_{JK}$	-160.79	0.30
$\Delta_K$	113.07	0.41
$\delta_J$	6.056	0.024
$\delta_K$	-256.63	0.40
H <sub>J</sub> x 10 <sup>3</sup>	99	13
H <sub>JK</sub> "	-351	24
H <sub>KJ</sub> "	675	48
H <sub>K</sub> "	-399	30
h <sub>J</sub> "	4.31	0.94
h <sub>JK</sub> "	-170	16
h <sub>K</sub> "	-2003	60
L <sub>J</sub> x 10 <sup>6</sup>	-1558	182
L <sub>JJK</sub> "	1260	132
l <sub>J</sub> "	24.1	8.0
l <sub>KJ</sub> "	-6622	1600
l <sub>K</sub> "	24948	2400

Standard Deviation of Microwave Transitions = 14.6 MHz

Standard Deviation of GSCD = 2572 MHz

Table V-4

Molecular Constants for Ground State, NS Form, I<sup>r</sup> Representation

		Constant (MHz)	2 $\sigma$ (MHz)
A <sup>NS</sup>		310583.521	0.084
B <sup>NS</sup>		270367.70	0.12
C <sup>NS</sup>		141820.05	0.077
D <sub>J</sub>		20.8654	0.0073
D <sub>JK</sub>		-76.239	0.011
D <sub>K</sub>		117.717	0.016
$\delta_1$		-8.8658	0.0044
$\delta_2$		0.6433	0.0013
H' <sub>J</sub>	x 10 <sup>3</sup>	10.33	0.13
H' <sub>JK</sub>	"	-90.01	0.33
H' <sub>KJ</sub>	"	154.0	1.1
H' <sub>K</sub>	"	-33.1	1.4
h <sub>1</sub>	"	2.83	0.13
h <sub>2</sub>	"	-1.014	0.032
h <sub>3</sub>	"	1.187	0.026
L' <sub>J</sub>	x 10 <sup>6</sup>	-6.9	2.1
L' <sub>JJK</sub>	"	62.9	5.9
L' <sub>JK</sub>	"	-196	22
L' <sub>KKJ</sub>	"	282	21
L' <sub>K</sub>	"	-175.0	9.1

Standard Deviation of Microwave Transitions = 0.49 MHz

Standard Deviation of GSCD = 84 MHz

Table V-5

Molecular Constants for Ground State, ~~MS~~ Form, III<sup>1</sup> Representation

	Constant (MHz)	$2\sigma$ (MHz)
A <sup>NS</sup>	310667.57	0.38
B <sup>NS</sup>	270331.55	0.42
C <sup>NS</sup>	141789.59	0.32
D <sub>J</sub>	33.130	0.031
D <sub>JK</sub>	<del>-59.195</del>	0.021
D <sub>K</sub>	27.831	0.032
$\delta_1$	-6.2617	0.0040
$\delta_2$	-8.3348	0.0018
H' <sub>J</sub> x 10 <sup>3</sup>	13.92	0.58
H' <sub>JK</sub> "	-48.62	0.66
H' <sub>KJ</sub> "	57.9	2.5
H' <sub>K</sub> "	-23.3	2.0
h <sub>1</sub> "	5.185	0.096
h <sub>2</sub> "	6.819	0.066
h <sub>3</sub> "	0.928	0.010

Standard Deviation of Microwave Transitions = 2.09 MHz

Standard Deviation of GSCD = 77 MHz

Table V-6

Molecular Constants for Upper State of  $\nu_2$  Band, AS Form,  
I<sup>r</sup> Representation

	Constant (cm <sup>-1</sup> )	2 $\sigma$ (cm <sup>-1</sup> )
AAS	10.72212	0.00022
BAS	9.22436	0.00014
CAS	4.668866	0.000062
$\Delta_J \times 10^4$	7.559	0.033
$\Delta_{JK}$ "	-27.35	0.14
$\Delta_K$ "	45.56	0.19
$\delta_J$ "	3.457	0.017
$\delta_K$ "	-0.144	0.061
$H_J \times 10^6$	0.377	0.034
$H_{JK}$ "	-1.90	0.18
$H_{KJ}$ "	1.16	0.34
$H_K$ "	2.36	0.26
$h_J$ "	0.158	0.016
$h_{JK}$ "	-0.428	0.082
$h_K$ "	1.756	0.080
$\nu_0$	1182.57696	0.00043

Standard Deviation of Residuals = 0.0018 cm<sup>-1</sup>

Table V-7

Molecular Constants for Upper State of  $\nu_2$  Band, AS Form, III<sup>F</sup>  
Representation

	Constant (cm <sup>-1</sup> )	2 $\sigma$ (cm <sup>-1</sup> )
AAS	10.696	0.012
BAS	9.268	0.011
CAS	4.6445	0.0090
$\Delta_J$ x 10 <sup>4</sup>	25.9	3.2
$\Delta_{JK}$ "	-89	11
$\Delta_K$ "	49.6	8.2
* $\delta_J$ "	0	—
$\delta_K$ "	-136	24
$H_J$ x 10 <sup>6</sup>	6.9	2.1
* $H_{JK}$ "	0	—
$H_{KJ}$ "	-119	22
$H_K$ "	97	21
* $h_J$ "	0	—
$h_{JK}$ "	-76	21
$h_K$ "	-171	41
$\nu_0$	1182.583	0.057

\*These constants were not statistically significant when included in the fit and were set equal to zero in the fit for the constants given above.

Standard Deviation of Residuals = 0.170 cm<sup>-1</sup>.

Table V-8

Molecular Constants for Upper State of  $\nu_2$  Band, NS Form, I<sup>F</sup> Representation

	Constant (cm <sup>-1</sup> )	2 $\sigma$ (cm <sup>-1</sup> )
A <sup>NS</sup>	10.72208	0.00019
B <sup>NS</sup>	9.22444	0.00013
C <sup>NS</sup>	4.668764	0.000062
D <sub>J</sub> x 10 <sup>4</sup>	7.633	0.030
D <sub>JK</sub> x "	-27.96	0.17
D <sub>K</sub> x "	46.17	0.20
$\delta_1$ x "	-3.480	0.016
$\delta_2$ x "	0.0524	0.0084
H' <sub>J</sub> x 10 <sup>6</sup>	0.368	0.030
H' <sub>JK</sub> x "	-3.35	0.22
H' <sub>KJ</sub> x "	5.67	0.42
H' <sub>K</sub> x "	-0.62	0.34
h <sub>1</sub> x "	0.138	0.015
h <sub>2</sub> x "	-0.028	0.011
h <sub>3</sub> x "	0.0539	0.0020
$\nu_0$	1182.57703	0.00042

Standard Deviation of Residuals = 0.0018 cm<sup>-1</sup>

Table V-9

Molecular Constants for Upper State of  $\nu_2$  Band, NS Form, III<sup>f</sup> Representation

	Constant (cm <sup>-1</sup> )	2 $\sigma$ (cm <sup>-1</sup> )
A <sup>NS</sup>	10.72538	0.00019
B <sup>NS</sup>	9.22311	0.00013
C <sup>NS</sup>	4.667511	0.000058
D <sub>J</sub> x 10 <sup>4</sup>	13.594	0.036
D <sub>JK</sub> x "	-25.805	0.072
D <sub>K</sub> x "	12.814	0.058
$\delta_1$ x "	-2.842	0.040
$\delta_2$ x "	-3.292	0.015
H' <sub>J</sub> x 10 <sup>6</sup>	0.725	0.040
H' <sub>JK</sub> x "	-2.65	0.10
H' <sub>KJ</sub> x "	3.26	0.12
H' <sub>K</sub> x "	-1.345	0.048
h <sub>1</sub> x "	0.291	0.052
h <sub>2</sub> x "	0.326	0.028
h <sub>3</sub> x "	0.0477	0.0056
$\nu_0$	1182.57694	0.00041

Standard Deviation of Residuals = 0.0018 cm<sup>-1</sup>



are much larger than those for the other Hamiltonians. Also, the off-diagonal quartic constants and all higher order constants in the AS-III<sup>r</sup> form are, on the average, larger than the corresponding constants in the other forms. These AS-III<sup>r</sup> fits are so poor that errors or numerical problems in the fitting program were at first suspected to be responsible for these results. The inability to obtain a good upper state fit is also accentuated by using such poor ground state constants to calculate the lower energy levels of the vibrational transitions. Later we will show that these results can be related directly to the unitary transformation used to obtain the AS-III<sup>r</sup> Hamiltonian. Before discussing causes for the poor AS-III<sup>r</sup> form fits some observations on the fitting results in general will be made.

The rigid rotor Hamiltonian was, of course, unable to fit the data even close to the experimental accuracy because of the large centrifugal distortion corrections required for the higher J transitions. The rigid rotor fits were identical for all four Hamiltonian forms, as they should be, since  $H_{\text{rigid}}$  is symmetric in X, Y, and Z and has the same form for both the AS and NS reduced Hamiltonians. When centrifugal distortion terms are included in  $H_{\text{R}}$  the accuracy of the fits varies among the Hamiltonian forms. For a given reduction, variations with representation are expected since the set of operators in each order is not symmetric in X, Y, and Z. Also, the reduction of the Hamiltonian transforms varying amounts of the original coefficients to the new higher order coefficients depending upon the value of  $s_{111}$ , whose value in turn depends upon both the representation and the particular reduction being used. Therefore, if the Hamiltonian is truncated to a given power of angular momentum, it will not fit the data identically for different reductions and representations. If the Hamiltonian included enough higher order terms, the fits for different Hamiltonian forms would be identical since all the effects of lower order coefficients transformed to higher order coefficients would then be contained in the calculation. In our case, except for the AS-III<sup>r</sup> form, the standard deviations of the fits for different forms with the Hamiltonian truncated to a given order are about the same. This indicates that the effects of the unitary transformations performed on the original Hamiltonian for these three reduced forms are very similar.

The ground state Hamiltonians were fit using both the microwave transitions alone and this data combined with the ground state combination differences from the  $\nu_2$  band. The GSCD had very little effect on the eighth order fits, usually changing constants obtained from a fit to only the microwave data by less than their standard deviations. This was due to the low weights assigned to the GSCD compared to the microwave transitions and because the  $J$ ,  $K_a$ , and  $K_c$  values of the GSCD were about the same as those for the microwave transitions. In fact, the 51 GSCD derived from the  $\nu_2$  band contained only eleven energy levels not already present in the microwave data. The microwave pure rotational frequencies are about 500 times more accurate than the GSCD and were therefore weighted a factor of  $(500)^2 = 2.5 \times 10^5$  times heavier than the GSCD. As seen in Table V-1 the standard deviations of the residuals for the GSCD are about equal to their experimental uncertainty, except for the AS-1<sup>1</sup> Hamiltonian. This means that the microwave measurements and the  $\nu_2$  band GSCD are consistent with each other to at least the accuracy of the GSCD.

The weighted standard deviations of the fit are greater than one, as expected, for all the best ground state fits except the AS-1<sup>1</sup> form. When both the microwave transitions and the GSCD are used in the fit of this Hamiltonian form the weighted standard deviation of the fit is 0.84. This figure is somewhat misleading since it is dominated by the residuals of the GSCD, which contribute very little to the determination of the ground state constants. If a fit is performed with the AS-1<sup>1</sup> form using only the microwave transitions the weighted standard deviation of the fit is reduced to 0.45. Therefore, the fit is "better" than it really should be considering the quality of the data. Since the microwave data set contains only 39 transitions, which are used to determine 21 statistically significant rotational constants, there are only  $N - M = 18$  degrees of freedom in the fit. This small weighted standard deviation of the fit coupled with so few degrees of freedom suggests that the fit for the higher order constants is somewhat parametric in nature. This is probably also true when the GSCD are added to the data set, since they are weighted so lightly and affect the constants so little.

Still, including the higher order statistically significant constants in the fit is believed to be reasonable since they provide corrections to the energy levels that cannot be handled by

the lower order terms in the Hamiltonian. If these corrections are left out of the Hamiltonian, the fitting process will minimize the standard deviation by trying to fit the higher order behavior of the Hamiltonian with lower order terms. This will lead to less accurate lower order constants than if the higher order behavior of the Hamiltonian is handled by these higher order constants, even if the result is a parametric type fit yielding values for the higher order constants that do not have physical significance. These comments should be kept in mind when interpreting the standard deviations of the constants obtained in these fits. To improve the molecular constants given here any further, transitions with higher values of  $J$  and  $K_a$  must be included in the fits.

The correlation tables for the ground and upper state fits are given in Appendix B. As is usually the case for fits to a large number of Hamiltonian constants, there are a number of high correlations between constants. The best ground state fit, which used the AS- $I^F$  Hamiltonian, had a total of 15 correlations with  $|\rho_{ij}| > 0.9$ , ranging in magnitude from 0.902 to 0.986, with an average value of 0.94. There were fewer high correlations among the upper state constants. The AS- $I^F$  form had only 3 correlations between upper state constants with  $|\rho_{ij}| > 0.9$ , and none of the forms had more than 5 of these high correlations. The AS- $I^F$  form ground state had 11 high correlations among the sixth and lower order constants compared to 3 high correlations among all the upper state constants. The upper state probably has fewer high correlations because more transitions were used in the fit for this state than for the ground state, making it easier to determine all the upper state constants independently. Some high correlations are also expected due to the approximate validity of the planarity relations among the quartic and sextic constants.

Comparisons of our AS- $III^F$  form ground state fits to others will be made in the next section. The only other fit of the  $H_2S$  microwave data not using the AS- $III^F$  form was by Gillis and Edwards<sup>(17)</sup>, who used Typke's Hamiltonian to sixth order in the  $III^F$  representation. They included both the microwave data and GSCD from several vibrational bands in their fit to obtain the constants given in Table V-10. As previously discussed, Typke's Hamiltonian is very similar to Watson's NS reduced form. The main differences between them will be

Table V-10

Molecular Constants for Ground State, Typke's Hamiltonian, III<sup>F</sup> Representation –  
From Gillis and Edwards<sup>(17)</sup>

	Constant (MHz)	6 $\sigma$ (MHz)
A'	310630.0	9.3
B'	270292.9	8.7
C'	141837.8	3.9
D' <sub>J</sub>	32.98	0.24
D' <sub>JK</sub>	-58.92	0.39
D' <sub>K</sub>	27.79	0.24
$\delta'_J$	-6.25	0.29
R <sub>6</sub>	8.33	0.21
H' <sub>J</sub> x 10 <sup>3</sup>	12.7	2.8
H' <sub>JK</sub> "	-46.0	7.8
H' <sub>KJ</sub> "	56	10
H' <sub>K</sub> "	-22.6	4.5
H' <sub>5</sub> "	9.7	3.9
H' <sub>6</sub> "	26.5	4.8
H' <sub>16</sub> "	7.2	2.1

Standard Deviation of Microwave Transitions = 3 MHz

Standard Deviation of GSCD = 90 MHz

noticeable in high order (sixth and greater) off-diagonal constants, as can be seen by comparing our NS-III<sup>r</sup> form ground state constants in Table V-5 to their constants. The standard deviations of 3 MHz for the microwave data and 90 MHz for the GSCD obtained by Gillis and Edwards are very similar to our values of 2.1 MHz and 77 MHz for these quantities using the NS-III<sup>r</sup> form Hamiltonian.

We conclude that the best rotational constants for both the ground and upper state of the  $\nu_2$  band of H<sub>2</sub>S are those associated with the AS-I<sup>r</sup> Hamiltonians. The observed  $\nu_2$  band transition frequencies minus the frequencies calculated with this Hamiltonian are given in Table IV-4. The AS-I<sup>r</sup> form ground and upper state constants given in Tables V-2 and V-6 were used to calculate these transition frequencies. Even though three of the upper state Hamiltonian forms could fit the infrared data to experimental accuracies, the AS-I<sup>r</sup> form constants should be more accurate since this form had the best ground state constants. The AS-III<sup>r</sup> Hamiltonian, though, was found to produce fits 10 to 100 times worse than the other three forms. Since this form was used by Helminger et. al. in the original fit of the microwave frequencies and because the III<sup>r</sup> (or III<sup>l</sup>) representation is considered to be the natural representation to use for H<sub>2</sub>S, it is important to understand why this Hamiltonian produced such poor results. The following section will discuss the AS-III<sup>r</sup> fits in detail and the cause for their poor behavior.

#### V. D. Characteristics of the AS-III<sup>r</sup> Hamiltonian

In this section, our results for the AS-III<sup>r</sup> form ground state fits will be compared to those of Helminger et al.<sup>(16)</sup> and Gillis and Edwards.<sup>(17)</sup> to see if they are consistent in order to help rule out the possibility that program errors are responsible for our poor AS-III<sup>r</sup> fits. Then the determinable quadratic and quartic constants for all four Hamiltonian forms will be compared to search for any obvious errors in the AS-III<sup>r</sup> results. We will also show that the AS-III<sup>r</sup> determinable constants are converging to their correct values (taken to be the determinable constants for the AS-I<sup>r</sup> Hamiltonian) as higher order terms are added to the Hamiltonian. Further evidence will then be given to support the conclusion that the poor

performance of the AS-III<sup>r</sup> Hamiltonian is due to its very slow convergence. This will include a quantitative study of the unitary transformation that produces the AS-III<sup>r</sup> Hamiltonian.

Helming et. al. fit the AS-III<sup>l</sup> Hamiltonian to the 39 microwave transitions with a standard deviation of 0.38 MHz. They used a total of 24 constants in the Hamiltonian, including 5 tenth order ones, which are given in Table V-11. See reference (16) for the definitions of the tenth order constants given in this table. As expected, their eighth and lower order constants had standard deviations somewhat lower than ours for the AS-III<sup>r</sup> form, but much larger than the standard deviations of our AS-I<sup>r</sup> form constants. Since the standard deviations of our fits to the AS-III<sup>r</sup> form improve rapidly as higher order terms are added, our results appear consistent with those of Helming et. al.

Gillis and Edwards also fit the 39 microwave transitions along with a large number of GSCD from several vibrational bands to the AS-III<sup>r</sup> Hamiltonian. The constants from their fit are given in Table V-12. Their fit had a standard deviation of 180 MHz for the microwave data and 330 MHz for the GSCD when using sixth order terms and lower in the Hamiltonian. This can be compared to our standard deviations of 136 MHz and 3241 MHz for the microwave data and GSCD respectively for the AS-III<sup>r</sup> Hamiltonian truncated at sixth order. Gillis and Edward's GSCD had a much lower standard deviation because they were weighted only 60 times lighter than the microwave transitions, while ours were weighted  $2.5 \times 10^5$  times lighter than the microwave data. Gillis and Edwards weighted their GSCD about 1000 times heavier than the experimental accuracy would suggest because they fit so poorly when weighted properly. These heavier weights resulted in a better fit to the GSCD but at the same time led to a poorer fit to the microwave data. Therefore it is not surprising that their GSCD had a lower standard deviation than ours and their microwave transitions a higher standard deviation. This arbitrary weighting scheme, while improving the fit to the GSCD, still results in a standard deviation for the microwave data 100 times worse than the experimental error. This highly unsatisfactory situation, resulting from their weighting scheme, indicates that a different approach should be taken to either improve the fit or understand

Table V-11

Molecular Constants for Ground State, AS Form, III<sup>R</sup> Representation – From  
Helminger et. al.<sup>(16)</sup>

	Constant (MHz)	2 $\sigma$ (MHz)
A <sup>AS</sup>	310182.24	0.60
B <sup>AS</sup>	270844.05	0.51
C <sup>AS</sup>	141705.88	0.51
$\Delta_J$	49.851	0.038
$\Delta_{\zeta\Pi}$	-159.696	0.069
$\Delta_K$	111.851	0.068
$\delta_J$	-6.0191	0.0050
$\delta_K$	262.17	0.21
H <sub>J</sub> x 10 <sup>3</sup>	28.13	1.05
H <sub>JK</sub> "	-228.3	2.7
H <sub>KJ</sub> "	459	16
H <sub>K</sub> "	-276	14
h <sub>J</sub> "	-5.841	0.081
h <sub>JK</sub> "	242.8	5.2
h <sub>K</sub> "	287.0	39
L <sub>KKJ</sub> x 10 <sup>6</sup>	2199	1190
L <sub>K</sub> "	-2343	1260
ℓ <sub>KJ</sub> "	-5327	990
ℓ <sub>K</sub> "	-41648	1900
P <sub>KJ</sub> x 10 <sup>6</sup>	-304	70
P <sub>KKJ</sub> "	803	180
P <sub>K</sub> "	-515	114
P <sub>JK</sub> "	-12.3	5.2
P <sub>KKJ</sub> "	130	13

Standard Deviation of Microwave Transitions = 0.38 MHz

Table V-12

Molecular Constants for Ground State, AS Form, III<sup>F</sup> Representation – From  
Gillis and Edwards<sup>(17)</sup>

	Constant (MHz)	6 $\sigma$ (MHz)
A <sub>AS</sub>	310172	48
B <sub>AS</sub>	270826	42
C <sub>AS</sub>	141672	23
$\Delta_J$	48.6	1.1
$\Delta_{JK}$	-161.6	3.3
$\Delta_K$	115.8	2.5
$\delta_J$	5.6	1.0
$\delta_K$	-241.3	1.5
H <sub>J</sub> x 10 <sup>3</sup>	17	14
H <sub>JK</sub> "	-708	78
H <sub>KJ</sub> "	2042	130
H <sub>K</sub> "	-1357	66
h <sub>J</sub> "	7.3	6.0
h <sub>JK</sub> "	-298	57
h <sub>K</sub> "	305	63

Standard Deviation of Microwave Transitions = 180 MHz

Standard Deviation of GSCD = 330 MHz



its behavior. Since the other Hamiltonian forms can fit the GSCD so much better than the AS-III<sup>F</sup> form while using the proper weights, a different weighting scheme for this Hamiltonian cannot be justified.

A direct comparison of the quadratic and quartic constants obtained for each Hamiltonian form can be made by transforming them into the determinable constants which are, to a good approximation, independent of Hamiltonian form. The relations for the determinable constants in terms of the AS and NS form constants have been derived by Watson<sup>(3)</sup> and are given in Appendix A. The quartic determinable constants were introduced in equation II-18, where they are written in terms of the  $T_{\alpha\beta}$  coefficients. The calculated determinable constants for the best ground and upper state fits are given in Tables V-13 to V-15. Table V-13 gives the upper state determinable constants in  $\text{cm}^{-1}$ , while Table V-15 gives these same constants in MHz so they can be directly compared to the ground state determinable constants given in Table V-13. As expected, the agreement among the determinable constants for the AS-I<sup>F</sup>, NS-I<sup>F</sup>, and NS-III<sup>F</sup> forms is much better than between these constants and the AS-III<sup>F</sup> determinable constants. For the more precise ground state fits the AS-III<sup>F</sup> determinable constants are in much better agreement with the others than for the upper state fits. Since a higher order fit to more accurate data leads to better determinable constants in the AS-III<sup>F</sup> form, it is unlikely that the relatively poor fits using this form are a result of program errors. If the AS-III<sup>F</sup> Hamiltonian converges more slowly than the other Hamiltonian forms, though, this result is understandable.

Also supportive of our conclusion that the AS-III<sup>F</sup> Hamiltonian converges more slowly than the other Hamiltonian forms are the GF/ENF values calculated for each fit performed in this work. Their values, along with the Gram Determinants, are given in Table V-16 for the ground state and in Table V-17 for the upper state fits. The Gram Determinant, which is an over-all measure of the linear dependence of the Hamiltonian terms, is about eleven

Table V-13

## Determinable Constants for Best Ground State Fits

Constant	Hamiltonian Form			
	AS, I <sup>F</sup>	AS, III <sup>F</sup>	NS, I <sup>F</sup>	NS, III <sup>F</sup>
A <sup>D</sup>	310629.18	310635.46	310629.11	310628.83
B <sup>D</sup>	270318.15	270315.98	270318.02	270317.86
C <sup>D</sup>	141806.00	141808.52	141805.85	141805.84
T <sub>aa</sub>	-62.24	-62.80	-62.34	-62.32
T <sub>bb</sub>	-37.30	-38.59	-37.31	-37.28
T <sub>cc</sub>	-1.845	-2.894	-1.847	-1.826
T <sub>1</sub>	9.642	8.662	9.784	9.753
*T <sub>2</sub>	5.683 x 10 <sup>5</sup>	-0.4733 x 10 <sup>5</sup>	5.701 x 10 <sup>5</sup>	5.761 x 10 <sup>5</sup>

\*Units for T<sub>2</sub> are (MHz)<sup>2</sup>, all others are in MHz.

Table V-14

## Determinable Constants for Best Upper State Fits

Constant	Hamiltonian Form			
	AS, I <sup>r</sup>	(a)AS, III <sup>r</sup>	NS, I <sup>r</sup>	NS, II <sup>r</sup>
A <sup>D</sup>	10.72364	10.71948	10.72364	10.72363
B <sup>D</sup>	9.22247	9.23708	9.22250	9.22250
C <sup>D</sup>	4.66831	4.63948	4.66821	4.66825
T <sub>aa</sub> (x 10 <sup>3</sup> )	-2.577	-2.590	-2.585	-2.586
T <sub>bb</sub> (x 10 <sup>3</sup> )	-1.447	-2.590	-1.449	-1.449
T <sub>cc</sub> (x 10 <sup>5</sup> )	-6.450	135.0	-5.687	-6.033
T <sub>1</sub> (x 10 <sup>4</sup> )	4.668	11.3	4.743	4.772
(b)T <sub>2</sub> (x 10 <sup>3</sup> )	1.895	4.916	1.876	1.921

(a) Note that for the AS-III<sup>r</sup> form the quartic constant  $\delta_J = 0$ .

(b) Units for T<sub>2</sub> are (cm<sup>-1</sup>)<sup>2</sup>, all others are in cm<sup>-1</sup>.

(a)Table V-15

## Determinable Constants for Best Upper State Fits

Constant	Hamiltonian Form			
	AS, I <sup>r</sup>	(b)AS, III <sup>r</sup>	NS, I <sup>r</sup>	NS, III <sup>r</sup>
A <sup>D</sup>	321486.7	321362.0	321486.7	321486.4
B <sup>D</sup>	276482.7	276920.7	276483.6	276483.6
C <sup>D</sup>	139952.4	139088.1	139949.4	139950.6
T <sub>aa</sub>	-77.26	-77.65	-77.50	-77.53
T <sub>bb</sub>	-43.38	-77.65	-43.44	-43.44
T <sub>cc</sub>	-1.934	40.47	-1.705	-1.809
T <sub>1</sub>	13.99	33.9	14.22	14.31
(c)T <sub>2</sub>	1.703 x 10 <sup>6</sup>	4.418 x 10 <sup>6</sup>	1.686 x 10 <sup>6</sup>	1.727 x 10 <sup>6</sup>

(a)This table is identical to Table V-14, except that the constants in this table are given in MHz.

(b)Note that for the AS-III<sup>r</sup> form the quartic constant  $\delta_J = 0$ .

(c)Units for T<sub>2</sub> are in (MHz)<sup>2</sup>, all others are in MHz.

Table V-16

## GF/ENF Factors Best Ground State Fits

AS Form Constant	AS, I <sup>r</sup>	AS, III <sup>r</sup>	NS, I <sup>r</sup>	NS, III <sup>r</sup>	NS Form Constant
$\chi^{AS}$	1.0	1.0	1.0	1.0	$\chi^{NS}$
$\gamma^{AS}$	0.38	1.0	0.38	0.93	$\gamma^{NS}$
$z^{AS}$	0.32	0.022	0.32	0.13	$z^{NS}$
$\Delta_J$	0.36	0.36	0.35	0.36	$D_J$
$\Delta_{JK}$	0.49	0.050	0.49	0.041	$D_{JK}$
$\Delta_K$	0.20	0.059	0.20	0.059	$D_K$
$\delta_J$	0.060	0.021	0.060	0.39	$\delta_1$
$\delta_K$	0.23	0.021	0.67	0.48	$\delta_2$
$H_J$	0.057	0.052	0.058	0.057	$H'_J$
$H_{JK}$	0.25	0.010	0.25	0.0067	$H'_{JK}$
$H_{KJ}$	0.62	0.0031	0.062	0.0032	$H'_{KJ}$
$H_K$	0.070	0.0016	0.070	0.0016	$H'_K$
$h_J$	0.011	0.30	0.011	0.22	$h_1$
$h_{JK}$	0.013	0.013	0.041	0.13	$h_2$
$h_K$	0.016	0.0030	0.015	0.31	$h_3$
$L_J$		0.0040	0.0026		$L'_J$
$L_{JK}$		0.0017	0.055		$L'_{JK}$
$L_{JK}$	0.070		0.015		$L'_{JK}$
$L_{KKJ}$	0.011		0.0085		$L'_{KKJ}$
$L_K$			0.025		$L'_K$
$\rho_J$	0.0036	0.099			$\rho_1$
$\rho_{JK}$	0.0077				$\rho_2$
$\rho_{KJ}$	0.0080	0.0015			$\rho_3$
$\rho_K$	0.075	0.00082			$\rho_4$
GMDT	$1.1 \times 10^{-48}$	$6.6 \times 10^{-66}$	$1.1 \times 10^{-45}$	$1.2 \times 10^{-31}$	

Table V-17

GF/ENF Factors – Best  $\nu_2$  Band Fits

AS Form Constant	AS, I <sup>r</sup>	AS, III <sup>r</sup>	NS, I <sup>r</sup>	NS, III <sup>r</sup>	NS Form Constant
$\nu_0$	1.0	1.0	1.0	1.0	$\nu_0$
X <sup>AS</sup>	0.66	0.62	0.66	0.63	X <sup>NS</sup>
Y <sup>AS</sup>	0.38	0.38	0.38	0.36	Y <sup>NS</sup>
Z <sup>AS</sup>	0.34	0.37	0.34	0.37	Z <sup>NS</sup>
$\Delta_J$	0.064	0.064	0.064	0.064	D <sub>J</sub>
$\Delta_{JK}$	0.13	0.027	0.13	0.027	D <sub>JK</sub>
$\Delta_K$	0.24	0.034	0.24	0.034	D <sub>K</sub>
$\delta_J$	0.031		0.031	0.24	$\delta_1$
$\delta_K$	0.14	0.096	0.10	0.66	$\delta_2$
H <sub>J</sub>	0.027	0.027	0.027	0.027	H' <sub>J</sub>
H <sub>JK</sub>	0.031		0.030	0.0072	H' <sub>JK</sub>
H <sub>KJ</sub>	0.032	0.0076	0.032	0.0034	H' <sub>KJ</sub>
H <sub>K</sub>	0.009	0.0065	0.069	0.0066	H' <sub>K</sub>
h <sub>J</sub>	0.0088		0.0088	0.063	h <sub>1</sub>
h <sub>JK</sub>	0.027	0.053	0.019	0.16	h <sub>2</sub>
h <sub>K</sub>	0.12	0.042	0.23	0.52	h <sub>3</sub>
GMDT	$1.5 \times 10^{-33}$	$2.1 \times 10^{-30}$	$1.3 \times 10^{-33}$	$3.2 \times 10^{-34}$	

orders of magnitude smaller for the AS-III<sup>r</sup> form ground state than for the other Hamiltonian forms.\* The upper state GF/ENF factors are also smaller for the AS-III<sup>r</sup> form, though its Gram Determinant is not smaller since the AS-III<sup>r</sup> form fit contains three less constants than the others. The larger linear dependencies among the AS-III<sup>r</sup> form Hamiltonian terms are consistent with it being a more slowly converging power series with large individual coefficients. It is well known, for example, that a power series approximation using orthogonal polynomials, will have smaller coefficients and will converge more rapidly than one using non-orthogonal polynomials.

The convergence properties of the AS-III<sup>r</sup> form can also be studied by examining the unitary transformation that leads to this form. The possible poor convergence of some reduced Hamiltonians has been previously recognized only for nearly symmetric asymmetric rotors. For the almost symmetric rotors CF<sub>2</sub> ( $\kappa = 0.9798$ ) and SO<sub>2</sub> ( $\kappa = -0.942$ ), Carpenter<sup>(59)</sup> found that the AS form Hamiltonian converged very slowly in the III<sup>r</sup> representation for CF<sub>2</sub> and in the I<sup>r</sup> representation for SO<sub>2</sub>. He then calculated  $s_{111}$ , given in equation II-22, for these different representations and found that the slow convergence of the Hamiltonian was related to a relatively large value of  $s_{111}$ . This is expected for a nearly symmetric prolate or oblate top in the I<sup>r</sup> and III<sup>r</sup> representations, respectively, because  $s_{111}$  in the AS form is proportional to  $1/(Y-X)$ , which becomes very large as  $Y \rightarrow X$  in these particular symmetric top limits. Since the transformed Hamiltonian contains terms like  $s_{111}(X-Z)$  in its quartic coefficients and like  $s_{111}^2(Z-Y)$  and  $s_{111}(T_{yy} - T_{yz})$  in its sextic coefficients we see that, in general, a bigger  $s_{111}$  will transform a larger part of the original lower order coefficients into the new higher order coefficients. This will result in larger transformed coefficients and make the Hamiltonian power series converge more slowly. One would expect this type of behavior, though, to be noticeable only in nearly symmetric asymmetric top molecules.

---

\*The ground state Gram Determinants compared here only included GF/ENF factors for constants up to sixth order so they would be directly comparable to each other.

A similar calculation of  $s_{111}$  was performed here using equations II-22 and II-25 for the AS and NS forms respectively, to see if it is much larger for the AS-III<sup>r</sup> form than for the other three Hamiltonian forms. Unfortunately,  $s_{111}$  cannot be calculated directly from the coefficients in a reduced Hamiltonian unless the planarity conditions for the quartic constants are imposed. Although the quartic planarity relations are not strictly correct, the errors introduced by using them in the calculation of  $s_{111}$  were found to be small compared to the variation of  $s_{111}$  with Hamiltonian form. All the untransformed quartic coefficients, and therefore  $s_{111}$ , can also be approximately calculated from the harmonic molecular force field if it is known. This calculation gives equilibrium distortion constants and not the vibrationally averaged ones observed in practice. For H<sub>2</sub>S, a molecular force field obtained solely from vibrational band centers is available.<sup>(60)</sup> Therefore, the  $s_{111}$  values calculated with this method will contain no input from H<sub>2</sub>S rotational frequencies or from the fitting routines used in this work and can serve as a check on the other calculations of  $s_{111}$ .

To calculate  $s_{111}$  from the coefficients obtained in the least-squares fits, the two planarity relations

$$T_{ac} = \frac{1}{2} A^2 C^2 \left[ \frac{T_{aa}}{A^4} - \frac{T_{bb}}{B^4} + \frac{T_{cc}}{C^4} \right] \quad (V-17)$$

and

$$T_{bc} = \frac{1}{2} B^2 C^2 \left[ -\frac{T_{aa}}{A^4} + \frac{T_{bb}}{B^4} + \frac{T_{cc}}{C^4} \right] \quad (V-18)$$

were used along with the equations for the determinable coefficients  $T_1$  and  $T_2$  given in equation II-18. The planarity relations given above are written in terms of the  $T_{\alpha\beta}$  constants since  $\tau_{aacc} = \tau'_{aacc} = 4 T_{ac}$  and  $\tau_{bbcc} = \tau'_{bbcc} = 4 T_{bc}$ . Note that the third planarity relation for  $\tau_{aabb}$  given in Appendix A cannot be written using the  $T_{\alpha\beta}$  notation because  $\tau_{aabb} = \tau'_{aabb} - 2 \tau_{abab} \neq T_{ab}$ . With the values given for the determinable constants  $T_{aa}$ ,  $T_{bb}$ , and  $T_{cc}$  in Tables V-13 and V-14,  $T_{ac}$  and  $T_{bc}$  can be calculated using the planarity relations. If only  $T_{ac}$  or  $T_{bc}$  is calculated using these relations, the other constant as well as  $T_{ab}$  can be obtained by solving the relations for  $T_1$  and  $T_2$  simultaneously. The procedure used here was to calculate the required coefficients twice, each time using a different planarity relation along with the



equations for  $T_1$  and  $T_2$ . There are a number of additional ways to calculate  $s_{111}$  using these equations, but they should all give roughly the same results, as was tested by using our two different methods for calculating  $s_{111}$ . The determinable constants  $A^D$ ,  $B^D$ , and  $C^D$  were used in equations V-17 and V-18 as (very good) approximations for A, B, and C. The results of these calculations are given in Table V-18 where  $s_{111} - 1$  denotes the  $s_{111}$  value calculated using equation V-17 and the relations for  $T_1$  and  $T_2$ , and  $s_{111} - 2$  denotes the  $s_{111}$  value calculated using equation V-18 and the  $T_1$  and  $T_2$  relations. The best fit values for the quartic distortion constants were used in all cases.

To calculate  $s_{111}$  from the harmonic force field the following relations for the quartic distortion constants derived by Kivelson<sup>(61)</sup> for a planar triatomic molecule were used,

$$-\frac{\tau_{aaaa} R}{A^2} = 2 F_{11}^{-1} + \tan^2 \theta F_{22}^{-1} - 2\sqrt{2} \tan \theta F_{12}^{-1} \quad (V-19)$$

$$-\frac{\tau_{bbbb} R}{B^2} = 2 F_{11}^{-1} + \cot^2 \theta F_{22}^{-1} + 2\sqrt{2} \cot \theta F_{12}^{-1} \quad (V-20)$$

$$-\frac{\tau_{aabb} R}{AB} = 2 F_{11}^{-1} - F_{22}^{-1} + \sqrt{2} (\cot \theta - \tan \theta) F_{12}^{-1} \quad (V-21)$$

$$-\frac{\tau_{abab} R}{AB} = \frac{2 M}{m_x} \left(1 + 2 \frac{m_y}{m_x} \sin^2 \theta\right)^{-2} F_{33}^{-1} \quad (V-22)$$

where

$$R = \frac{r^2 \times 10^{-20}}{2h}$$

$\theta$  is  $\frac{1}{2}$  the bond angle for  $H_2S = 46.07^\circ$ ,  $M =$  atomic weight of  $H_2S = 34$  amu,  $m_y = m_{\text{hydrogen}} = 1$  amu,  $m_x = m_{\text{sulphur}} = 32$  amu, and  $r = H - S$  bond length = 1.3518 Å. The inverse force field matrix  $F^{-1}$  was calculated from a force field matrix given by Cook et. al.<sup>(60)</sup>, which was derived solely from the vibrational band centers of  $H_2S$ . The non-zero elements of these matrices are

Table V-18

 $s_{111}$  Parameter Calculations

Type of Data	Hamiltonian Form	$s_{111-1}$	$s_{111-2}$	$s_{111-FF}$	(c) Standard Deviation of Fit (MHz)
		(x $10^{-6}$ )			
MW	AS (I <sup>r</sup> )	62	70	56	1.96
MW	AS (III <sup>r</sup> )	837	849	729	136
MW	NS (I <sup>r</sup> )	90	82	82	2.91
MW	NS (III <sup>r</sup> )	-24	-17	-17	2.09
(a)MW	AS (III <sup>l</sup> )	864	861	729	
(b)MW	AS (III <sup>r</sup> )	770	812	729	
IR	AS (I <sup>r</sup> )	69	91	53	54
IR	AS (III <sup>r</sup> )	1554	962	661	5100
IR	NS (I <sup>r</sup> )	93	75	75	54
IR	NS (III <sup>r</sup> )	-37	-17	-16	54

(a) From MW fit of Helminger et al.<sup>(16)</sup>

(b) From MW fit of Gillis et al.<sup>(17)</sup>

(c) Standard deviation obtained when Hamiltonians include terms only up to sixth power in angular momentum.

$$\begin{aligned}
F_{11} &= 4.2731 \text{ md/\AA} \\
F_{22} &= 0.4250 \text{ md/\AA} \\
F_{33} &= 4.2960 \text{ md/\AA} \\
F_{12} &= F_{21} = 0.064 \text{ md/\AA}
\end{aligned}
\tag{V-23}$$

and

$$\begin{aligned}
F_{11}^{-1} &= 0.23455 \text{ (md/\AA)}^{-1} \\
F_{22}^{-1} &= 2.3582 \text{ (md/\AA)}^{-1} \\
F_{33}^{-1} &= 0.23278 \text{ (md/\AA)}^{-1} \\
F_{12}^{-1} &= F_{21}^{-1} = -0.03532 \text{ (md/\AA)}^{-1}
\end{aligned}
\tag{V-24}$$

The rest of the required distortion constants were calculated using the planarity relations and the equations given in II-8 relating the  $\tau_{\alpha\alpha\beta\beta}$  constants to the  $\tau'_{\alpha\alpha\beta\beta} = 4 T_{\alpha\beta}$  constants. The values for  $s_{111}$  calculated using the molecular force field are denoted by  $s_{111} - \text{FF}$  in Table V-18.

Another general check on the accuracy of the quartic planarity relations when applied to  $\text{H}_2\text{S}$  was made by evaluating the planarity relations derived by Watson.<sup>(62)</sup> These relations are stated directly in terms of the AS and NS Hamiltonian constants, and are given in Appendix A, equation A-4. They involve four terms, composed of products of quartic and quadratic rotational constants, whose sum should equal zero if true equilibrium constants are used. These relations were evaluated for each of the four Hamiltonian forms in both the ground and upper vibrational states. A measure of the accuracy of these relations is the deviation from zero of the sum of the four terms divided by their average magnitude. Using this measure, the planarity relations were found to be accurate to within 1% to 5% for the ground state constants and 5% to 40% for the upper state constants. These results indicate that any errors in the calculation of  $s_{111}$  due to the planarity relations should be small compared to the variation of  $s_{111}$  with Hamiltonian form observed in Table V-18.

From Table V-18, we see that  $s_{111}$  is about 12 times larger for the AS-III<sup>F</sup> form in the ground state and about 25 times larger for this form in the upper vibrational state than for

the other three Hamiltonian forms. The rather good agreement among the three calculated values for  $s_{111}$  for each form gives us confidence in the methods used for these calculations. Also, since the values for  $s_{111}$  calculated from the distortion constants are always close to those calculated from the molecular force field, it would have been possible to predict the poor performance of the AS-III<sup>r</sup> Hamiltonian in fitting the transition frequencies without performing the least-squares fits. The similarity of these two calculations is also another strong assurance that the AS-III<sup>r</sup> form fitting routine does not contain any program errors or numerical problems. It should also be noted that the values calculated for  $s_{111}$  from the constants of Helminger et. al. and Gillis and Edwards are very close to our value for  $s_{111}$  for the AS-III<sup>r</sup> form. Considering the fact that molecular rotational data is usually only fit to a single, somewhat arbitrarily chosen reduced Hamiltonian, our results show the usefulness of performing a calculation of  $s_{111}$  before choosing a Hamiltonian form for the least-squares fit of the data.  $s_{111}$  - FF was also calculated for the AS and NS forms in the II<sup>r</sup> representation and was found to equal  $-55 \times 10^{-6}$  for the AS form and  $-31 \times 10^{-6}$  for the NS form. Both of these values for  $s_{111}$  are close to those obtained for the AS-I<sup>r</sup>, NS-I<sup>r</sup>, and NS-III<sup>r</sup> Hamiltonians, and therefore fits made using the II<sup>r</sup> representation will probably be no better than those already performed.

To illustrate how much the unitary transformation for the AS-III<sup>r</sup> form can alter the rotational constants, we can evaluate the quartic coefficient  $\tilde{T}_{022}$ , which corresponds to  $-\delta_k$ , and part of the sextic coefficient  $\tilde{\phi}_{060}$ , which corresponds to  $H_k$ . From equation II-21 and the ground state AS-III<sup>r</sup> form constants we have

$$-\delta_k = 257 \text{ MHz} = \tilde{T}_{022} = T_{022} - 2 B_{020} s_{111} = T_{022} + 238 \text{ MHz} \quad (\text{V-25})$$

where the AS-III<sup>r</sup> form values for  $B_{020}$  and  $s_{111}$  have been inserted. Using the formula for  $\tilde{\phi}_{060}$  in Table 2 of Ref. (3) and the value found for  $H_k$  in the AS-III<sup>r</sup> ground state fit we have

$$\begin{aligned} H_k = 0.42 \text{ MHz} &= \tilde{\phi}_{060} = \phi_{060} + 14 B_{020} s_{111}^2 + \text{other terms} \\ &= \phi_{060} - 1.3 \text{ MHz} + \text{other terms} \end{aligned} \quad (\text{V-26})$$

where the AS-III<sup>r</sup> form values for  $B_{020}$  and  $s_{111}$  have again been inserted. We see that the AS-III<sup>r</sup> unitary transformation contributes 238 MHz to  $\delta_k$ , which can be compared to a contribution of only - 13.2 MHz to  $\delta_k$  calculated for the AS-I<sup>r</sup> form unitary transformation. Similarly, the AS-III<sup>r</sup> transformation contributes - 1.3 MHz to  $H_k$  from the  $B_{020} s_{111}^2$  term while the AS-I<sup>r</sup> transformation only contributes 0.0058 MHz to  $H_k$  from this term. We can also calculate  $T_{022}$  from equation V-25 to obtain  $T_{022} = 19$  MHz. Therefore the AS-III<sup>r</sup> unitary transformation changed  $T_{022}$  by more than an order of magnitude, illustrating the poor characteristics of this particular Hamiltonian form. The large contributions to the higher order transformed constants from the original lower order ones for the AS-III<sup>r</sup> form, combined with the already large centrifugal distortion corrections required to accurately calculate the H<sub>2</sub>S rotational energy levels, results in a power series for this reduced Hamiltonian with extremely slow convergence.

It is possible to understand the poor behavior of the AS-III<sup>r</sup> Hamiltonian in a more qualitative manner. Because of the geometry of H<sub>2</sub>S, the rotational constants A and B are sensitive to the value of the bond angle, while C is not. As the bond angle goes to 180°, for example, the A rotational constant diverges. Also, the force constant  $F_{22}$ , which is associated with changes in the bond angle, is very small. Consequently, rotation of the molecule about a and b axes can significantly alter the bond angle and cause large changes in the instantaneous A and B rotational constants. Rotation about the c axis, though, only causes a small amount of bond stretching, which affects A, B, and C very little. Therefore, the centrifugal distortion constants that go with terms in the Hamiltonian containing the operators  $J_a$  and  $J_b$  will be large relative to those constants that go with terms containing only  $J_c$ . For example, from Table V-13, it can be seen that the quartic distortion coefficients  $T_{aa}$  and  $T_{bb}$  are about 25 times larger than  $T_{cc}$ .

If the operators present in the four reduced Hamiltonians used here are examined (see equations II-24 and II-27), a striking difference between the AS-III<sup>r</sup> Hamiltonian and the other three Hamiltonian forms is apparent. To any order, the highest

powers of  $J_a$  and  $J_b$  that ever appear in the AS-III<sup>r</sup> Hamiltonian are  $J_a^2$  and  $J_b^2$ . The other three Hamiltonian forms, though, when expanded to the  $n^{\text{th}}$  power of angular momentum, contain at least one of the operators  $J_a^n$  or  $J_b^n$ , or the product  $J_a^{n/2} J_b^{n/2}$ . Since the operators with the largest distortion coefficients have been dropped from the AS-III<sup>r</sup> Hamiltonian, it is not surprising that it fits the transition frequencies so poorly compared to the other three Hamiltonian forms. As has been shown, the AS-III<sup>r</sup> Hamiltonian must be taken to higher orders of angular momentum than the other three Hamiltonians to make up for its lack of terms with high powers of  $J_a$  and  $J_b$ .

In conclusion, a very satisfactory fit of the measured  $\nu_2$  band frequencies has been made to the AS-I<sup>r</sup> form reduced Hamiltonian for the upper vibrational state. It should be mentioned that the use of the AS-I<sup>r</sup> constants to predict transition frequencies involving states with  $J$  or  $K_a$  greater than about 9 (roughly the maximum value of  $J$  or  $K_a$  used in the least-squares fits) will result in errors higher than those indicated by the statistical uncertainties in these constants. The AS-III<sup>r</sup> reduced Hamiltonian fit the measured frequencies very poorly due to its very slow convergence. This unexpected slow convergence could have been predicted by the large value of the Hamiltonian transformation parameter,  $s_{111}$ , calculated using the molecular force field constants. In most previous studies of asymmetric rotor spectra, a single and somewhat arbitrary choice for the Hamiltonian form has usually been made. Our results, though, illustrate that in some cases, it can be very important to choose the proper Hamiltonian form and representation, even when fitting rotational data for very asymmetric tops.

## CHAPTER VI

### LINE STRENGTHS IN THE $\nu_2$ BAND OF $\text{H}_2\text{S}$ - COMPARISON TO RIGID ROTOR LINE STRENGTHS

In this chapter the results of the  $\text{H}_2\text{S}$  line strength measurements will be discussed and compared to calculated rigid rotor line strengths. Since a number of doublets in the  $\nu_2$  band of  $\text{H}_2\text{S}$  have lines with an intensity of 3 to 1 due to nuclear spin statistics, a partial check of the internal consistency of the measured line strengths will be made by comparing the observed line strength ratios to the known ratio of 3 to 1. Some general observations will also be made on the dependence of the line strength perturbations on  $J$ ,  $K_a$  and  $K_c$ .

The line strength ratios in twelve doublets, all measured at low pressures, were computed for comparison to the expected ratios of 3 to 1. The expected deviation of any of these strength ratios from 3 to 1 due to centrifugal distortion or other causes should be small since the doublets were split by only  $0.01\text{ cm}^{-1}$  to  $0.1\text{ cm}^{-1}$ . The standard deviation of the observed ratios from a 3 to 1 ratio was found to be 1.8%. Since both lines of each doublet were always in the same diode laser scan, any errors in their strengths due to uncertainties in the gas pressure or due to distortion of the lines by the laser lineshape should be the same. Therefore, the experimental errors in the observed line strength ratios were determined solely from the standard deviation of the measurements used to obtain an average line strength for each transition. The average experimental error calculated in this manner for the twelve ratios was 1.8%, the same as the standard deviation of the observed ratios from a 3 to 1 ratio. This indicates that the strengths measured within one laser mode were internally consistent.

The line strengths measured here were compared to calculated rigid rotor line strengths in order to determine the magnitude of the centrifugal distortion perturbations. To calculate the rigid rotor line strengths the total band strength  $S_v^0$ , which is the sum of all the

line strengths in the band, is needed. Since  $S_v^0$  cannot be determined directly from our measured line strengths, the band strength value of  $S_v^0 = 2.17 \text{ cm}^{-1}/\text{atm-cm}$  measured by Emerson and Eggers<sup>(1)</sup> was used for the rigid rotor calculation. In terms of the total band strength, the rigid rotor line strengths are given by

$$S = \frac{S_v^0 \nu g_i e^{-E_i/kT}}{\bar{\nu} Q_R} (1 - e^{-h\nu/kT}) |\langle \varphi_{Zb} \rangle|^2. \quad (\text{VI-1})$$

This equation can be derived from equation II-32 and the definition  $S_v^0$ .  $\bar{\nu}$  is the band center frequency. In this approximation,  $S_v^0$  is proportional to the vibrational part of the dipole moment matrix element, which is given in equation II-40.

The usual approximation was made in equation VI-1 that the partition function  $Q$  can be separated into a rotational part,  $Q_R$  and a vibrational part,  $Q_V$ , which is included in  $S_v^0$ .  $Q_R$  is given approximately by<sup>(63)</sup>

$$Q_R \approx \left( \frac{\pi(kT)^3}{ABC} \right)^{1/2} \quad (\text{VI-2})$$

where  $A, B, C$  are the ground state quadratic rotational constants. The accuracy of equation VI-2 was checked by comparing the value it gives for  $Q_R$  for  $\text{H}_2\text{O}$  to the more accurate value of  $Q_R$  calculated by Camy-Peret and Flaud<sup>(24)</sup> using equation II-33. These two values of  $Q_R$  for  $\text{H}_2\text{O}$  were different by only 2.3%. This uncertainty of about 2% in  $Q_R$  and the quoted uncertainty of 5% in the total band strength were the main contributors to any errors in the rigid rotor line strength calculation.

The lower state energy levels,  $E_i$ , and the direction cosine matrix elements  $\langle \varphi_{Zb} \rangle$  were calculated using a computer program written by Maki.<sup>(54)</sup> This program uses a Watson AS- $I^r$  Hamiltonian to calculate the rotational energy levels and eigenfunctions required to determine these matrix elements. Since only terms up to the sixth power of angular momentum were included in the ground and upper state AS- $I^r$  Hamiltonians for these calculations, our best fit rotational constants for the same ground and upper state Hamiltonians were used here. It should be noted that by using quartic and sextic terms in the rotational



Hamiltonian in this calculation, the average centrifugal distortion within each vibrational state is included in the rotational part of the total wavefunction. The vibrational part of the dipole moment matrix element, though, is kept constant for all the individual line strengths calculated for the band. The final rigid rotor line strengths calculated using equation VI-1 were divided by 0.9502 to correct for the naturally occurring abundance<sup>(53)</sup> of the sulphur 32 isotope. Since Emerson and Eggers made no mention of isotopic impurities in their measurements, we have assumed that their quoted value for  $S_v^0$  includes contributions from all the sulphur isotopes.

The calculated rigid rotor line strengths and the observed line strengths are plotted as a function of frequency in Figure VI-1. The experimental F factors (the ratios of the observed to calculated line strengths) for each line are listed in Table IV-5. Also, the F factors are plotted as a function of frequency in Figure VI-2. The Q branch plots have been separated from the R and P branch plots in this figure for clarity. It should be remembered that only the H<sub>2</sub>S transitions measured with the diode laser spectrometer are shown in these figures. There are a number of other H<sub>2</sub>S absorption lines in the 1080 cm<sup>-1</sup> to 1260 cm<sup>-1</sup> region that were not measured and do not appear in Figures VI-1 and VI-2.

As expected from the low resolution measurements of this band, the R and Q<sup>RP</sup> branch F factors are greater than unity, and the P and Q<sup>PR</sup> branch F factors are almost all less than unity. The F factors range from as low as 0.057 on the P branch side of the band center to as high as 4.71 on the R branch side. The maximum values of J, K<sub>a</sub>, and K<sub>c</sub> observed for the measured transitions were 12, 7, and 10, respectively. It is also evident in Figure VI-1 that in all the branches it is the weaker lines whose strengths differ the most relative to their rigid rotor strengths.

The strong lines in Figure VI-1, whose strengths differ from the rigid rotor line strengths by only 10% to 20%, belong to the four sub-bands (J)<sub>0,J</sub> - (J-1)<sub>1,J-1</sub>, (J-1)<sub>1,J-1</sub> - (J)<sub>0,J</sub>, (J)<sub>1,J</sub> - (J-1)<sub>0,J-1</sub>, and (J-1)<sub>0,J-1</sub> - (J)<sub>1,J</sub>. The rotational energy levels involved in these transitions always have one state with K<sub>a</sub> = 1 and the other with K<sub>a</sub> = 0. The K<sub>c</sub> values are always equal to J for each energy level, the maximum possible value allowed. This

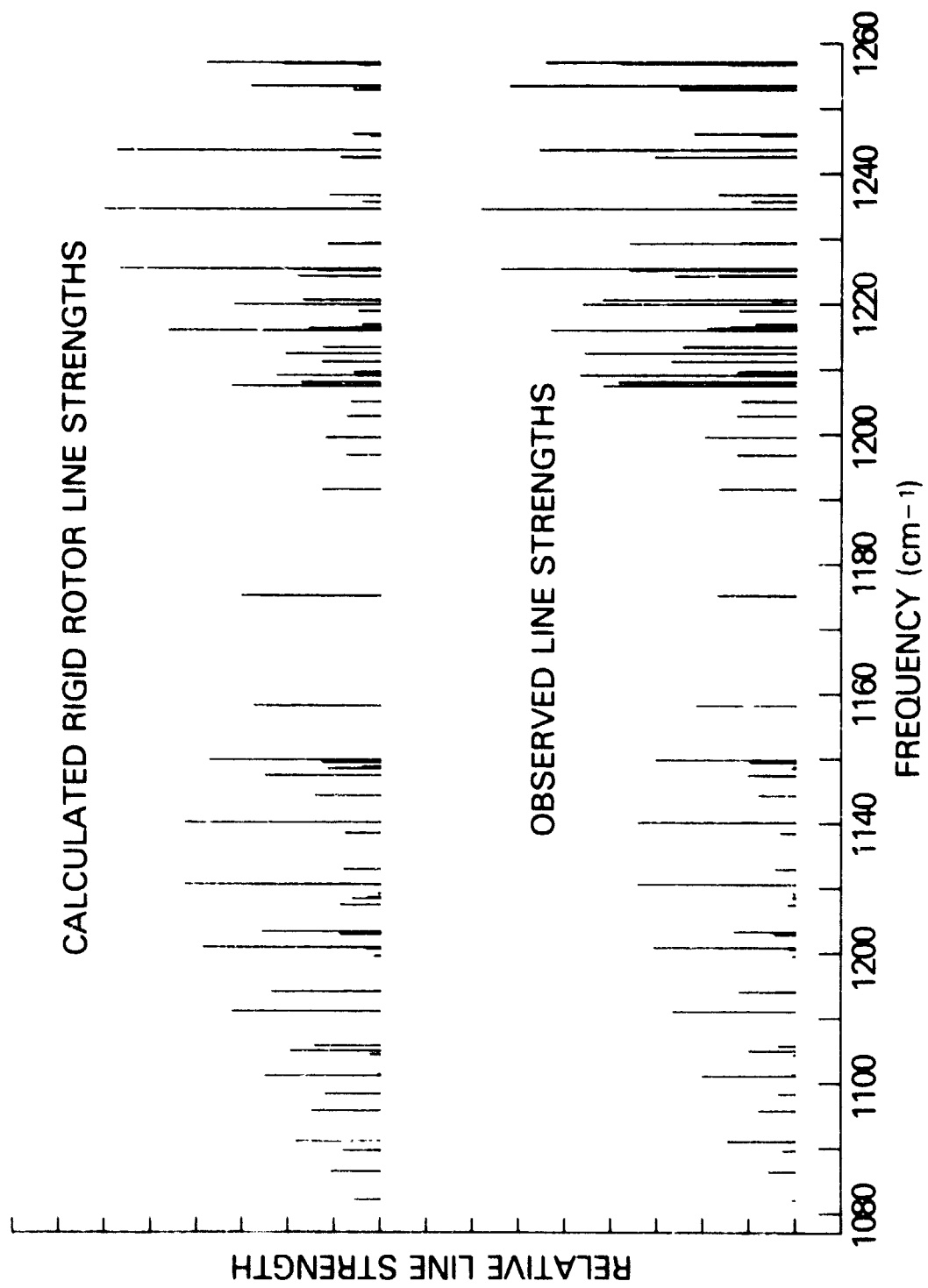


Figure VI-1. Stick Spectrum of Observed Line Strengths and Rigid Rotor Line Strengths

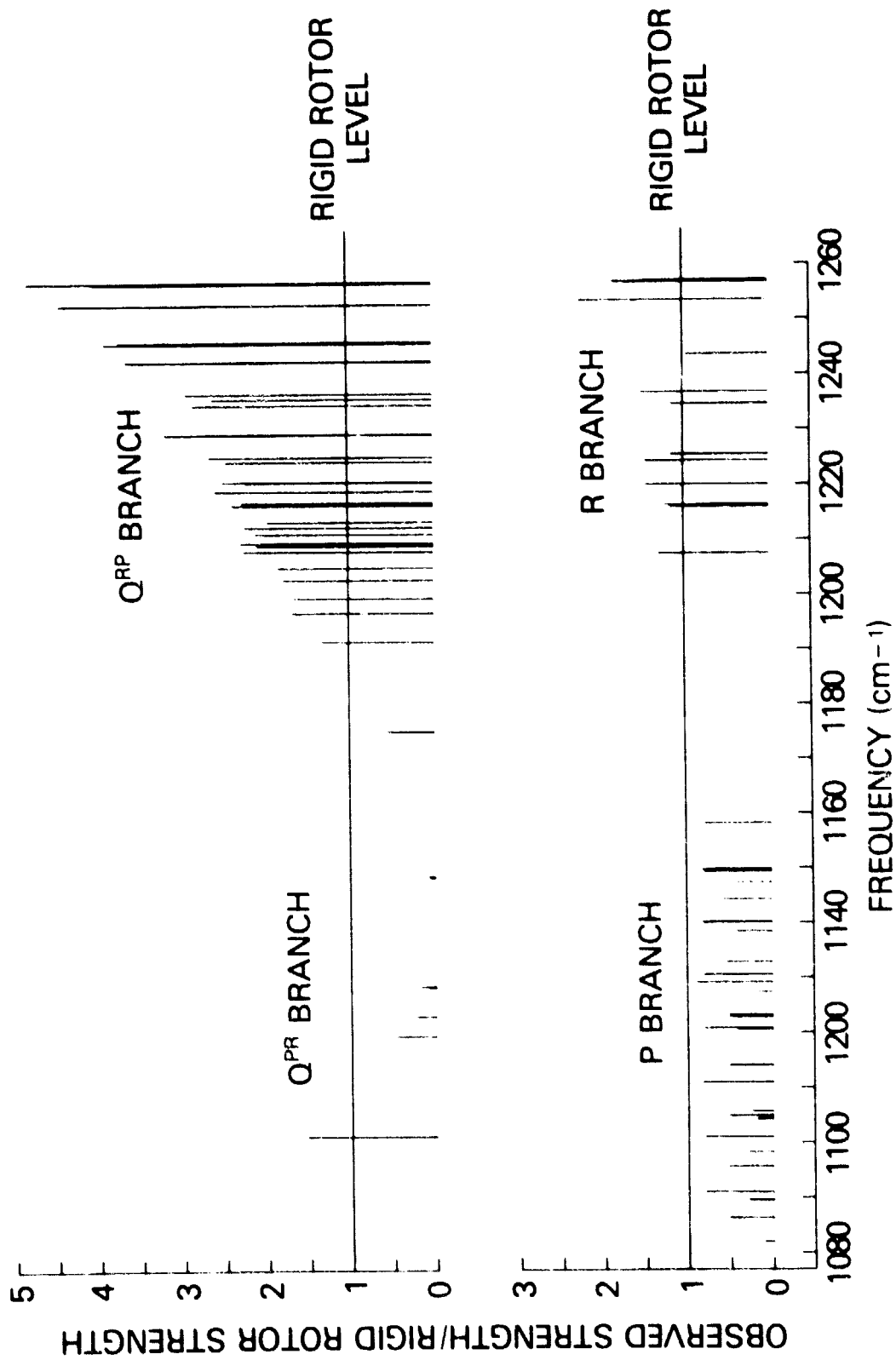


Figure VI-2. Ratio of Observed Line Strengths to Calculated Rigid Rotor Line Strengths (F Factor)

corresponds classically to rotation almost exclusively about the c axis of the molecule in both the upper and lower states of the transition. To a large degree, rotations about the c axis stretch the H-S bonds but do not change the bond angle. Centrifugal forces arising from rotations about the a and b axes, though, will alter the bond angle. Since the H<sub>2</sub>S force constants<sup>(60)</sup> involving bond angle changes are so much smaller than those involving bond stretching, rotations about the a and b axes distort the molecule more severely and therefore affect the dipole moment the most. Thus it is not surprising that the transitions with  $K_c$  at a maximum in both the upper and lower rotational states have line strengths close to rigid rotor values.

It is also expected that lines with a large change in  $K_a$  and  $K_c$  would have F factors very different from unity. Unfortunately lines with  $\Delta K_a$  and  $\Delta K_c$  greater than one are always very weak and hard to observe. Our only example of a line with both  $\Delta K_a$  and  $\Delta K_c$  greater than one, the  $5_{41}-5_{14}$  transition, had a F factor of 4.71, the largest one observed. For this transition, the rotational angular momentum about the a axis is much greater in the upper state than in the lower state. Therefore, the bond angle is smaller in the upper state. This difference in the molecular geometry between the upper and lower states results in a much larger change in the dipole moment for this transition relative to a rigid rotor transition.

The largest and smallest F factors were usually for the Q<sup>RP</sup> and Q<sup>PR</sup> lines respectively. This is partially because the observed Q branch lines had higher values of J and  $K_a$  than the observed R and P branch transitions. Since the distortion of the molecule is proportional to the square of the components of the total angular momentum, the difference in the distortion between two states with high J and  $K_a$  values is greater than the difference in the distortion between states with low values of J and  $K_a$ . In general, this leads to more strongly perturbed line strengths at high J and  $K_a$  values.

As mentioned in Ch. II, it is hoped that the line strength measurements presented here can serve as a severe test of the presently existing theories of centrifugal distortion in asymmetric rotor line strengths. The combination of the large strength perturbations present in

the  $\nu_2$  band of  $\text{H}_2\text{S}$  with the high accuracy of these measurements should make these line strengths very useful for that purpose.

CHAPTER VII  
NUCLEAR QUADRUPOLE HYPERFINE STRUCTURE IN THE INFRARED  
SPECTRUM OF HYDROGEN IODIDE

VII. A. Introduction

Nuclear quadrupole hyperfine structure in the 1-0 vibration-rotation band of hydrogen iodide near  $4.5 \mu\text{m}$  was observed using a tunable semiconductor diode laser.<sup>(64)</sup> Hyperfine structure arising from nuclear quadrupole interactions is commonly seen in microwave rotation spectra with splittings ranging from less than 1 MHz to several hundred MHz for molecules containing iodine. In vibration-rotation transitions, nuclear quadrupole splittings have been observed only in the past several years using the sub-Doppler resolution techniques of laser saturation spectroscopy in studies of methyl halide spectra.<sup>(65)</sup> In the case of hydrogen iodide however, its extremely large nuclear quadrupole moment and molecular weight combine to give relatively large hyperfine splittings with small Doppler widths. This allows resolution of some hyperfine structure in the low  $J$  transitions of hydrogen iodide with Doppler limited spectroscopy. Several studies of the 1-0 band of the HI molecule have been made with grating spectrometers with resolution too low to observe any hyperfine structure. The grating spectra were used in locating the transitions studied in the present work with the diode laser.<sup>(66, 67)</sup>

VII. B. Nuclear Quadrupole Interaction Theory

Nuclear quadrupole splittings arise through the interaction of the nuclear electric quadrupole moment with the electric field gradient of the molecular electron cloud. This interaction couples the nuclear spin  $I$  (if  $I > 1$ ) to the rotational angular momentum  $J$  to form the total angular momentum  $\underline{F} = \underline{I} + \underline{J}$  and splits each rotational level into  $2I + 1$  levels for  $J \geq I$  or  $2J + 1$  levels for  $I > J$ . These new levels each have different values of total angular

momentum denoted by the quantum number  $F$ , which varies from  $|J - 1|$  to  $|J + 1|$  in steps of one.

The interaction energy is given by<sup>(5)</sup>

$$H_Q = \frac{1}{6} \sum_{ij} V_{ij} Q_{ij} \quad (\text{VII-1})$$

where

$$Q_{ij} = \int_{\text{nucleus}} \rho(r) [3r_i r_j - r^2 \delta_{ij}] d\tau, \quad (\text{VII-2})$$

is the nuclear quadrupole moment tensor and

$$V_{ij} = \frac{\partial^2 V}{\partial r_i \partial r_j} = - \frac{\partial E_i}{\partial r_j} \quad (\text{VII-3})$$

is the molecular electric field gradient at the nucleus.  $\rho(r)$  represents the nuclear charge density and the  $r_i$  are space-fixed cartesian coordinates. The dependence of the interaction energy on the rotational state of the molecule was originally derived by Casimir<sup>(68)</sup> using first order perturbation theory, and can be found in several texts.<sup>(5,69)</sup> Casimir obtained

$$\langle 1JF | H_Q | 1JF \rangle = \frac{1}{2} eQq_J \left[ \frac{3/4 C(C+1) - 1(I+1)J(J+1)}{1(2I-1)J(2J-1)} \right] \quad (\text{VII-4})$$

where

$$C = F(F+1) - 1(I+1) - J(J+1). \quad (\text{VII-5})$$

$eQ$  is called the "quadrupole moment of the nucleus" and is defined in the limiting case of  $M_I = 1$  as

$$eQ = \langle 1, M_I = 1 | \rho(r) (3r_z^2 - r^2) | 1, M_I = 1 \rangle. \quad (\text{VII-6})$$

Similarly,  $q_J$  is defined as the value of the molecular electric field gradient in the  $z$  direction averaged over the state  $|J, M_J = J\rangle$ , or

$$q_J = \langle J, M_J = J | V_{zz} | J, M_J = J \rangle. \quad (\text{VII-7})$$

For a diatomic molecule

$$q_J = \frac{-qJ}{(2J+3)} \quad (\text{VII-8})$$

where  $q$  is the field gradient along the molecular bond axis. The rotational level splittings for a diatomic molecule can then be written as

$$\Delta E_Q = \langle I J F | H_Q | I J F \rangle = - (eQq) Y(I, J, F) \quad (\text{VII-9})$$

where

$$Y(I, J, F) = \frac{3/4 C(C+1) - I(I+1) J(J+1)}{2I(2I-1)(2J-1)(2J+3)} \quad (\text{VII-10})$$

The combined constant  $eQq$  is called the nuclear quadrupole coupling constant. The observed splittings in a vibration-rotation transition will be given by

$$\Delta\nu = (eQq)'' Y(I, J'', F'') - (eQq)' Y(I, J', F') \quad (\text{VII-11})$$

where a double prime indicates the upper state and a single prime the lower state of the transition. Though  $Y(I, J, F)$  in general varies for each hyperfine component and rotational level,  $eQq$  will only vary with vibrational state.

The relative intensities of the various hyperfine components within a given vibration-rotation transition are as follows,<sup>(70)</sup>

$$\begin{aligned} \frac{1}{F} Q(F) Q(F-1) \quad \Delta F = \mp 1 \\ \frac{2F+1}{F(F+1)} P(F) Q(F) \quad \Delta F = 0 \\ \frac{1}{F} P(F) P(F-1) \quad \Delta F = \pm 1 \end{aligned} \quad (\text{VII-12})$$

where

$$\begin{aligned} P(F) &= (F+J)(F+J+1) - I(I+1) \\ Q(F) &= I(I+1) - (F-J)(F-J+1). \end{aligned} \quad (\text{VII-13})$$

The top sign on  $\Delta F$  is to be used for  $\Delta J = +1$  (R Branch) transitions and the bottom sign for  $\Delta J = -1$  (P Branch) transitions.

The  $^{127}\text{I}$  nuclear spin of  $5/2$  and microwave determined ground vibrational state  $eQq$  of  $-1828.4 \text{ MHz}$ <sup>(71)</sup> for hydrogen iodide give line splittings in the pure rotation spectrum as large as  $800 \text{ MHz}$ . Splittings in the hydrogen iodide vibration-rotation spectrum will be very similar to the rotational splittings, modified slightly due to any dependence of  $eQq$  on the vibrational state of the molecule. The selection rules of  $\Delta I = 0, \Delta F = 0, \pm 1$  gives 3 lines for



R(0) and P(1), 9 lines for P(2), and 14 lines for P(3). Stick spectra for P(1), P(2), and P(3) calculated using the known ground state  $eQq$  and the first excited vibrational state  $eQq$  value measured in this work are given in Figure VII-1. Only 12 lines are shown for P(3) because two pairs of lines are degenerate to first order, although they are split by about 1.5 MHz, due to nuclear magnetic hyperfine effects,<sup>(71)</sup> which is too small to be shown in Figure VII-1 (c).

### VII. C. Experimental Considerations

The R(0) through P(3) lines, which fall in the region from 2190 to 2242  $\text{cm}^{-1}$ , were recorded using a PbSSe diode laser. The experimental apparatus was almost identical to that described in Ch. III except for the use of a one meter single pass cell instead of the White cell. Also the germanium etalon was not thermally stabilized during this work, which should not adversely affect the splitting measurements since the splittings are so small.

The gas cell pressures used ranged from 3 to 7 torr. The small strength of the H1 transitions<sup>(72)</sup> and the somewhat impure gas samples used required these relatively high pressures in the 1-meter cell. This resulted in linewidths generally 30% greater than the Doppler width of H1. It is unlikely that pressure shifts could introduce any systematic errors since all hyperfine levels in a given transition should have very similar pressure-shift coefficients.

The line centers, or minima within the hyperfine structure of a line, and etalon peaks were found digitally by least squares fitting the data to a cubic polynomial as described in Ch. IV. The splittings were determined using the calculated free spectral range for the etalon. Errors in the calculated free spectral range are negligible in this experiment since the splittings measured were so small. Random laser frequency fluctuations between fringe peaks was the main source of error, giving standard deviations of 3 to 10 MHz in the measured splittings.

### VII. D. Results

Figure VII-1 (a) gives the observed and calculated profiles of the P(1) transition. The triplet structure due to splitting in the  $J = 1$  rotational level is fully resolved. Since only the ground vibrational state is split in this transition, the infrared data can be directly compared to microwave measurements. The microwave value for  $eQq$  was used to generate the

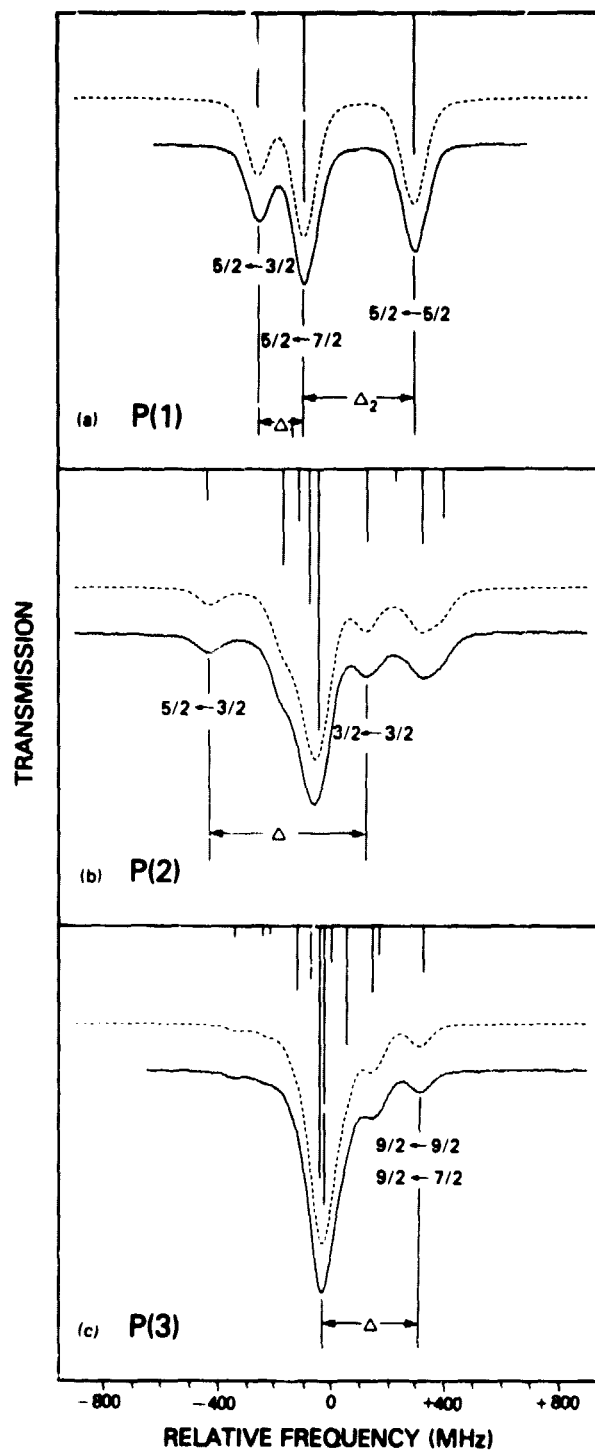


Figure VII-1: Observed and Calculated Profiles of P(1), P(2), and P(3) of HI. The solid line is the observed profile and the dashed line the calculated profile. The splittings measured are labeled  $\Delta$  and some individual transitions are identified by the quantum number F. Above each profile is a stick spectrum of the transition with a line length proportional to the relative strength.

calculated profile in Figure VII-1 (a). A Voigt line shape (see Ch. IV, equation IV-6) was used, arbitrarily scaling the line strength to closely approximate the observed absorption. The overall agreement, both for splittings and relative strengths, is very good. The splittings were corrected for slight blending by determining the amount of line shift due to blending in the synthetic Voigt profile. The calculated splittings also included small corrections for magnetic hyperfine contributions, averaging about 1.5 MHz, which is somewhat below the standard deviations of the measurements. Second order nuclear quadrupole hyperfine contributions were negligible.<sup>(69)</sup> Seven runs of the P(1) line were made and their scatter about the mean is the main contributor to the stated errors. Table VII-1 gives results for the measured splittings. Both splittings were measured relative to the strongest hyperfine component,  $F = 7/2 \rightarrow 5/2$ . They are compared in Table VII-1 to those calculated using the well known microwave determined ground state  $eQq$ . Agreement is within experimental error for both splittings.

The R(0), P(2), and P(3) transitions all involve rotational level splittings in the first excited vibrational state, allowing a determination of  $eQq$  in that state. As  $J$  increases, the intensity of  $\Delta F = \Delta J$  transitions become dominant over  $\Delta F = 0$  and  $\Delta F = -\Delta J$  transitions, and the spectra condense to the unperturbed line center. This causes an extreme amount of line blending, especially for P(2) and P(3), so that quadrupole coupling constants could not be directly obtained from the observed absorption features. In order to convert measured frequency intervals between minima in the spectrum of each line to an  $eQq$  value for the upper vibrational state, simulated Voigt profiles were made for each rotational line, keeping the ground state  $eQq$  constant while slightly varying the upper state  $eQq$  about the ground state value. From these profiles the change in observed splitting per unit change in upper state  $eQq$  was generated. Splittings analogous to those given by  $\Delta_1$  and  $\Delta_2$  in Figure VII-1 (a) for P(1) were measured in R(0) to obtain a value for the upper state  $eQq$ , while the splittings identified by  $\Delta$ 's in Figure VII-1 (b) and VII-1 (c) were used for the P(2) and P(3) measurements. These spectral features were a combination of lines exhibiting the least amount of blending and greatest sensitivity to upper state  $eQq$  value. The theoretical spectra

Table VII-1

Observed Splittings in P(1) of HI	
Splitting (MHz)*	Calculated - Observed (MHz)
$\Delta_1 = 159.9 \pm 3.2$	2.6
$\Delta_2 = 385.5 \pm 6.5$	-0.3

\*7 Trial Average

shown in Figure VII-1 (b) and VII-1 (c) were generated in the same manner as for P(1), using both the microwave derived ground state  $eQq$  value and the measured  $eQq$  in the first excited vibrational state. As with P(1), the overall agreement is very good for these transitions. Note, for example, the close agreement between the calculated and measured curves for the widely split but weak lines in P(3). The R(0) profile, which is not shown, appears identical in form to P(1) except reversed in frequency.

Table VII-2 gives the measured differences in  $eQq$  between the ground and first excited vibrational state using the method described above along with the first excited state  $eQq$  values themselves. The average value for the difference was found to be very small, as expected, not much larger than its standard deviation. Estimates for the standard deviations of the two weighted averages in Table VII-2 were derived from the standard deviations of the four individual measurements and not from the spread of these values about the weighted average. This was done because the uncertainties in the individual  $eQq$  values were larger than their spread about the mean. The last column in Table VII-2 illustrates the sensitivity of the measured splittings to the upper state  $eQq$  value, showing that P(2), for example, has the most sensitive splitting measured. In order to reveal any systematic errors in the splittings the measured difference in the ground state  $eQq$  from the much more accurate microwave value is also given in Table VII-2. This observed difference was determined from the P(1) transition. Its value, which lies less than one standard deviation away from 0%, indicates that there are no large systematic errors contributing to the upper state  $eQq$  determination. The measured difference between the ground and first excited vibrational state  $eQq$  of  $1.2 \pm 0.7\%$  is

Table VII-2

Observed Difference in Quadrupole Coupling  
Constant from Ground to 1st Excited Vibrational State

Transition	No. of Trials	Excited State eQq (MHz)	eQq Difference (%)	Change in Splitting for 1% Difference in eQq (MHz)
R(0) $\Delta_1$	5	$-1854 \pm 27$	$1.4 \pm 1.5$	1.8
$\Delta_2$		$-1853 \pm 48$	$1.4 \pm 2.6$	3.8
P(2)	4	$-1851 \pm 16$	$1.2 \pm 0.9$	5.8
P(3)	3	$-1830 \pm 44$	$0.1 \pm 2.4$	1.6
	Weighted Averages:	$-1850 \pm 13$	$1.2 \pm 0.7$	$(-22 \pm 13 \text{ MHz})$
P(1)	7		$-0.6 \pm 1.3^*$	

\*Measured Difference in Ground State eQq from Microwave Value

comparable in magnitude to the vibrational dependences found for eQq in methyl iodide<sup>(65,73)</sup> using laser saturated absorption experiments, where eQq was found to change for various vibrational modes from  $-0.3\%$  to  $+1.5\%$  per unit change in vibration quantum number.

In summary, nuclear quadrupole hyperfine structure has been observed in the vibration-rotation spectrum of hydrogen iodide. The measured splittings are in good agreement with microwave measurements of HI. The relative intensities observed for the hyperfine components were shown to be reproduced very well using the theoretical expressions for the relative strengths. Also, some evidence for a slight increase in the quadrupole coupling constant from the ground to first excited vibrational state was found.

## APPENDIX A

### PLANARITY RELATIONS AND DETERMINABLE CONSTANTS

A number of approximate relations can be derived for the rotational constants of a planar asymmetric rotor. It can be easily shown that the equilibrium quadratic constants obey the relation

$$C_e = \frac{A_e B_e}{A_e + B_e} \quad (\text{A-1})$$

since

$$I_c^e = I_a^e + I_b^e. \quad (\text{A-2})$$

These relations, which are only strictly valid for the equilibrium rotational constants (denoted by the superscript e), are approximately correct for the vibrationally averaged constants that are observed in practice. For example, equation A-1 is accurate to about 2% when the observed ground state rotational constants of H<sub>2</sub>S are used.

Similar planarity relations can be derived for the equilibrium quartic constants by utilizing the properties of the inertial derivatives of a planar molecule. These relations, originally derived by Dowling<sup>(12)</sup>, are

$$\begin{aligned} \tau_{aabb} &= \frac{1}{2} A^2 B^2 \left( -\frac{\tau_{aaaa}}{A^4} - \frac{\tau_{bbbb}}{B^4} + \frac{\tau_{cccc}}{C^4} \right) \\ \tau_{aacc} &= \frac{1}{2} A^2 C^2 \left( \frac{\tau_{aaaa}}{A^4} - \frac{\tau_{bbbb}}{B^4} + \frac{\tau_{cccc}}{C^4} \right) \\ \tau_{bbcc} &= \frac{1}{2} B^2 C^2 \left( -\frac{\tau_{aaaa}}{A^4} + \frac{\tau_{bbbb}}{B^4} + \frac{\tau_{cccc}}{C^4} \right) \\ \tau_{acac} &= \tau_{bcbc} = 0. \end{aligned} \quad (\text{A-3})$$

Therefore for a planar molecule, the nine quartic coefficients are reduced to four independent coefficients. In the above relations the superscript denoting equilibrium coefficients has been dropped.

These quartic planarity relations can also be applied to the quartic distortion constants in Watson's AS and NS reduced Hamiltonians to obtain a single relation among the fine reduced quartic constants. The relations for AS and NS Hamiltonians in the I<sup>r</sup> and III<sup>r</sup> representations are<sup>(62)</sup>

$$\begin{aligned}
 \text{AS-I}^r; \quad & 4C\Delta_J - (B - C)\Delta_{JK} - 2(2A + B + C)\delta_J + 2(B - C)\delta_K = 0 \\
 \text{AS-III}^r; \quad & 4C\Delta_J + (A + B + 2C)\Delta_{JK} + 2(A + B)\Delta_K + 2(A - B)(\delta_J + \delta_K) = 0 \\
 \text{NS-I}^r; \quad & 4CD_J - (B - C)D_{JK} + 2(2A + B + C)\delta_1 - 4(4A + B - 3C)\delta_2 = 0 \\
 \text{NS-III}^r; \quad & 4CD_J + (A + B + 2C)D_{JK} + 2(A + B)D_K - 2(A - B)\delta_1 = 0.
 \end{aligned} \tag{A-4}$$

Again, these relations are only strictly true for equilibrium quadratic and quartic constants, but should be approximately correct when the observed rotational constants are used instead.

A set of quadratic and quartic determinable constants in terms of the AS and NS reduced form constants have been derived by Watson<sup>(3)</sup>, and are as follows.

#### AS Form

$$\begin{aligned}
 X^D &= X^{AS} + 2\Delta_J + \Delta_{JK} - 2\delta_J - 2\delta_K \\
 Y^D &= Y^{AS} + 2\Delta_J + \Delta_{JK} + 2\delta_J + 2\delta_K \\
 Z^D &= Z^{AS} + 2\Delta_J \\
 T_{xx} &= -\Delta_J - 2\delta_J \\
 T_{yy} &= -\Delta_J + 2\delta_J \\
 T_{zz} &= -\Delta_J - \Delta_{JK} - \Delta_K \\
 T_1 &= -3\Delta_J - \Delta_{JK} \\
 T_2 &= -(X + Y + Z)\Delta_J - \frac{1}{2}(X + Y)\Delta_{JK} + (X - Y)(\delta_J + \delta_K)
 \end{aligned} \tag{A-5}$$

#### NS Form

$$\begin{aligned}
 X^D &= X^{NS} + 2D_J + D_{JK} + 2\delta_1 + 4\delta_2 \\
 Y^D &= Y^{NS} + 2D_J + D_{JK} - 2\delta_1 + 4\delta_2 \\
 Z^D &= Z^{NS} + 2D_J + 6\delta_2 \\
 T_{xx} &= -D_J + 2\delta_1 + 2\delta_2 \\
 T_{yy} &= -D_J - 2\delta_1 + 2\delta_2 \\
 T_{zz} &= -D_J - D_{JK} - D_K
 \end{aligned} \tag{A-6}$$

$$\begin{aligned}
 T_1 &= -3D_J - D_{JK} - 6\delta_2 & (A-6) \\
 T_2 &= -(X + Y + Z)D_J - \frac{1}{2}(X + Y)D_{JK} - (X - Y)\delta_1 - 6Z\delta_2. & \text{cont.}
 \end{aligned}$$

The X, Y, Z constants in the above relations for  $T_1$  and  $T_2$  correspond to the X, Y, Z constants in equation II-10. In this work  $X^D$ ,  $Y^D$ , and  $Z^D$  were used in place of X, Y, and Z. This should not introduce any errors in these relations larger than any already present.



APPENDIX B

CORRELATION TABLES FOR MOLECULAR CONSTANTS OF  
GROUND AND  $\nu_2 = 1$  EXCITED STATES OF H<sub>2</sub>S

Table B-1

Correlation Table, AS Form, I<sup>r</sup> Representation,  $\nu_2 = 1$  Upper State Fit, Ground State Fixed at Best Fit Value

$\nu_0$	B <sub>AS</sub>	C <sub>AS</sub>	A <sub>AS</sub>	$\Delta_J$	$\Delta_K$	$\delta_J$	$\delta_K$	H <sub>J</sub>	H <sub>JK</sub>	H <sub>KJ</sub>	H <sub>K</sub>	h <sub>J</sub>	h <sub>JK</sub>	h <sub>K</sub>
$\nu_0$	1.00													
B <sub>AS</sub>	-0.29	1.00												
C <sub>AS</sub>	-0.47	-0.07	1.00											
A <sub>AS</sub>	-0.36	-0.60	0.11	1.00										
$\Delta_J$	-0.26	0.80	0.30	-0.55	1.00									
$\Delta_{JK}$	0.01	-0.36	-0.24	0.40	-0.72	1.00								
$\Delta_K$	-0.15	-0.37	0.21	0.53	-0.08	-0.48	1.00							
$\delta_J$	-0.44	0.84	-0.40	-0.61	0.61	-0.38	-0.31	1.00						
$\delta_K$	-0.07	0.33	0.094	-0.17	0.42	0.12	-0.46	0.01	1.00					
H <sub>J</sub>	-0.18	0.68	0.29	-0.49	0.97	-0.77	0.01	0.53	0.42	1.00				
H <sub>JK</sub>	0.10	-0.20	-0.22	0.07	-0.58	0.88	-0.65	-0.24	0.10	-0.68	1.00			
H <sub>KJ</sub>	-0.19	-0.07	0.07	0.37	0.12	-0.34	0.64	-0.02	-0.10	0.20	-0.72	1.00		
H <sub>K</sub>	0.02	-0.40	0.14	0.27	-0.33	-0.02	0.40	-0.40	-0.39	0.15	-0.42	1.00		
h <sub>J</sub>	-0.03	0.74	-0.36	-0.56	0.55	-0.40	-0.24	0.97	-0.11	0.51	-0.30	0.03	-0.38	1.00
h <sub>JK</sub>	-0.00	0.32	0.12	-0.29	0.43	0.06	-0.51	0.02	0.91	0.41	0.19	-0.35	-0.20	-0.13
h <sub>K</sub>	-0.08	0.12	0.01	0.02	0.09	0.12	-0.16	0.17	0.34	0.12	-0.02	0.24	-0.50	0.06
														1.00

Table B-2

Correlation Table, AS Form III Representation,  $\nu_2 = 1$  Upper State Fit, Ground State Fixed at Best Fit Values

	$\nu_0$	AAS	BAS	CAS	$\Delta_J$	$\Delta_{JK}$	$\Delta_K$	$\delta_K$	$H_J$	$H_{KJ}$	$H_K$	$h_{JK}$	$h_K$
$\nu_0$	1.0												
AAS	-0.62	1.0											
BAS	-0.57	0.35	1.0										
CAS	-0.47	0.23	-0.18	1.0									
$\Delta_J$	-0.50	0.52	0.89	-0.19	1.0								
$\Delta_{JK}$	-0.04	0.27	-0.54	0.49	-0.60	1.0							
$\Delta_K$	0.15	-0.48	0.15	-0.14	0.21	-0.82	1.0						
$\delta_K$	-0.15	0.60	-0.31	0.35	-0.20	0.78	-0.68	1.0					
$H_J$	-0.46	0.57	0.76	-0.14	0.93	-0.49	0.15	-0.03	1.0				
$H_{JK}$	-0.10	0.30	-0.33	0.44	-0.38	0.84	-0.76	0.64	-0.46	1.0			
$H_K$	0.15	-0.36	0.18	-0.30	0.23	-0.76	0.83	-0.57	0.33	-0.97	1.0		
$h_{JK}$	-0.16	0.56	-0.13	0.24	0.01	0.48	-0.39	0.89	0.18	0.39	-0.32	1.0	
$h_K$	-0.17	0.39	-0.07	0.25	-0.05	0.58	-0.70	0.44	-0.20	0.88	-0.94	0.20	1.0

Table B-3

Correlation Table, NS Form, I<sup>r</sup> Representation,  $\nu_2 = 1$  Upper State Fit, Ground State Fixed at Best Fit Values

	$\nu_0$	B <sup>NS</sup>	C <sup>NS</sup>	A <sup>NS</sup>	D <sub>J</sub>	D <sub>JK</sub>	D <sub>K</sub>	$\delta_1$	$\delta_2$	H' <sub>J</sub>	H' <sub>JK</sub>	H' <sub>KJ</sub>	H' <sub>K</sub>	h <sub>1</sub>	h <sub>2</sub>	h <sub>3</sub>
$\nu_0$	1.00															
B <sup>NS</sup>	-0.31	1.00														
C <sup>NS</sup>	-0.47	-0.04	1.00													
A <sup>NS</sup>	-0.37	-0.57	0.08	1.00												
D <sub>J</sub>	-0.25	0.72	0.24	-0.51	1.00											
D <sub>JK</sub>	-0.04	-0.22	0.01	0.31	-0.76	1.00										
D <sub>K</sub>	-0.09	-0.27	-0.02	0.38	0.28	0.74	1.00									
$\delta_1$	0.05	-0.84	0.41	0.56	-0.67	0.42	0.05	1.00								
$\delta_2$	0.08	-0.18	-0.28	0.07	0.15	-0.65	0.71	-0.14	1.00							
H' <sub>J</sub>	-0.17	0.52	0.15	-0.35	0.93	-0.85	0.49	-0.60	0.30	1.00						
H' <sub>JK</sub>	0.07	-0.13	0.02	0.02	-0.60	0.82	-0.76	0.34	0.54	-0.82	1.00					
H' <sub>KJ</sub>	-0.16	0.02	-0.02	0.26	0.20	-0.26	0.42	-0.13	0.16	0.40	-0.74	1.00				
H' <sub>K</sub>	0.06	-0.28	0.01	0.15	-0.08	-0.22	0.38	0.25	0.35	-0.06	-0.15	-0.65	1.00			
h <sub>1</sub>	-0.03	0.74	-0.39	-0.53	0.69	-0.51	0.06	-0.97	0.26	0.67	-0.43	0.13	-0.16	1.00		
h <sub>2</sub>	-0.04	0.18	0.31	-0.16	-0.12	0.50	-0.74	0.15	-0.97	-0.32	0.62	-0.30	-0.29	-0.27	1.00	
h <sub>3</sub>	-0.08	0.09	0.09	0.02	-0.04	0.21	-0.22	0.01	-0.26	-0.04	-0.13	0.58	-0.77	-0.08	0.23	1.00

Table B-4

Correlation Table, NS Form, III<sup>r</sup> Representation,  $\nu_2 = 1$  Upper State Fit, Ground State Fixed at Best Fit Values

	$\nu_0$	A <sup>NS</sup>	B <sup>NS</sup>	C <sup>NS</sup>	D <sub>J</sub>	D <sub>JK</sub>	D <sub>K</sub>	$\delta_1$	$\delta_2$	H' <sub>J</sub>	H' <sub>JK</sub>	H' <sub>KJ</sub>	H' <sub>K</sub>	h <sub>1</sub>	h <sub>2</sub>	h <sub>3</sub>
$\nu_0$	1.00															
A <sup>NS</sup>	-0.36	1.00														
B <sup>NS</sup>	-0.31	-0.58	1.00													
C <sup>NS</sup>	-0.46	0.14	-0.01	1.00												
D <sub>J</sub>	-0.51	0.81	-0.07	0.01	1.00											
D <sub>JK</sub>	0.33	-0.62	0.02	0.06	-0.90	1.00										
D <sub>K</sub>	-0.21	0.28	-0.01	0.32	0.52	-0.79	1.00									
$\delta_1$	0.13	-0.91	0.76	0.01	-0.63	0.45	-0.17	1.00								
$\delta_2$	0.08	-0.43	0.34	0.04	-0.28	0.14	0.02	0.58	1.00							
H' <sub>J</sub>	-0.41	0.82	-0.21	0.02	0.96	-0.88	0.55	-0.72	-0.36	1.00						
H' <sub>JK</sub>	0.29	-0.64	0.18	0.10	-0.82	0.90	-0.78	0.57	0.25	-0.89	1.00					
H' <sub>KJ</sub>	-0.18	0.39	-0.21	0.30	0.47	-0.61	0.75	-0.39	-0.16	-0.16	0.58	1.00				
H' <sub>K</sub>	0.06	-0.27	0.27	-0.12	-0.16	0.12	-0.13	0.36	0.21	-0.29	0.49	-0.75	1.00			
h <sub>1</sub>	-0.14	0.86	-0.66	-0.02	0.65	-0.48	0.19	-0.97	-0.63	0.78	0.62	0.42	0.38	1.00		
h <sub>2</sub>	-0.09	0.51	-0.40	-0.03	0.37	-0.23	0.05	-0.67	-0.94	0.50	-0.38	0.26	-0.28	0.76	1.00	
h <sub>3</sub>	0.06	0.15	-0.29	0.01	-0.04	0.11	-0.10	-0.32	-0.44	0.06	-0.03	0.08	-0.19	0.39	0.60	1.00

Table B-5

Correlation Table, AS Form, I<sup>r</sup> Representation, Ground State Fit Using Microwave H<sub>2</sub>S Frequencies and Ground State Combination Differences

	BAS	CAS	AAS	Δ <sub>J</sub>	Δ <sub>JK</sub>	Δ <sub>K</sub>	δ <sub>J</sub>	δ <sub>K</sub>	H <sub>J</sub>	H <sub>JK</sub>	H <sub>KJ</sub>	H <sub>K</sub>	h <sub>J</sub>	h <sub>JK</sub>	h <sub>K</sub>	L <sub>JK</sub>	L <sub>KKJ</sub>	ℓ <sub>J</sub>	ℓ <sub>JK</sub>	ℓ <sub>KJ</sub>	ℓ <sub>K</sub>		
BAS	1.00																						
CAS	0.89	1.00																					
AAS	0.92	0.98	1.00																				
Δ <sub>J</sub>	0.89	0.86	0.90	1.00																			
Δ <sub>JK</sub>	0.53	0.31	0.46	0.61	1.00																		
Δ <sub>K</sub>	-0.58	-0.28	-0.42	-0.57	-0.96	1.00																	
δ <sub>J</sub>	0.61	0.38	0.50	0.75	0.93	-0.90	1.00																
δ <sub>K</sub>	-0.53	-0.40	-0.50	-0.73	-0.90	0.82	-0.95	1.00															
H <sub>J</sub>	0.72	0.70	0.72	0.89	0.41	-0.35	0.59	-0.57	1.00														
H <sub>JK</sub>	0.10	-0.10	0.02	0.07	0.74	-0.76	0.59	-0.59	-0.26	1.00													
H <sub>KJ</sub>	0.55	0.50	0.53	0.73	0.39	-0.33	0.51	-0.49	0.94	-0.31	1.00												
H <sub>K</sub>	-0.66	-0.49	-0.56	-0.78	-0.65	0.64	-0.73	0.67	-0.88	-0.12	-0.93	1.00											
h <sub>J</sub>	0.53	0.33	0.45	0.72	0.91	-0.85	0.98	-0.95	0.63	0.53	0.60	-0.78	1.00										
h <sub>JK</sub>	-0.11	0.00	-0.11	-0.21	-0.75	0.68	-0.67	0.73	0.08	-0.89	0.13	0.12	0.65	1.00									
h <sub>K</sub>	-0.59	-0.50	-0.54	-0.80	-0.60	0.55	-0.76	0.80	-0.85	-0.06	-0.82	0.25	-0.79	0.21	1.00								
L <sub>JK</sub>	-0.59	-0.35	-0.46	-0.69	-0.83	0.83	-0.85	0.81	-0.66	-0.39	-0.72	0.91	-0.88	0.46	0.79	1.00							
L <sub>KKJ</sub>	0.63	0.35	0.45	0.66	0.81	-0.84	0.82	-0.74	0.63	0.38	0.69	-0.90	0.83	-0.40	-0.73	-0.99	1.00						
ℓ <sub>J</sub>	-0.42	-0.23	-0.34	-0.65	-0.82	0.74	-0.90	0.87	-0.66	-0.37	-0.70	0.83	-0.96	0.55	0.78	0.88	-0.82	1.00					
ℓ <sub>JK</sub>	0.06	0.24	0.22	0.29	-0.07	0.21	0.05	-0.12	0.47	-0.42	0.50	-0.30	0.16	0.02	-0.22	0.14	0.06	-0.34	1.00				
ℓ <sub>KJ</sub>	0.42	0.21	0.30	0.51	0.81	-0.81	0.83	-0.87	0.36	0.65	0.33	-0.57	0.80	-0.67	-0.73	-0.79	0.76	-0.70	-0.24	1.00			
ℓ <sub>K</sub>	-0.09	0.01	-0.05	0.02	-0.12	0.15	0.03	-0.16	-0.08	0.08	-0.25	0.28	-0.02	-0.14	-0.19	0.22	-0.29	0.12	-0.07	0.17	1.00		

Table B-6

Correlation Table, As Form, III<sup>F</sup> Representation, Ground State Fit Using Microwave H<sub>2</sub>S Frequencies and Ground State Combination Differences

	AAS	BAS	CAS	$\Delta_J$	$\Delta_{JK}$	$\Delta_K$	$\delta_J$	$\delta_K$	H <sub>J</sub>	H <sub>JK</sub>	H <sub>KJ</sub>	H <sub>K</sub>	h <sub>J</sub>	h <sub>JK</sub>	h <sub>K</sub>	L <sub>J</sub>	L <sub>JK</sub>	$\rho_J$	$\rho_{KJ}$	$\rho_K$	
AAS	1.0																				
BAS	0.84	1.0																			
CAS	0.95	0.94	1.0																		
$\Delta_J$	0.82	0.64	0.66	1.0																	
$\Delta_{JK}$	-0.86	0.15	0.04	-0.13	1.0																
$\Delta_K$	-0.15	-0.31	-0.16	-0.34	-0.84	1.0															
$\delta_J$	-0.07	-0.30	-0.05	-0.22	-0.23	0.39	1.0														
$\delta_K$	0.59	0.16	0.31	0.70	-0.12	-0.20	-0.17	1.0													
H <sub>J</sub>	0.72	0.40	0.51	0.91	-0.31	-0.10	-0.06	0.79	1.0												
H <sub>JK</sub>	-0.28	0.07	-0.07	-0.39	0.89	-0.62	-0.16	-0.47	-0.56	1.0											
H <sub>KJ</sub>	0.20	-0.08	0.04	0.27	-0.80	0.62	0.14	0.36	0.42	-0.94	1.0										
H <sub>K</sub>	-0.28	-0.01	-0.10	-0.42	0.63	-0.39	-0.03	-0.46	-0.52	0.86	-0.96	1.0									
h <sub>J</sub>	-0.20	-0.20	-0.09	-0.32	0.01	0.22	0.75	-0.43	-0.30	0.08	0.06	-0.03	1.0								
h <sub>JK</sub>	0.34	0.04	0.16	0.35	0.04	-0.21	-0.05	0.65	0.46	-0.11	-0.14	0.14	-0.62	1.0							
h <sub>K</sub>	0.48	0.16	0.25	0.69	-0.53	0.17	-0.11	0.71	0.75	-0.78	0.78	-0.86	-0.12	0.05	1.0						
L <sub>J</sub>	-0.63	-0.33	-0.46	-0.77	0.21	0.07	-0.01	-0.69	-0.92	0.47	-0.44	0.56	0.17	-0.33	-0.67	1.0					
L <sub>JK</sub>	0.52	0.13	0.29	0.68	-0.46	0.13	0.09	0.73	0.88	-0.69	0.52	-0.55	-0.33	0.59	0.61	-0.86	1.0				
$\rho_J$	0.18	0.11	0.03	0.34	-0.55	0.25	-0.57	0.36	0.37	-0.59	0.48	-0.45	-0.97	0.28	0.48	-0.21	0.43	1.0			
$\rho_{KJ}$	-0.42	-0.01	-0.16	-0.55	0.59	-0.24	-0.33	-0.74	-0.69	0.74	-0.53	0.48	0.47	-0.70	-0.63	0.50	-0.79	-0.62	1.0		
$\rho_K$	0.12	-0.19	-0.06	0.12	-0.62	0.43	0.15	0.39	0.26	-0.60	0.37	-0.21	-0.41	0.65	0.22	-0.04	0.51	0.57	-0.85	1.0	

Table B-7

Correlation Table, NS Form, I<sup>r</sup> Representation, Ground State Fit Using Microwave H<sub>2</sub>S Frequencies and Ground State Combination Differences

	B <sup>NS</sup>	C <sup>NS</sup>	A <sup>NS</sup>	D <sub>J</sub>	D <sub>JK</sub>	D <sub>K</sub>	δ <sub>1</sub>	δ <sub>2</sub>	H' <sub>J</sub>	H' <sub>JK</sub>	H' <sub>KJ</sub>	H' <sub>K</sub>	h <sub>1</sub>	h <sub>2</sub>	h <sub>3</sub>	L' <sub>J</sub>	L' <sub>JK</sub>	L' <sub>JK</sub>	L' <sub>KKJ</sub>	L' <sub>K</sub>
B <sup>NS</sup>	1.0																			
C <sup>NS</sup>	0.53	1.0																		
A <sup>NS</sup>	0.80	0.82	1.0																	
D <sub>J</sub>	0.93	0.50	0.78	1.0																
D <sub>JK</sub>	0.57	0.01	0.29	0.46	1.0															
D <sub>K</sub>	-0.52	-0.05	-0.15	-0.35	-0.91	1.0														
δ <sub>1</sub>	-0.75	0.12	-0.35	-0.78	-0.60	0.46	1.0													
δ <sub>2</sub>	0.56	-0.18	0.23	0.65	0.42	-0.27	-0.87	1.0												
H' <sub>J</sub>	0.68	0.68	0.74	0.80	0.28	-0.19	-0.36	0.16	1.0											
H' <sub>JK</sub>	0.21	-0.04	0.04	0.01	0.64	-0.69	-0.16	0.11	-0.27	1.0										
H' <sub>KJ</sub>	0.45	0.07	0.29	0.55	0.49	-0.34	-0.54	0.34	0.67	-0.34	1.0									
H' <sub>K</sub>	-0.59	-0.07	-0.27	-0.55	-0.82	0.78	0.51	-0.37	-0.53	-0.17	-0.84	1.0								
h <sub>1</sub>	0.74	-0.10	0.35	0.78	0.65	-0.49	-0.98	0.80	0.47	0.11	0.66	-0.70	1.0							
h <sub>2</sub>	-0.46	0.27	-0.13	-0.53	-0.36	0.22	0.82	-0.99	-0.01	-0.11	-0.26	0.30	-0.73	1.0						
h <sub>3</sub>	-0.63	-0.09	-0.38	-0.69	-0.66	0.52	0.70	-0.39	-0.72	-0.01	-0.82	0.81	-0.83	0.27	1.0					
L' <sub>J</sub>	0.58	-0.33	0.14	0.58	0.69	-0.56	-0.94	0.77	0.21	0.28	0.52	-0.65	0.95	-0.73	-0.74	1.0				
L' <sub>JK</sub>	0.38	0.04	0.26	0.54	0.17	-0.01	-0.51	0.34	0.65	-0.62	0.90	-0.58	0.62	-0.27	-0.73	0.44	1.0			
L' <sub>JK</sub>	-0.56	-0.06	-0.30	-0.60	-0.63	0.52	0.63	-0.39	-0.64	0.15	-0.96	0.92	-0.74	0.31	0.85	-0.63	-0.83	1.0		
L' <sub>KKJ</sub>	0.61	0.04	0.26	0.56	0.74	-0.73	-0.65	0.37	0.47	0.19	0.72	-0.90	0.71	-0.30	-0.75	0.67	0.55	-0.88	1.0	
L' <sub>K</sub>	0.29	0.09	0.13	0.28	0.61	-0.58	-0.27	0.21	0.38	0.14	0.63	-0.75	0.35	-0.17	-0.49	0.33	0.31	-0.57	0.41	1.0



Table B-8

Correlation Table, NS Form, III<sup>r</sup> Representation, Ground State Fit Using Microwave H<sub>2</sub>S Frequencies  
and Ground State Combination Differences

	A <sup>NS</sup>	B <sup>NS</sup>	C <sup>NS</sup>	D <sub>J</sub>	D <sub>JK</sub>	D <sub>K</sub>	δ <sub>1</sub>	δ <sub>2</sub>	H' <sub>J</sub>	H' <sub>JK</sub>	H' <sub>KJ</sub>	H' <sub>K</sub>	h <sub>1</sub>	h <sub>2</sub>	h <sub>3</sub>
A <sup>NS</sup>	1.0														
B <sup>NS</sup>	0.93	1.0													
C <sup>NS</sup>	0.93	0.95	1.0												
D <sub>J</sub>	0.92	0.90	0.91	1.0											
D <sub>JK</sub>	-0.23	-0.11	-0.02	-0.10	1.0										
D <sub>K</sub>	-0.41	-0.47	-0.50	-0.59	-0.69	1.0									
δ <sub>1</sub>	0.09	0.41	0.31	0.13	0.26	-0.18	1.0								
δ <sub>2</sub>	0.02	0.25	0.21	0.02	0.41	-0.20	0.85	1.0							
H' <sub>J</sub>	0.83	0.81	0.88	0.88	-0.21	-0.30	0.20	0.11	1.0						
H' <sub>JK</sub>	0.15	0.26	0.39	0.18	0.56	-0.34	0.57	0.71	0.39	1.0					
H' <sub>KJ</sub>	-0.44	-0.49	-0.60	-0.43	-0.02	0.06	-0.45	-0.49	-0.77	-0.81	1.0				
H' <sub>K</sub>	0.32	0.35	0.45	0.26	-0.19	0.22	0.38	0.40	0.67	0.68	-0.96	1.0			
h <sub>1</sub>	-0.05	-0.31	-0.25	-0.06	-0.31	0.15	-0.92	-0.91	-0.14	-0.66	0.48	-0.41	1.0		
h <sub>2</sub>	-0.03	-0.23	-0.21	-0.02	-0.38	0.16	-0.81	-0.96	-0.12	-0.75	0.53	-0.45	0.94	1.0	
h <sub>3</sub>	-0.05	-0.19	-0.19	-0.03	-0.21	0.04	-0.61	-0.73	-0.16	-0.60	0.49	-0.45	0.77	0.86	1.0

## BIBLIOGRAPHY

1. M. T. Emerson and D. F. Eggers, Jr., *J. Chem. Phys.* 37, 251 (1962).
2. H. C. Allen and E. K. Plyler, *J. Chem. Phys.* 25, 1132 (1956).
3. J. K. G. Watson, in "Vibrational Spectra and Structure", Vol. 6, J. R. Durig, Ed., (Elsevier Scientific Pub. Co., New York, 1977).
4. E. B. Wilson and J. B. Howard, *J. Chem. Phys.* 4, 260 (1936).
5. H. W. Kroto, "Molecular Rotation Spectra", (Wiley, New York, 1975).
6. E. B. Wilson, J. C. Decius, and P. C. Cross, "Molecular Vibrations", (McGraw-Hill, New York, 1955).
7. B. T. Darling and D. M. Dennison, *Phys. Rev.* 57, 128 (1940).
8. J. K. G. Watson, *Mol. Physics* 15, 479 (1968).
9. G. Amat and H. H. Nielsen, *J. Chem. Phys.* 36, 1859 (1962).
10. D. Kivelson and E. B. Wilson, *J. Chem. Phys.* 21, 1229 (1953).
11. D. Kivelson and E. B. Wilson, *J. Chem. Phys.* 20, 1575 (1952).
12. J. M. Dowling, *J. Mol. Spectrosc.* 6, 550 (1961).
13. J. K. G. Watson, *J. Chem. Phys.* 46, 1935 (1967).
14. J. K. G. Watson, *J. Chem. Phys.* 48, 4517 (1968).
15. V. Typke, *J. Mol. Spectrosc.* 63, 170 (1976).
16. P. Helminger, R. L. Cook, and F. C. DeLucia, *J. Chem. Phys.* 56, 4581 (1972).
17. J. R. Gillis and T. H. Edwards, *J. Mol. Spectrosc.* 85, 55 (1981).
18. S. C. Wang, *Phys. Rev.* 34, 243 (1929).
19. H. C. Allen and P. C. Cross, "Molecular Vib-Rotors", (Wiley, New York, 1963).
20. G. W. King, R. M. Hainer, and P. C. Cross, *J. Chem. Phys.* 11, 27 (1943).
21. S. M. Kirschner, Ph.D. dissertation, Ohio State University, 1975.
22. R. H. Noble, *J. Chem. Phys.* 19, 799 (1951).
23. P. C. Cross, R. M. Hainer, and G. W. King, *J. Chem. Phys.* 12, 210 (1944).
24. J. M. Flaud and C. Camy-Peyret, *J. Mol. Spectrosc.* 55, 278 (1975).

25. Y. Ben-Aryeh, *J. Opt. Soc. Am.* 60, 1469 (1970).
26. J. Nagel and D. Rogovin, *J. Quart. Spectrosc. Radiat. Transfer* 22, 475 (1979).
27. R. L. Sams and W. B. Olson, *J. Mol. Spectrosc.* 84, 113 (1980).
28. R. S. Eng, P. L. Kelley, A. R. Calawa, T. C. Harman, and K. W. Nill, *Mol. Physics* 28, 653 (1974).
29. C. N. Harward and J. M. Hoell, *Appl. Opt.* 18, 3978 (1979).
30. G. N. Steinberg, *Rev. Sci. Instrum.* 50, 1622 (1979).
31. J. S. Wells, F. R. Petersen, and A. G. Maki, *Appl. Opt.* 18, 3567 (1979).
32. J. S. Wells, F. R. Petersen, A. G. Maki, and D. J. Suple, *Appl. Opt.* 20, 1676 (1981).
33. J. J. Hillman, D. E. Jennings, and J. L. Faris, *Appl. Opt.* 18, 1808 (1979).
34. R. S. Eng, J. F. Butler, and K. J. Linden, *Opt. Eng.* 19, 945 (1980).
35. E. D. Hinkley, K. W. Nill, and F. A. Blum, in "Laser Spectroscopy of Atoms and Molecules", H. Walther, Ed., (Springer-Verlag, Heidelberg, 1976).
36. (a) J. V. White, *J. Opt. Soc. Am.* 32, 285 (1942); (b) T. H. Edwards, *J. Opt. Soc. Am.* 51, 98 (1961).
37. M. El-Sherbiny, E. A. Ballik, J. Shewchun, B. K. Garside, and J. Reid, *Appl. Opt.* 18, 1198 (1979).
38. D. E. Jennings, *Appl. Opt.* 19, 2695 (1980).
39. W. B. Olson, A. G. Maki, and W. J. Lafferty, National Bureau of Standards, unpublished.
40. C. Freed, L. C. Bradley, and R. G. O'Donnell, *IEEE J. Quant. Elect.* 16, 1195 (1980).
41. J. B. Curtis, Ph.D. dissertation, Ohio State University, 1974.
42. H. W. Icenogle, B. C. Platt, and W. L. Wolfe, *Appl. Opt.* 15, 2348 (1976).
43. H. Flicker, J. P. Aldridge, H. Filip, N. G. Nereson, M. J. Reisfeld, and W. H. Weber, *Appl. Opt.* 17, 6 (1978).
44. W. S. Benedict, R. Herman, G. E. Moore, and S. Silverman, *Can. J. Phys.* 34, 834 (1956).
45. C. L. Korb, R. H. Hunt, E. K. Plyler, *J. Chem. Phys.* 48, 4252 (1968).

46. (a) W. G. Planet, G. L. Tetterer, and J. S. Knoll, *J. Quant. Spectrosc. Radiat. Transfer* 20, 547 (1978); (b) G. Restelli, F. Cappelloni, and G. Melandrone, *Chem. Phys. Lett.* 66, 454 (1979); (c) V. M. Devi, P. P. Das, A. Bano, and K. N. Rao, *J. Mol. Spectrosc.* 87, 578 (1981); (d) V. M. Devi, P. P. Das, A. Bano, K. N. Rao, J. M. Flaud, C. Camy-Peyret, and J. P. Chevillard, *J. Mol. Spectrosc.* 88, 251 (1981).
47. T. D. Wilkerson, G. Schwemmer, B. Gentry, and L. P. Giver, *J. Quant. Spectrosc. Radiat. Transfer* 22, 315 (1979).
48. C. Young, *J. Quant. Spectrosc. Radiat. Transfer* 5, 549 (1965).
49. J. J. Olivero and R. L. Longbothum, *J. Quant. Spectrosc. Radiat. Transfer* 17, 233 (1977).
50. B. Fridovich, V. M. Devi, and P. P. Das, *J. Mol. Spectrosc.* 81, 269 (1980).
51. P. P. Das, V. M. Devi, and K. N. Rao, *J. Mol. Spectrosc.* 84, 305 (1980).
52. R. E. Meredith, *J. Quant. Spectrosc. Radiat. Transfer* 12, 455 (1972).
53. "American Institute of Physics Handbook", 3rd ed., D. E. Gray, Ed. (McGraw-Hill, New York, 1972).
54. A. G. Maki and W. J. Lafferty, National Bureau of Standards, private communication.
55. J. J. Hillman, NASA-Goddard Space Flight Center, private communication.
56. P. J. Walsh, *Commun. Assoc. Comput. Mach.* 5, 511 (1962).
57. W. C. Hamilton, "Statistics in Physical Science", (Ronald Press Co., New York, 1964).
58. P. Helminger, F. C. DeLucia, and W. H. Kirchhoff, *J. Phys. Chem. Ref. Data* 2, 215 (1973).
59. J. H. Carpenter, *J. Mol. Spectrosc.* 46, 348 (1973).
60. R. L. Cook, F. C. DeLucia, and P. Helminger, *J. Mol. Struct.* 28, 237 (1975).
61. D. Kivelson, *J. Chem. Phys.* 22, 904 (1954).
62. J. K. G. Watson, *J. Mol. Spectrosc.* 65, 123 (1977).
63. G. Herzberg, "Molecular Spectra and Molecular Structure, II. Infrared and Raman Spectra of Polyatomic Molecules", (Van Nostrand Reinhold Co., New York, 1945).
64. L. L. Strow, *Optics Letters* 5, 166 (1980).
65. J. L. Hall and J. A. Magyar, in "High Resolution Laser Spectroscopy", K. Shimoda, Ed., (Springer-Verlag, New York, 1975).

66. L. A. Pugh and K. N. Rao, *J. Mol. Spectrosc.* 37, 373 (1971).
67. P. Niay, P. Bernage, C. Coquant, and A. Fayt, *J. Mol. Spectrosc.* 72, 168 (1978).
68. H. B. G. Casimir, "On the Interaction between Atomic Nuclei and Electrons", (Utzler's Tweede Genootschap, E. F. Bohn, Haarlem, 1936).
69. C. H. Townes and A. L. Schawlow, "Microwave Spectroscopy", (McGraw-Hill, New York, 1955).
70. W. Gordy, W. V. Smith, and R. F. Trambarulo, "Microwave Spectroscopy", (Wiley, New York, 1953).
71. F. C. DeLucia, P. Helminger, and W. Gordy, *Phys. Rev. A* 3, 1849 (1971).
72. G. Ameer and W. Benesch, *J. Chem. Phys.* 37, 2600 (1962).
73. E. Arimondo, P. Glorieux, and T. Oka, in "Laser Spectroscopy III", J. L. Hall and J. L. Carlsten, Eds. (Springer-Verlag, New York, 1977).

## CURRICULUM VITAE

**Name:** Lawrence Larrabee Strow.

**Permanent address:** 6064 Old Lawyers Hill Rd., Elkridge, Maryland 21227.

**Degree and date to be conferred:** Ph.D., 1981.

**Date of birth:** [REDACTED]

**Place of birth:** [REDACTED]

**Secondary education:** Howard County Senior High School,  
Ellicott City, Maryland, 1970.

Collegiate institutions attended	Dates	Degree	Date of Degree
University of Delaware	1970-71		
University of Maryland (at Baltimore County)	1971-74	B.A. Physics	1974
University of Maryland (at College Park)	1975-77	M.S. Physics	1977
University of Maryland (at College Park)	1977-81	Ph.D. Physics	1981

**Major:** Molecular Physics.

**Professional publications:** L. L. Strow, "Observation of Nuclear Quadrupole Hyperfine Structure in the Infrared Spectrum of Hydrogen Iodide Using a Tunable Diode Laser", *Optics Letters* 5, 166 (1980).

L. L. Strow, C. L. Korb, and B. M. Gentry, "A Cooled Optics Spectrometer for High Resolution Measurements in Support of Atmospheric Research", *Proceedings of the Optical Society of America Topical Meeting on Spectroscopy in Support of Atmospheric Measurements, Sarasota Florida, 1980.*

**Professional positions held:** Physicist - NASA Goddard Space Flight Center,  
Greenbelt, Maryland, 1974-present.